Quantum Simulation with Cold Atoms in Optical Lattices

by

Yang-Hao Chan

A dissertation submitted in partial fulfillment
of the requirements for the degree of
Doctor of Philosophy
(Physics)
in the University of Michigan
2013

Doctoral Committee:

Professor Luming Duan, Chair
Professor James W. Allen
Professor Georg A. Raithel
Professor Duncan Steel
Assistant Professor Kai Sun

To my family.

ACKNOWLEDGEMENTS

Foremost, I would like to thank my adviser, Professor Luming Duan, who mentors me for the past five years. His insight and perspective on physics problems greatly stimulates me. I always feel inspired from how he sees the interesting physics in our studies and how he is able to provide a broad picture in new areas. His sharpness in pointing out questions and creativity in solving problems always makes me feel refreshed in a discussion. He is a also a kind and patient teacher, who is willing to spend his time in explaining a new idea or method in great details. I am grateful to have such a brilliant and generous adviser.

I am in great debt to my master degree adviser, Professor YihYuh Chen. I am always impressed by the clarity and insight he offered in the lecture. His enthusiasm and broad knowledge in physics stimulates me to study a PhD program.

I would like to thank our group members, Bin Wang and Yong-jian Han (who introduced to me the tensor network algorithm), Wei Zhang and Jason Kestner (who taught me a lot in cold atom physics), Chao Shen and Shengtao Wang (we had a lot of discussion in coding and debugging), Zhexuan Gong, Dongling Deng, Zhen Zhang, and Yue Wu for sharing their knowledge in our journal clubs and of course, for their sincere friendship. I especially want to thank Guin-Dar Lin, who shares many thoughtful insight with me not only in physics but in other general areas. I would also like to thank our visitors, Zhaohui Wei, Zhangqi Yin, and Jiangming Zhang. They brought us different perspectives in physics research and inspired collaborations.

I am also thankful to Professor Congjun Wu in the University of San Diego, California (who taught me the background knowledge on high symmetry Heisenberg model), Professor Shi-liang Zhu in the South China Normal University, (who collaborates with us in the topological Bose-Mott insulators work) Hsiang-hsuan Hung (who introduced the ED method to me), and Hong-chen Jiang (who generously shared his knowledge on the DMRG method with me). It is a real pleasure to discuss with them. I benefit a lot from their expertise in these areas.

Finally, I am most grateful to have the constant support from my family. This thesis is dedicated to them, for without their encouragement and understanding I could not pursue my interests in physics.

TABLE OF CONTENTS

LIST OF FIGURES

Figure

ABSTRACT

A quantum simulator is a well-controlled quantum system which can be used to simulate another quantum system which we are interested. Quantum degenerate gases confined by optical standing waves(optical lattices) have been considered to simulate condensed matter systems. In this thesis we investigate the possibility of using these cold atom gases in optical lattices as quantum simulators. We focus on two issues in this problem. The first one is the realization of interesting quantum phases by engineering Hamiltonians with the cold atoms toolbox. Secondly, the systems we studied are often intractable to analytical methods, which makes it a crucial issue to solve them with numerical methods.

For the first issue we find several interesting phases can be studied with cold atoms in optical lattices. We show that a p-wave superfluid is stablized through a dissipation blockade mechanism. This mechanism also induces a new insulator formed by p-wave Feshbach molecules. We find that the anisotropic nature of interaction between polar molecules or dipolar atoms can be used to realize two charge density waves with different patterns and a supersolid phase which has not been found conclusively in the condensed matter system. Finally, we propose to realize a long sought spin liquid phase with hard-core bosons subject to a spin-dependent lattice and Raman induced hoppings.

For the second issue we choose to numerically study these systems with the so-

called tensor network algorithm. Tensor network algorithm is a variational method based on the matrix product states or tensor product states which are designed to approximate generic wave functions from their entanglement properties. In general the tensor network algorithm has advantages that it is applicable beyond one dimension, and can be used to study physical properties in the thermodynamic limit directly. We apply this method to map out the phase diagrams of the above systems. Furthermore, we show that it is capable of capturing the phase diagram of a frustrated magnetism model, the Heisenberg model on a checkerboard lattice.

The great controllability and isolation from the environment of a cold atom system offer a playground to study interesting physics in strongly correlated systems. Several proposed control schemes in this thesis have been demonstrated in experiments. By providing detailed evidence from numerical simulations, this work addresses practical routes to novel quantum phases.

CHAPTER I

Introduction

1.1 Motivation

The idea of quantum simulation was first proposed by Feynman back to 1982.[1] He suggested that instead of solving a quantum problem on a classical machine, which costs an exponentially high amount of computational resource, one could use a quantum simulator to fulfill this task. To simulate the behavior of electrons in materials, a quantum degenerate gas confined in the periodic potential created by optical methods(optical lattices) has been realized in the experiment. Since the first demonstration of a superfluid-Mott insulator transition[2] with cold atoms in an optical lattice many exciting progresses have been made over the last ten years in pursuing the holy grail of building a general quantum simulator of strongly correlated systems. These include a multicomponent bosonic Mott insulator in hexagonal lattices[3], fermionic Mott insulators[4, 5], an $SU(N)$ Mott insulator[6], dual Mott insulators of bosons and fermions[7], and a simulation of antiferromagnetic spin chains[8] among others. Besides Mott physics, a more recent discovery of topological materials such as quantum hall system and topological insulators has also motivated the development of synthetic gauge field[9, 10] for neutral cold atoms. Ultracold polar molecules and Feshbach molecules in an optical lattice[11], and orbital superfluidity[12, 13] also

bring novel physics into the field.

A cold atom toolbox of novel techniques mentioned above provides a platform with great controllability and versatility in the study of strongly correlated systems. With a wide range of tunable parameters, exotic quantum phases predicted in theoretical studies but not yet realized in condensed matter systems could possibly be reached. For example, supersolid phases[14] with hard-core bosons on a triangular lattice are discussed. Spin liquids can be studied in the high symmetry group Mott insulators. Topological Mott insulators[15] and even more bizarre Chern insulators[16] are made possible by considering the long-range dipole-dipole interaction of polar molecules confined in an optical lattice. The opportunity of systematically studying these quantum phases provided by cold atom systems is very exciting.

Meanwhile, to theoretically investigate physical properties in these models, a reliable tool is required. For strongly correlated systems which are often intractable to analytical analysis, numerical tools have proved to be useful for providing valuable knowledge. In one dimension the density matrix renormalization group(DMRG)[17, 18] can be used to calculate most physical properties of the system to high accuracy. In two dimensions quantum Monte Carlo results are often taken as exact ones. However, this method suffers from the so called sign problem which limits its applicability in fermion and frustrated systems. Thus, this program of research has two goals. First, we develop numerical codes using the tensor network algorithm for two dimensional systems. Secondly, these codes are then applied to study the engineered cold atom systems.

1.2 Background

In this section we briefly review basic concepts of optical lattices. The connection between atoms in an optical lattice to the Hubbard model and the Heisenberg model is discussed. In the last part we introduce the tensor network algorithm which serves as a main tool used in all the studies in this dissertation.

1.2.1 Optical lattices

The basic idea of optical lattice can be understood as a manipulated spatially varying field $\mathbf{E}$ with a lattice structure. From the classical light point of view, a neutral atom placed in an electric field $\mathbf{E}$ obtains an energy shift ΔV due to the induced dipole moment $\mathbf{d}$ as

$$\Delta V = -\frac{1}{2}\mathbf{d}\cdot\mathbf{E} = -\frac{1}{2}\alpha(\omega_l)|\mathbf{E}(\mathbf{r})|^2, \tag{1.1}$$

where α is the polarizability with a dependence on the frequency of $\mathbf{E}$ field ω_l. By applying coherent counter-propagating laser fields which form a standing wave pattern in space, atoms can then be confined in this lattice-like potential.

The polarizability depends on the internal structure of atoms. In a simple quantum picture, we take the atom as a two level system with the ground level $|g\rangle$ and an excited level $|e\rangle$ at frequency ω_0 close to the laser frequency ω_l. The ground state light shift is treated as a second order perturbation in $\mathbf{E}$ fields, which gives

$$\alpha(\omega_l) \simeq -\frac{|\langle e|d|g\rangle|^2}{\hbar\delta} \tag{1.2}$$

with the detuning $\delta = \omega_l - \omega_0$.[19, 20, 21] In this expression we have to consider the energy of the system as that of "atom plus light"[20] by using the photon energy $\hbar\omega_l$. The sign of polarizability $\alpha(\omega_l)$ thus potential depends on the detuning δ. We can see that atoms are attracted to the nodes(antinodes) of the laser intensity for

blue-detuned light with $\delta > 0$(red-detuned light with $\delta < 0$). Here we assumed the excited state population is low due to the far detuning of the field.

Considering a more general situation with spontaneous decay of the excited state we can solve the steady state of the density matrix equations[22]. In the density matrix formulation the force on an atom can be written as $\mathbf{f} = \mathrm{Tr}(\rho\nabla(\mathbf{d}\cdot\mathbf{E}))$, which is the expectation value of the negative gradient of the potential shift. For a standing wave field $\mathbf{E}(z) = E_0\hat{\mathbf{x}}\cos(kz)$ with rotating wave approximation in a frame rotating at the laser frequency we have

$$v_z\frac{\partial\rho_{11}}{\partial z} = -i\chi^*\cos(kz)\rho_{21} + i\chi\cos(kz)\rho_{12} + \gamma_2\rho_{22}, \tag{1.3}$$

$$v_z\frac{\partial\rho_{22}}{\partial z} = i\chi^*\cos(kz)\rho_{21} - i\chi\cos(kz)\rho_{12} - \gamma_2\rho_{22}, \tag{1.4}$$

$$v_z\frac{\partial\rho_{12}}{\partial z} = -i\chi^*\cos(kz)(\rho_{22}-\rho_{11}) - (\gamma - i\delta)\rho_{12}, \tag{1.5}$$

$$v_z\frac{\partial\rho_{21}}{\partial z} = i\chi\cos(kz)(\rho_{22}-\rho_{11}) - (\gamma + i\delta)\rho_{21}, \tag{1.6}$$

where v_z is atom velocity along z direction, γ_2 is the spontaneous decay rate, $\chi = \langle\mathbf{d}\cdot\mathbf{E}\rangle/2\hbar$ is half of the Rabi frequency and $\gamma = \frac{\gamma_2}{2} + \Gamma$ with Γ being the collision rate. To the first order in χ, with an initial population only in the ground state we have[22]

$$\rho_{12} = \frac{i\chi^*}{2}\left[\frac{e^{ikz}}{\gamma - i(\delta - kv_z)} + \frac{e^{-ikz}}{\gamma - i(\delta + kv_z)}\right]. \tag{1.7}$$

The force $\mathbf{f}$ is then

$$\begin{aligned}\mathbf{f} = {} & \hat{\mathbf{z}}\frac{\hbar k|\chi|^2\gamma}{2}\left[\frac{1}{\gamma^2 + (\delta + kv_z)^2} - \frac{1}{\gamma^2 + (\delta - kv_z)^2}\right] \\ & + \hat{\mathbf{z}}\frac{\hbar k|\chi|^2}{2}\left[\frac{\gamma\cos(2kz) - \sin(2kz)\Delta_-}{\gamma^2 + \Delta_-^2} - \frac{\gamma\cos(2kz) + \sin(2kz)\Delta_+}{\gamma^2 + \Delta_+^2}\right],\end{aligned} \tag{1.8}$$

where $\Delta_\pm = \delta \pm kv_z$. The first line describes a dissipative force which vanishes in the limit of large detuning δ while the second line recovers the gradient force from the

potential shift Eqn. 1.1 and Eqn. 1.2 in this limit. We can find a relation between the strength of the dissipative force $\mathbf{f}_{diss}$ and the dipole force $\mathbf{f}_{dipole}$.

$$\mathbf{f}_{diss} \simeq \frac{\gamma}{\delta}\mathbf{f}_{dipole}. \tag{1.9}$$

Since the dissipative force scales as δ^{-2} while the gradient force scales as δ^{-1}, for experiments with cold atoms the detuning is often chosen to be large to reduce the effect of the dissipative force.[20, 19, 21] A list of typical experimental parameters for the Rb atom is given in Table 1.1.

laser wave length	λ	767 nm
recoil energy	E_R	~ 3.88 kHz
lattice depth	V_0	~ 40 kHz
laser frequency detuning	δ	7000 GHz
trapping frequency	ω_{trap}	~ 4 kHz
spontaneous decay rate	γ_2	5.9 MHz
Hyperfine splitting in the excited state	Δ_{HF}	200 MHz
nearest neighbor hopping	J	~ 75 Hz
bandwidth	W	~ 200 Hz

Table 1.1: Typical experimental parameters for Rb atom

In the above we review the basic idea of an optical lattice in one spatial direction. By forming standing waves in two dimensions with the help of a strong transverse confinement, experimentalists are able to construct a two dimensional lattice. Lattices of different geometries such as the triangular lattice and the honeycomb lattice have also been constructed, which allows us to study interesting physics there.

One particular technique to form different optical lattices for different magnetic sublevels is realized by taking advantage of the strong dependence of their transition dipole matrices on the laser polarization. Considering the generalization of the two level atom results above to a multilevel atom, which is practical for experiments, we need to include the contribution of transition dipole matrices from different sublevels. For alkali atoms in the ground state with angular momentum F and magnetic

quantum number m_F, if the laser detuning is large compared to the excited state hyperfine splittings, the potential shift can be written as

$$\Delta V = \frac{\hbar|\chi|^2}{3}\left[\frac{2+Pg_F m_F}{\delta_{2,F}} + \frac{1-Pg_F m_F}{\delta_{1,F}}\right], \tag{1.10}$$

where g_F is the Landé factor and P is the laser polarization with $P = 0, \pm 1$ for linearly and circularly polarized light $\sigma^{\pm}$. $\delta_{1,F}$ and $\delta_{2,F}$ are the detuning referring to energy splitting between $^2S_{1/2}$, and $^2P_{1/2}$ and $^2P_{3/2}$ respectively[20]. For example at a "magic" wavelength 790 nm for ^{87}Rb, the spin independent part in the above equation vanishes. Thus, $m_F = 1$ and $m_F = -1$ states can have completely opposite potential with a circularly polarized light.

One application of spin dependent optical lattices is to realize an artificial magnetic field[23, 24]. Considering a two dimensional square lattice, atoms of two different sublevels are confined alternatively in one direction while in the other direction they distribute uniformly. The hopping between two sublevels is induced by the Raman transition, which can have an additional phase factor contributed from the wave vector of the Raman laser. This gives a controllable phase when atoms circle around a closed loop, which is exactly the effect when placing a charged particle in a gauge field.

1.2.2 Hubbard model and quantum magnetism

The behavior of fermionic atoms in an optical lattice can be described by the Hubbard model under suitable experiment conditions. The Hubbard model was first introduced to study interacting electrons in a lattice as a tight binding approximation. In this dissertation we will study several Hubbard-like models with variants in the form of interactions and atomic classes. Furthermore, quantum magnetism models which is another focus of this dissertation can also be derived from the Hubbard

model in the strong interaction limit. In this section we will briefly review the derivation of the Hubbard model and the super-exchange interaction of localized moments followed by the idea of frustrated magnetism.

We begin with a single particle in a 1D optical lattice, which is described by the Hamiltonian

$$H = \frac{p^2}{2m} + V_0 \sin^2(k_l x), \tag{1.11}$$

where m is the atom mass, V_0 is the amplitude of an optical lattice, $k_l = \pi/a$ is the wave-vector, and a is the lattice constant. The eigenstates of this Hamiltonian are the Bloch states ϕ[25], which can be written as

$$\phi_q^n(x) = e^{iqx} u_q^n(x), \tag{1.12}$$

with quasi-momentum $-\pi/a \leq q \leq \pi/a$ and band index n. The Bloch function $u_q^n(x)$ has the same periodicity as that of the lattice

$$u_q^n(x + a) = u_q^n(x). \tag{1.13}$$

For a periodic lattice with N sites q has discrete values with $\Delta k = 2\pi/(Na)$. The solution of Bloch functions $u_q^n(x)$ can be computed with a Fourier expansion and solving the linear eigenvalue equation.

A Bloch function at a fixed point x is periodic in q space. Thus we can expand it in the real space as

$$u_q^n(x) = \sqrt{\frac{a}{2\pi}} \sum_{r_i} \omega_n(r_i, x) e^{iqr_i}, \tag{1.14}$$

with r_i the minima of the lattice potential. The Wannier function $\omega_n(r_i, x)$ has the property of $\omega_n(r_i, x) = \omega_n(r_i - x)$ which can be seen by writing it as an inverse transformation of Bloch functions $u_q^n(x)$. Wannier functions at different sites are orthogonal to each other and they are not uniquely defined because of the freedom in

choosing phase factors in Bloch states ϕ. In one dimension one could choose a maximally localized Wannier function[26, 27] which is useful to describe local interactions between particles.

We review here the derivation of the Bose-Hubbard model which describes the bosonic atoms in the optical lattice. The derivation for fermionic atoms is similar and the results will be given in the following. We first write down the second quantization form of interacting particles in a lattice potential. In the cold atom experiment, particles interact with each other mainly through s-wave scattering which can be effectively described by a pseudopotential $U(x)$,[19]

$$U(x) = \frac{4\pi\hbar^2 a_s}{m}\delta(x) = g\delta(x), \tag{1.15}$$

where a_s is the scattering length. The Hamiltonian is written as

$$H = \int dx\psi^\dagger(x)(\frac{p^2}{2m} + V_0\,\sin^2(k_l x))\psi(x) + \frac{g}{2}\int dxdx'\psi^\dagger(x)\psi^\dagger(x')\delta(x-x')\psi(x')\psi(x). \tag{1.16}$$

We can expand the field operators ψ with Wannier functions and the bonsonic annihilation operators $b_{n,i}$ at n-th band and site r_i as

$$\psi(x) = \sum_{i,n}\omega_n(x - r_i)b_{n,i}. \tag{1.17}$$

Several approximations will be made in the derivation of the Hubbard model. First the integral

$$J = \int dx \sum_l \omega^*(x)(\frac{p^2}{2m} + V_0\,\sin^2(k_l x))\omega(x - la) \tag{1.18}$$

with l beyond nearest neighbor terms are two order of magnitude smaller than the nearest neighbor term. We can ignore them safely. Secondly, the off-site interaction is small compared with other terms so we will only keep the on-site interaction term

$$U = g\int dx|\omega(x)|^4. \tag{1.19}$$

Lastly, in a deep enough optical lattice when the interaction energy of particles is small compared to the band gap we can ignore the population of higher bands[28]. Thus it can be reduced to a single band model with $n = 0$ in the Wannier function and both creation and annihilation operators. For example in a typical experiment with $V_0 = 15\ E_R$ we have a band gap around $6\ E_R$ while interaction energy $U = 0.15\ E_R$ for Na atoms, where $E_R = \hbar^2 k^2/2m$ is the recoil energy of an atom with mass m in the optical lattice. This justifies the approximations we made above. The order of magnitude for the hopping strength J and the bandwidth W are given in Table 1.1. The model is then written as

$$H = H_t + H_U = -J \sum_{<i,j>} (b_i^\dagger b_j + h.c) + \frac{U}{2} \sum_i n_i(n_i - 1), \tag{1.20}$$

where $< i, j >$ stands for nearest neighbor pairs and n_i is the number operator on site i. The first term H_t is often referred as a hopping term which describes the tunneling of atoms to its nearest neighbor site and the second term H_U describes the interaction of atoms occupying the same site.

The fermionic Hubbard model can be derived in a similar fashion while the anti-commutation rule of fermions modifies the interaction term. For $S = \frac{1}{2}$ fermions the interaction term is written as

$$U \sum_i n_{i,\uparrow} n_{i,\downarrow}, \tag{1.21}$$

while for spinless fermions atoms are not allowed to occupy the same site and thus the nearest neighbor interaction term dominates as

$$U \sum_{<i,j>} n_i n_j, \tag{1.22}$$

where $< i, j >$ stands for all nearest neighbor pairs. Although the Hubbard model looks simple, its complete phase diagram is still not fully understood beyond one

dimension. It is suggested to have a Mott insulator phase at strong interaction with half filling, a d-wave superconductor phase, a pseudo-gap phase and a Fermi liquid in two dimensions.[29]

In the Mott insulator phase an effective hamiltonian can be written down, which itself has also been studied intensively. Considering a system with half-filled $S = \frac{1}{2}$ fermions, double occupancy on a site is inhibited in the strong interaction limit. The system at this point is known to be in a Mott insulator phase in which the charge degree of freedom is frozen and particles can only interact with each other through the so-called super-exchange interaction. Here, we briefly review the derivation of super-exchange interaction introduced in Ref. [30].

In the strong interaction limit with half filling, we can treat the hopping term as a perturbation with the small parameter J/U. The super-exchange interaction describes a virtual process where one particle hops to an occupied site and one of them hops back to the original site. The effective Hamiltonian is derived by taking a canonical transformation of H, as

$$H' = e^{-J\hat{O}} H e^{J\hat{O}} \tag{1.23}$$

with $\hat{O} = [\hat{P}_s H_t \hat{P}_d - \hat{P}_d H_t \hat{P}_s]/U$. $\hat{P}_s$ and $\hat{P}_d$ are projection operators onto singly and doubly occupied subspaces respectively. Calculating H' up to second order in J and projecting onto the singly occupied subspace we get

$$\hat{P}_s H' \hat{P}_s = \sum_{<i,j>} J_{ex} \left(\mathbf{S}_i \cdot \mathbf{S}_j - \frac{1}{4} \right), \tag{1.24}$$

where $J_{ex} = 4J^2/U$, $\mathbf{S}_i = \frac{1}{2} b^\dagger_{i,\alpha} \sigma_{\alpha\beta} b_{i,\beta}$ is the spin operators with the Pauli matrices $\sigma_{\alpha\beta}$ and $b_{i,\alpha}$ is the fermionic annihilation operator with spin index α. Eqn. 1.24 is the so-called Heisenberg model which describes the basic interaction of localized

moments. If J_{ex} is positive spins on neighboring sites tend to align themselves in opposite direction while a negative J_{ex} will align them in the same direction.

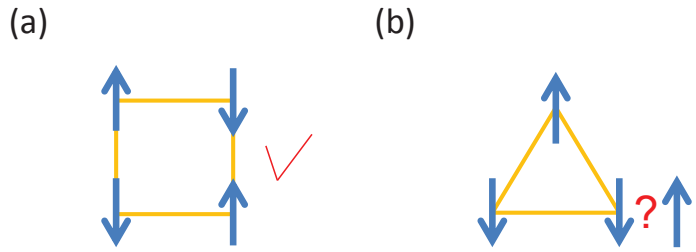

Figure 1.1: (a) Spin orientation minimizes energy on every bond on a square lattice. (b) Energy can not be minimized on all bonds on a triangular lattice.

The Heisenberg model has been widely studied on different lattices. One particular interesting class is that on lattices with geometric frustration. To discuss the idea of geometric frustration, let's begin with a Ising Hamiltonian

$$H = J \sum_{<i,j>} \sigma_i^z \sigma_j^z, \tag{1.25}$$

where σ_i^z is the Pauli z matrix and J is taken to be positive. On a square lattice the ground state can be established by aligning neighboring spins in the opposite direction as shown in figure 1.1(a). We notice that with this arrangement the energy of each bond is minimized as well. However, this is not the case if we consider a triangular lattice. For example in figure 1.1(b) we can find that it is not possible to minimize the energy of all three bonds simultaneously in a triangular unit and what we show here are actually two possible ground states out of six. The phenomenon that one can not minimize all bond energy at the same time is called frustration. It comes from the competing interaction between spins on different sites and in this particular case geometry of the underlying lattice plays a main role.

As the example above shows, frustration inevitably brings degeneracy to the ground states. At a classical level the large ground state degeneracy prevents the triangular lattice system from picking any ordering even at very low temperature. It is believed that the ground state of a highly frustrated model would be a liquid like phase without any ordering, which is thus called a spin liquid[31, 32]. In the quantum case it is generally believed that the interplay between quantum fluctuation and frustration may also lead to a liquid like state. Several candidate materials are found in experiments.[33] In chapter V we propose an implementation to study spin liquids in cold atom systems.

1.2.3 Tensor network algorithm

In this section we introduce the main numerical tool we used in this dissertation: the tensor network algorithm. We will first briefly discuss the main idea of this algorithm and then focus on the implementation for the 1D case: infinite Time-evolved Block Decimation(iTEBD). Finally we discuss its extension to the 2D case: infinite Projected-Entangled-Pair States.

Matrix product states

For a quantum mechanical problem, the computational complexity often scales exponentially with the particle number of the system. This seriously limits the ability to solve physical problems with numerical methods. For example with a high end computer people can solve the ground state of a Heisenberg model on a square lattice with about 42 spins, which has a Hilbert space dimension of about 4 trillion(2^{42}). Compared with the size of the real material samples, the finite-size effect on this scale could still pose problems for interesting physical quantities. Fortunately, the search for ground states in certain physical systems could be done

more efficiently by exploiting their particular entanglement properties. In these cases a special class of ansatz states called matrix product states(MPS) can be written down to efficiently approximate the ground state. The success of Density Matrix Renormalization Group(DMRG)[34, 17] algorithm in one dimensional problems is closely related to efficiently finding the ground state within the MPS manifold.

A heuristic way to understand MPS is through the perspective of a mean field theory. In a mean field theory, ansatz states are often written down as product states of single particle or local basis. One can then optimize coefficients of these ansatz states through variational methods. For example a general wave function of spinless fermions in a lattice is

$$|\psi\rangle = \sum_{i_1 i_2 ... i_n} c_{i_1 i_2 ... i_n} |n_{i_1} n_{i_2} ... n_{i_n}\rangle , \tag{1.26}$$

where $|n\rangle = |0\rangle$ or $|1\rangle$ represents local occupation number of fermion and there are up to 2^n coefficients. Under a mean field treatment the above state could be approximated by

$$|\psi\rangle \simeq \prod_i \tilde{c}_i |\phi_i\rangle , \tag{1.27}$$

where ϕ_i can be a superposition of $|0\rangle$ and $|1\rangle$ and the number of coefficients is reduced to n. An approximate ground state can then be obtained by variational methods. We can immediately see the main drawback of this product ansatz state. It can not describe the entanglement between two different sites, which in many cases is essential to a correct ground state.

MPS in this sense is considered to be an extension of the above product states. We can replace the complex number coefficients $\tilde{c}_i$ with $D \times D$ matrices A^i, where D is called the virtual dimension. At every site we have a collection of $D \times D$ matrices

or a $d \times D^2$ tensor where d is the dimension of local Hilbert space. The coefficients of the state $|\psi\rangle$ is then obtained by multiplying these matrices. The wave function then reads

$$|\psi\rangle \simeq \sum_{i_1,i_2,...,i_n=1}^{d} A^{i_1} A^{i_2} ... A^{i_n} \, |n_{i_1} n_{i_2} ... n_{i_n}\rangle \, . \tag{1.28}$$

The number of free parameters in this expression is now nD^2, which scales only polynomially to the size of the system. This significantly reduces the computational cost of the problems. Furthermore, we will see below in the discussion of obtaining a MPS representation of an arbitrary wave function that the entanglement amount captured by this ansatz state is related to the virtual dimension D of the matrices.

The discussion of representing an arbitrary 1D wave function with MPS is detailed in several papers[35, 36, 37, 38]. We briefly review here for completeness of our introduction. The idea is to decompose the wave function through a series of singular value decomposition(SVD) or the Schmidt decomposition. Consider our n sites wave function $|\psi\rangle$. We can first group indices $(2, 3, ..., n)$ as a super index then perform a Schmidt decomposition on this bipartite system, which is conveniently done by a SVD operation on the coefficient matrix. The result gives the coefficient $c_{i_1 i_2 ... i_n}$ in 1.26 as

$$c_{i_1 i_2 ... i_n} = \sum_{\alpha} A^{i_1}_{\alpha} \Phi_{\alpha, i_2 ... i_n}, \tag{1.29}$$

where $A^{i_1}_{\alpha}$ is a collection of row vectors with dimension D. We can follow the same prescription above to further decompose $\Phi_{\alpha, i_2 ... i_n}$ into

$$\Phi_{\alpha, i_2 ... i_n} = \sum_{\beta} A^{i_2}_{\alpha\beta} \Phi_{\beta, i_3 ... i_n}, \tag{1.30}$$

where $A^{i_2}_{\alpha\beta}$ is a collection of $D \times D$ matrices. Repeat this procedure to the end of

the lattice. Finally, we will have

$$c_{i_1 i_2 \ldots i_n} = A^{i_1} A^{i_2} \ldots A^{i_n}, \tag{1.31}$$

as we claimed in Eqn. 1.28. We notice that at the $l(1 < l < n)$ step we have

$$c_{i_1 i_2 \ldots i_n} = \sum_{\alpha} (A^{i_1} A^{i_2} \ldots A^{i_l})_{\alpha} S_{\alpha,\alpha} \Phi_{\alpha, i_{l+1} \ldots i_n}, \tag{1.32}$$

with a singular value $S_{\alpha,\alpha}$. We could rewrite the wave function as

$$|\psi\rangle = \sum_{\alpha} S_{\alpha,\alpha} \, |a_\alpha\rangle_{1,2,\ldots,l} \, |b_\alpha\rangle_{l+1,l+2,\ldots,n} \,, \tag{1.33}$$

with

$$|a_\alpha\rangle_{1,2,\ldots,l} = \sum_{i_1, i_2, \ldots, i_l} (A^{i_1} A^{i_2} \ldots A^{i_l})_{\alpha} \, |i_1 i_2 \ldots i_l\rangle \tag{1.34}$$

and

$$|b_\alpha\rangle_{l+1,l+2,\ldots,n} = \sum_{i_{l+1}, i_{l+2}, \ldots, i_n} \Phi_{\alpha, i_{l+1} \ldots i_n} \, |i_{l+1} i_{l+2} \ldots i_n\rangle \,, \tag{1.35}$$

which is the Schmidt decomposition of the state $|\psi\rangle$. The von Neumann entanglement entropy of this bi-partition can be read off from the Schmidt decomposition immediately,

$$S = -\sum_{\alpha=1}^{D} S_{\alpha,\alpha}^2 \log_2 S_{\alpha,\alpha}^2. \tag{1.36}$$

Thus, the virtual dimension D quantifies the entanglement that MPS ansatz states could capture as we mentioned earlier. In the implementation of our algorithm since we could only choose a finite D value, it is always important to test the convergence of our results in D.

The success of variational methods based on MPS, like DMRG and iTEBD lies in an important observation of the entanglement entropy of the ground states. In

1D gapped system it is known that the entanglement entropy of the system with a correlation length ξ saturates as $S \sim \log \xi$, whereas it scales as $S \sim \log L$ for a subsystem with length L[39] in a 1D critical system. In either case the entanglement does not grow very rapidly with system size. Thus, an efficient variational method with an MPS ansatz which is able to capture the low entanglement property of these states can be built successfully.

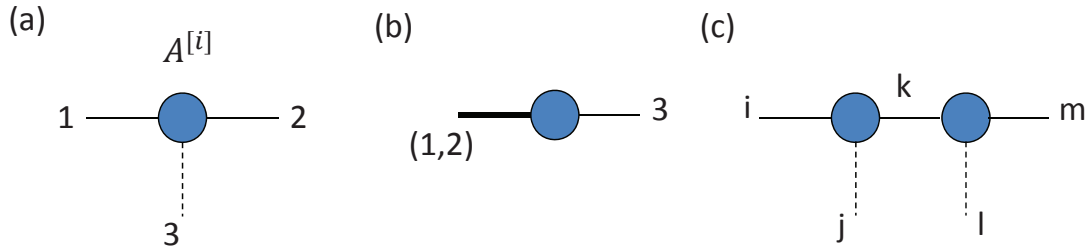

Figure 1.2: (a) A^i tensor in equation 1.34 with two virtual indices in solid line and one physical index in dashed line. (b) Relabel indices 2 and 3 by assigning the physical index with 2 and the right virtual index with 3 then reshape the new tensor by grouping the left virtual index 1 and the physical index 2 into a thicker leg. This is for later convenience in the contraction step. (c) Contraction an index k of two tensors as in equation 1.37 is drawed by connecting their correspondent legs.

Graphical notation of fundamental manipulations

The description in terms of matrices could be very tedious when we discuss their manipulation in the algorithm. It is therefore useful to introduce a graphical notation in which the operations on the matrices are replaced by a few drawings. We will represent a rank n tensor as a dot with n legs. In this notation a complex number is a simple dot without any leg, a vector is a dot with one leg, and a matrix is a dot with two legs, etc. For example the A^i matrices above have three legs, two of them in solid line are indices for virtual degree of freedom while the other index in dashed

line is for local physical degree of freedom i as shown in figure 1.2(a). We can label different legs by assigning numbers to them, which is convenient for bookkeeping.

Four basic manipulations of tensors are required in the algorithm: index relabelling, tensor reshaping, index contraction(matrices multiplication), and singular value decomposition. Index relabelling is done in the graphic notation by reassigning proper numbers to indices. This changes the storage sequences of these indices in the computer. For the bosonic system changes in the ordering of indices do not have physical consequences, but are only for programming convenience in the later contraction step. However, extra care must be taken in the fermionic system where permutation of two indices might introduce an additional negative sign. Since in this thesis we mainly discuss systems with bosonic degree of freedom we leave the details of fermionic PEPS in Ref. [40, 41]. In the algorithm we often need to combine several indices into a super-index or split a super-index back to several indices. This requires reshaping a tensor into another one with a different number of legs. We will represent the combined super-index by a thicker line with a bracket including labels of joining indices as in figure 1.2(b). Index contraction or matrix multiplication is denoted by connecting corresponding indices of two tensors. For example in figure 1.2(c) we show the contraction of an index k of two tensors A and B

$$C_{ij,lm} = \sum_k A_{ijk} B_{klm}. \tag{1.37}$$

iTEBD

In this subsection we briefly introduce our implementation of the iTEBD algorithm. The iTEBD algorithm has the advantage of finding the ground state of a 1D system in the thermodynamic limit directly without resorting to finite size extrapolation[38]. The algorithm assumes a partial translational invariance of MPS

states, under which the ground state can be found by efficiently updating local tensors in a parallel fashion.

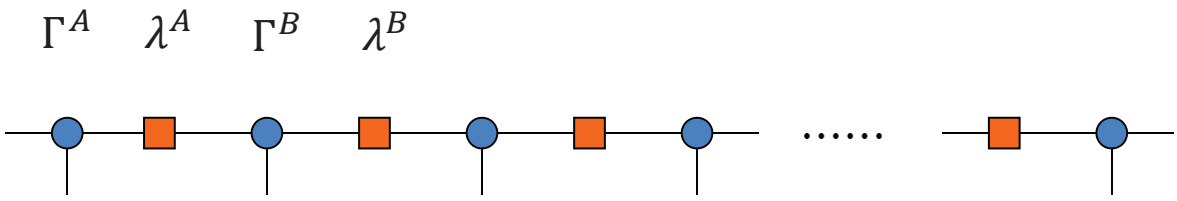

Figure 1.3: $\{\Gamma, \lambda\}$ representation of states used in the iTEBD algorithm.

In the iTEBD algorithm states are represented by two different rank 3 tensors Γ^A, Γ^B, and two matrices λ^A, λ^B through

$$|\psi\rangle \simeq \sum_{\ldots,i_1,i_2,\ldots}^{d} \ldots\Gamma^{[A]i_1}\lambda^A\Gamma^{[B]i_2}\lambda^B\ldots\,|\ldots n_{i_1} n_{i_2}\ldots\rangle\,. \tag{1.38}$$

The above structure is repeated infinite times, where the translational invariance by shifting two sites is manifest. This can be recast to a more familiar form as equation 1.28 if we absorbed the $\lambda^{A,B}$ matrices into $\Gamma^{A,B}$. Diagrammatically the state is shown as in figure 1.3, where we use squares to distinguish λ matrices.

To obtain the ground state efficiently, we adapt imaginary time evolution methods. The Hamiltonian we are interested in can be written as a sum of local two-sites Hamiltonian as

$$H = \sum_r h^{[r,r+1]}. \tag{1.39}$$

We denote the sum of terms starting with even sites as a new operator F and those with odd sites as G. The time evolution operators U can then be expanded with Suzuki-Trotter formula as functions of F and G.

$$U(T) = e^{-iHT} = (e^{-iHdt})^{T/dt} \simeq (e^{(-idt/2)F} e^{-idtG} e^{(-idt/2)F})^{T/dt}, \tag{1.40}$$

where T is the total evolution time and dt is the small time step. In the third equality we used a second order Suzuki-Trotter expansion. We can always choose a higher order expansion which will reduce the error from finite size of dt. However, there are more terms involved in a higher order expansion, which in turn increases the computation time.

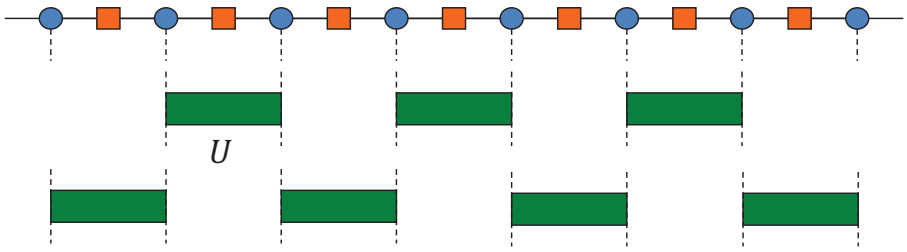

Figure 1.4: A time evolution step consists of updating even and odd links.

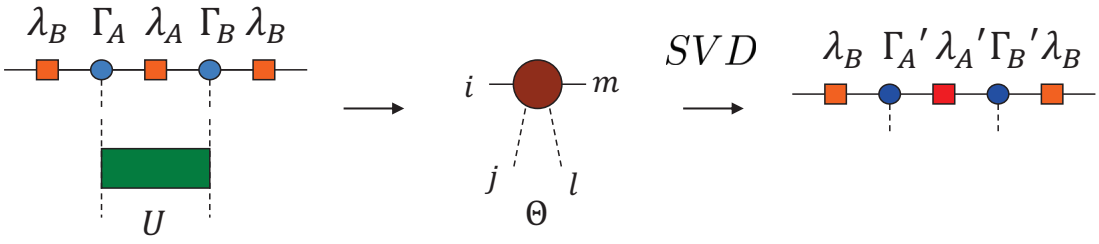

Figure 1.5: Update MPS on the λ^A link.

A small step of time evolution can be done by first applying the operator $U(dt) = e^{-iHdt}$ on the odd links of MPS followed by the same operation on the even links as we show in figure 1.4, in which the time evolution operator $U(dt)$ is represented by a rectangle with four legs. The operation of U on the link where λ^A sits is described in figure 1.5. Similar operations can be done on the other link. We first contract corresponding legs as in figure 1.5 of λ^B, Γ^A, λ^A, Γ^B, λ^B, and U into a

four-legs big tensor Θ. At this stage the operation is finished and we notice that no approximation is made so far. However, we need to restore the original MPS form for further operations. This requires to split the Θ tensor into new Γ tensors. One can show that the optimized choices of Γ tensors is to do a singular value decomposition on the Θ tensor as shown in the final step in figure 1.5. The physical index and virtual index of Θ on the left side and right side are joined separately into two super-indices. We then apply a singular value decomposition on this reshaped Θ tensor as

$$\Theta_{(ij),(ml)} = U_{ij,k} S_{kk} V_{k,ml} \tag{1.41}$$

The singular value S_{kk} is taken as the λ'_A matrix and $U_{ij,k}$ and $V_{k,ml}$ matrices are reshaped to Γ'_A and Γ'_B respectively. Since Θ is a $dD \times dD$ matrix the updated leg of Γ tensor would have a dimension of dD if we do not make any cut, which leads to an exponential increase of computational resource with increasing time steps. Thus at every step only the largest D singular values and corresponding parts of U and V matrices are kept. This is exactly the same strategy used in DMRG by keeping states with the largest eigenvalues of the reduced density matrix.

The above procedure is general for both real time and imaginary time evolution. However, we notice that in a real time process, the entanglement might grow rapidly in certain quantum quench simulation. In these cases care must be taken in the accuracy of simulation results. A recent paper demonstrates the spreading of correlations with cold atoms in an optical lattice along with numerical results calculated by time-dependent DMRG method for comparison[42]. It is observed that the simulation result is only reliable up to a few $1/J$(J is the hopping strength). On the other hand, ground states can be found more accurately by imaginary time evolution as long as they belong to the class of low entanglement states.

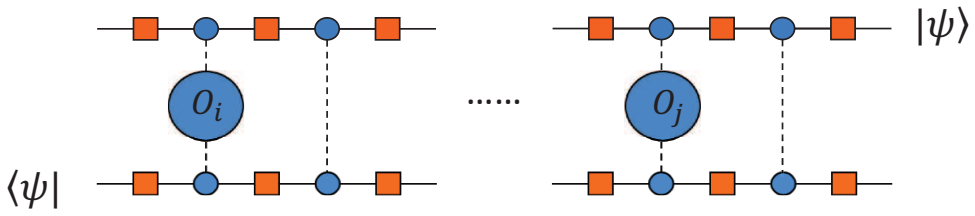

Figure 1.6: Calculate expectation value of a composite operator O_iO_j

Once the ground state is found, expectation values of physical observables can be calculated efficiently with MPS structure. To obtain a general two-site expectation value of composite observable O_iO_j at sites i and j, we calculate

$$\langle\psi|O_iO_j|\psi\rangle, \tag{1.42}$$

which can be done by sandwiching O_iO_j with MPS and its conjugate, then contracting the whole tensor network. In figure 1.6 we demonstrate this tensor network in which the up-side down MPS stands for the bra vector of $\langle\psi|$ and the operators O_i and O_j are inserted at i-th and j-th site while at other sites a direct contraction is assumed. This is useful when we want to calculate the spin-spin correlation function $\langle S_iS_j\rangle$ in a Heisenberg model or single particle density matrix $\langle b_i^\dagger b_j\rangle$ in a Bose-Hubbard model. The expectation value of a more complicated four-site composite operator can be calculated similarly by inserting two more operators in the tensor network, which is often used to check superconducting pair-pair correlations.

Before ending this subsection, we discuss the issue about error control in the iTEBD algorithm. There are two kinds of error source in the algorithm. First, we approximate time evolution operators by a Suzuki-Trotter expansion. It is known that depending on the order of the expansion n, the error in the expansion is about dt^n. In our implementation we often choose a fourth order expansion with a varying

dt. The smallest dt in our simulation is 10^{-4} 1/(energy unit), which ensures a negligible expansion error. The other error source regards retaining a finite D states in the singular value decomposition. It can be estimated by summing the discarded weight of singular values. We can either set a tolerance value on the discarded weight and ensure a large enough D is used to meet the tolerance or check the convergence of expectation value of physical variables as we increase D. For example in this thesis we often require a ground state energy difference to be smaller than 10^{-5} in the energy unit as we increase D value. In some studies, the convergence of order parameter with increasing D value is also demonstrated.

iPEPS

The iPEPS algorithm is an extension of the iTEBD algorithm to two dimensions. Since its first introduction[44], many work have been done with this algorithm including the less studied frustrated magnetism problems. There are several advantages of the iPEPS algorithm. First it is free of sign problem such that in general it can be used to study some fermionic models where Quantum Monte Carlo fails to give a convergent results. Several works have been done on the t-J model and interacting fermions[41, 40, 43]. Second it is designed to address the problems in the thermodynamic limit. Thus no further finite size extrapolation of physical observables is needed, which is often required for the exact diagonalization method and the DMRG method. However, iPEPS method itself has some drawbacks too. One main problem is that although it scales only polynomially with the virtual dimension D, the scaling exponent is 12 on a square lattice, which is already a formidable task for a moderate value of D. Depending on the models we studied, a small D value might not be sufficient to obtain sensible results. The implementation of the iPEPS closely

follows the idea of the iTEBD. We will discuss its underlying structure, strategy in searching ground states, and computation of observables in separate paragraphs.

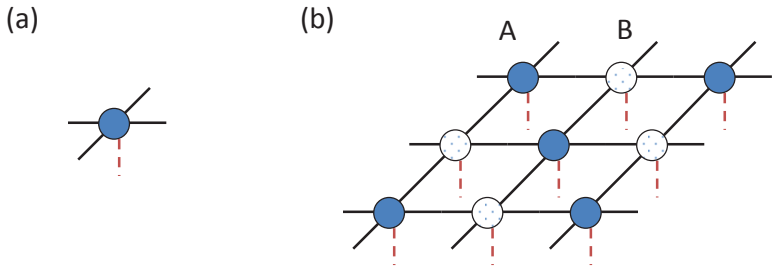

Figure 1.7: (a) A tensor with 5 legs as a basic unit in the iPEPS on a square lattice. (b) A and B tensors sit on two sub-lattices on a square lattice.

The ansatz states used in the iPEPS algorithm have a so called tensor product state(TPS) structure, which is a straightforward extension of MPS. For example we use rank 5 tensors $A_{\alpha,ijkl}$ with four virtual indices (i, j, k, l) and one physical index α on each site in a square lattice as we show in figure 1.7(a). Tensors are connected with their four nearest neighbors through virtual indices. This can be generalized to arbitrary lattice structures by simply adapting the number of virtual legs to the number of nearest neighbors in a lattice.

To address problems in the thermodynamic limit, translational symmetry is assumed in the tensor network. For simplicity we will mainly discuss the implementation in the case where there are only two different tensors A and B in a unit cell sitting on two sub-lattices of a square lattice as in figure 1.7(b). In a more general case we would need to increase the size of the unit cell to incorporate different translational symmetry breaking pattern of the system. For example it is enough to study anti-ferromagnetic states with a 2×1 unit cell. However, if we want to study a plaquette valence bond state, a 4×4 unit cell will be needed.

Similar to the iTEBD algorithm, imaginary time evolution is used for finding the ground state. The operation on 2D tensor network is similar to that in the iTEBD except we have five indices for each tensor now, which requires us to reshape a rank 5 tensor into a matrix before performing singular value decomposition. It is not surprising that the iPEPS method has a higher scaling exponent of computational complexity than its 1D companion, which is d^3D^9 in this step.

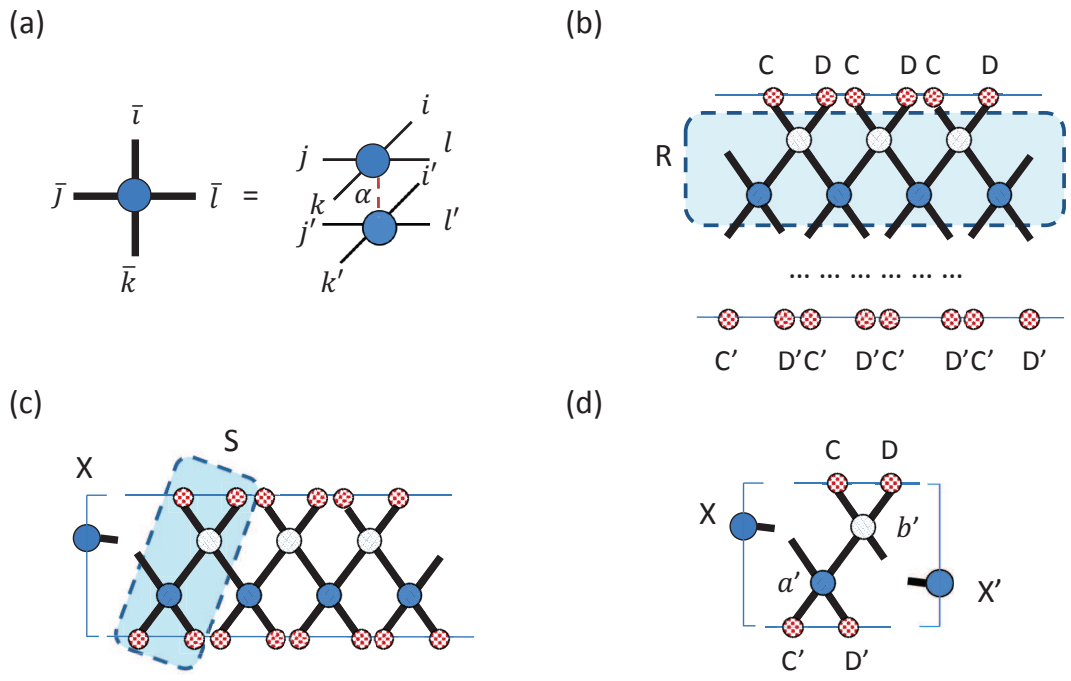

Figure 1.8: (a) a tensor in equation 1.43 obtained by contracting the physical index α of A and its conjugate. (b) Contracting the infinite tensor network to a infinite strip by finding R's dominant eigenvectors. (c) The dominant eigenvector X of S is computed. (d) $\{X, X', C, D, C', D'\}$ is used to construct the environment of a' and b' tensors. The correlation function is then computed by contracting this tensor network.

Measurement of physical observables requires evaluation of a infinite double layer tensor network made by

$$a_{\bar{i}\bar{j}\bar{k}\bar{l}} = \sum_{\alpha=1}^{d} A_{\alpha,ijkl} A^*_{\alpha,i'j'k'l'} \tag{1.43}$$

where $\bar{i}$ represents the double bond index (i, i')[44] and the physical index α is contracted as shown in figure 1.8. We introduce a set of boundary tensors $\{C, D, C', D'\}$ each of which has three indices. One index has a virtual dimension D^2, which will be contracted with the double bond $\bar{i}$ and the others have a different virtual dimension χ. The contraction is achieved by first approximating the infinite tensor network environment with an infinite strip. This is done by repeatedly contracting the tensor network with boundary tensors along one direction. In the second step the infinite strip is further contracted.

Our implementation follows the so called diagonal scheme in Ref. [44]. Here we demonstrate how to compute a nearest neighbor correlation function. General two-site correlations can be done in a similar fashion with a bit more work. We sketch the main steps in figure 1.8. In a diagonal scheme a chain of boundary tensors $\{C, D\}$ is used as upper-left boundary and boundary tensors $\{C', D'\}$ as lower-right boundary as in figure 1.8(b). The contraction of boundary tensors with $a_{\bar{i}\bar{j}\bar{k}\bar{l}}$ and $b_{\bar{i}\bar{j}\bar{k}\bar{l}}$ tensors is done by using the iTEBD algorithm with a and b tensors as time evolution operators there. We repeat this update of $\{C, D, C', D'\}$ until the convergence is reached. This is equivalent to finding both the left and the right dominant eigenvectors of the transfer matrix R consisting of a and b tensors(shaded region in figure 1.8(b)).

In the next step the contraction of the infinite strip consisting of $\{C, D, C', D', a, b\}$ tensors is done by computing the left and right dominant eigenvectors of a transfer matrix S which is a basic repeated unit in the strip as we show in figure 1.8(c). The left and right dominant eigenvectors X and X' are calculated through simple vector-matrix multiplication. We can build an effective environment from $\{C, D, C'D', X, X'\}$ tensors as in figure 1.8(d). The desired physical observables are inserted to form a'

and b' tensors as

$$a'_{\bar{i}\bar{j}\bar{k}\bar{l}} = \sum_{\alpha,\alpha'=1}^{d} A_{\alpha,ijkl} O^{r_i}_{\alpha,\alpha'} A^*_{\alpha',i'j'k'l'} \tag{1.44}$$

and

$$b'_{\bar{i}\bar{j}\bar{k}\bar{l}} = \sum_{\alpha,\alpha'=1}^{d} B_{\alpha,ijkl} O^{r_j}_{\alpha,\alpha'} B^*_{\alpha',i'j'k'l'}, \tag{1.45}$$

where r_i and r_j are site indices, which are contracted with the environment to get the correlation $\langle O^{r_i} O^{r_j} \rangle$. The computational cost scales as $O(\chi^2 D^6 d)$ in this scheme. A χ value around D^2 is often required to obtain convergent results, which leads to a scaling exponent of 12 as we mentioned earlier.

There are several other contraction schemes being used in recent works. The so-called corner transfer matrix renormalization group(CTMRG) method considers an update of boundary tensors including all tensors surrounding the a' and b' tensors rather than starting from a particular dimension.[45] A variant of CTMRG, which is called directional corner transfer matrix(CTM) method[46], was introduced later, which has a similar update scheme to CTMRG but addresses different directions independently. It is claimed that these methods have a better numerical stability and can be used to discuss physics near critical point more accurately.

1.3 Dissertation overview

In this dissertation we propose several models which could be realized with cold atoms in an optical lattice and use the tensor network algorithm to study many body physics in them. We outline the structure here.

In Chapter II, we propose to stabilize a p-wave superfluid in an optical lattice by a so-called dissipation-induced blockade mechanism. We write down an effective model to describe spinless fermions near a p-wave Feshbach resonance. The phase diagram is studied by using the iTEBD method introduced above. The work presented in

this chapter is published in Ref. [47]

In Chapter III, we propose to study a super-solid phase with dipolar atoms or polar molecules. We focus on the tunable anisotropy nature of dipole-dipole interaction which allows a repulsive interaction along one direction and an attractive interaction along the other in a two dimensional lattice. The existence of super-solid phase is demonstrated through various order parameters calculated by the iPEPS algorithm. We also map out the phase diagram at different interaction strength and confirm that there is no supersolid phase with only nearest neighbor repulsive interaction in a square lattice. The work presented in this chapter is published in Ref. [48]

In Chapter IV, we study an anti-ferromagnetic Heisenberg model on a checkerboard lattice. We demonstrate the applicability of the iPEPS algorithm on this frustrated magnetism model. The phase diagram of this model in a parameter region with a dominant next nearest neighbor exchange is still under debate. Results from different numerics and theoretical work give different possible candidate ground states. Our results agree with a semiclassical study and shows the possibility of a previous proposed ground state as a metastable state. This work is published in Ref. [49].

In Chapter V, we propose that a spin liquid phase in an optical lattice is possible through the implementation of a J_1-J_2 XY model with hard-core bosons. The required next nearest neighbor hopping is realized by dressing hard-core bosons in a spin dependent lattice with Raman laser beams. The coupling ratio J_1/J_2 is tunable over a wide range. We study the phase diagram of this model with two complementary method: the iPEPS algorithm and the exact diagonalization method. We find a spin liquid phase without any spin order and valence bond order in a region with intermediate couping strength $0.46 \leq J_2/J_1 \leq 0.54$. The results is published in

Ref. [50]

In Chapter VI, the iPEPS algorithm is applied to study the phase diagram of a quarter-filled $S = \frac{3}{2}$ fermions on the square lattice in the strong interaction regime. The effective model can be written down as a Heisenberg type model with $SO(5)$ symmetry. For a speical point in this model the iPEPS method has been demonstrated to be able to capture the ground state property in a recent study.[43] However, the complete phase diagram has not been discussed yet. Depending on the strength of the spin exchange we discover a Nêel phase, a magnetic dimer phase and a non-magnetic dimer phase.

In Chapter VII, we propose to study a topological Bose-Mott insulator phase in the optical superlattice. We find numerical evidence that repulsively interacting bosons in a superlattice sturcture can have a non-zero Chern number with edge states. We also suggest the Chern number could be measured in the cold atom experiment through the density plateaue in the harmonic traps. This work is collaborated with Professor Shi-liang Zhu in the South China Normal University. The results is published in Ref. [51].

CHAPTER II

Stablization of the p-wave superfluid state in an optical lattice

2.1 Overview

It is hard to stabilize the p-wave superfluid state of cold atomic gas in free space due to inelastic collisional losses. We consider the p-wave Feshbach resonance in an optical lattice, and show that it is possible to have a stable p-wave superfluid state where the multi-atom collisional loss is suppressed through the quantum Zeno effect. We derive the effective Hamiltonian for this system, and calculate its phase diagram in a one-dimensional optical lattice. The results show rich phase transitions between the p-wave superfluid state and different types of insulator states induced either by interaction or by dissipation.

2.2 Introduction

The observation of the s-wave superfluid state in a Fermionic atomic gas represents a remarkable breakthrough in the study of many-body physics with ultracold atoms [52, 53, 54, 55, 56]. The Feshbach resonance plays an important role in those experiments, enhancing the interatomic interaction so that the superfluid phase can be entered at a temperature that is experimentally achievable. It is of great interest

to realize the superfluid state with other pairing symmetries as well. The p-wave superfluid state is the next candidate for observation, and has attracted the interest of many experimental and theoretical groups [57, 58, 59, 60, 61, 62, 63, 64]. The p-wave Feshbach resonance has been recently observed in experiments [57, 58, 59, 60], and can push the single-component Fermi gas to the strongly interacting region and open a door towards observation of the p-wave superfluid state in this system. However, compared with the s-wave Feshbach resonance, a key difficulty with the p-wave resonance is that the inelastic collision loss in this system is typically large [57, 58, 59, 60, 65, 66], which forbids thermalization of the gas within the system lifetime [66].

In this chapter, we discuss how a dissipation-induced blockade mechanism can stabilize the p-wave superfluid state in an optical lattice in the strongly interacting region. Such a dissipation-induced blockade has been reported in recent experiments to realize the Tonks gas [67, 68] or for simulation of effective three-body interactions [69] with cold bosonic atoms. We apply this mechanism to stabilize the single-component Fermion system in an optical lattice in the presence of the p-wave Feshbach resonance. The p-wave Feshbach resonance has been considered recently on single sites in a very deep optical lattice [65, 70]. Here, instead, we focus on the many-body physics by deriving an effective Hamiltonian for this system, taking into account the atomic hopping in the reduced Hilbert space caused by the dissipation-induced blockade. This effective Hamiltonian provides a starting point to understand the quantum phases. We compute the phase diagram of the system explicitly with well-controlled numerical methods for an anisotropic lattice where the atom tunnelling is dominantly along one dimension. The results show rich phase transitions between the p-wave superfluid state, a dissipation-induced insulator state, the Mott

insulator state, and different kinds of metallic states. Although these results are obtained from one-dimensional calculations, we expect these phases to correspond also to similar phases in higher dimensions.

2.3 p-wave Feschbach resonance Fermi gas

We consider a single-component Fermi gas near a p-wave Feshbach resonance. If this strongly interacting gas is loaded into an optical lattice, many different Bloch bands can be populated, in particular when the resonance is broad (as it is the case for some recent experiments [57, 58, 59, 60]). However, we can derive an effective single-band model for this system that is independent of the interaction details. Following a strategy similar to the s-wave Feshbach resonance case [71, 72], we first analyze the local Hilbert space structure on a single lattice site. When we have zero or one atom on the site i, the states are simply denoted by $|0\rangle_i$ and $|a\rangle_i = a_i^\dagger |0\rangle_i$, respectively. For the case of two atoms on a single site, the exact two-body physics has recently been calculated [70], and there are several two-body energy levels separated by an energy difference of the order of the band gap. If we assume that the system temperature is significantly below the band gap, only the lowest two-body state is relevant. We refer to this state as a dressed molecule level, and denote it by $|b\rangle_i = b_i^\dagger |0\rangle_i$. Note that the wave function of $|b\rangle_i$ in general includes contributions from many of the original atomic orbitals [70]. It has a p-wave symmetry in space and is antisymmetric under exchange of the two atoms.

2.3.1 Dissipation induced blockade

If more that two atoms come to a single site, different from the s-wave case, the state will not be stable due to the big three-particle inelastic collision loss [65]. At first sight, this seems to mean that the system will become unstable. However, in

a lattice, there is a subtle dissipation induced blockade mechanism [67, 68] which forbids population of the unstable three-particle state and thus stabilizes the whole system. The basic idea is illustrated in Fig. 2.1. The three-particle state $|3\rangle$ has a large bandwidth characterized by its inelastic collision rate γ and an energy shift characterized by the on-site atom-dressed-molecule interaction energy Δ_3. If a single atom tunnels through a barrier with a hopping rate t to form this state $|3\rangle$, the probability of getting $|3\rangle$ is given by $t^2/\left(\gamma^2+\Delta_3^2\right)$ [67, 68] (similar to a two-level transition with a detuning Δ_3 and a bandwidth γ). So the net collisional loss of the system is bounded by $\gamma_{\text{eff}}=\gamma t^2/\left(\gamma^2+\Delta_3^2\right)\leq t^2/\left(2\Delta_3\right)$ no matter how large the inelastic collision rate γ is. Near the Feshbach resonance, the atom-dressed-molecule interaction energy Δ_3 is comparable with the lattice band gap (thus much larger than t) [73], the net collisional loss γ_{eff} is therefore small compared with the atomic hopping required to thermalize the system. As an example, for ^{40}K, the measured $1/e$ lifetime is 1 ms . If we scale this value to the lattice case with a typical depth $V_0\sim 10E_r$, the decay rate γ can be a hundred times larger than the tunneling rate t, which leads to small effective collisional loss γ_{eff} even without the detuning Δ_3 caused by interaction. The reduction of population in the noisy state $|3\rangle$ is called the dissipation-induced blockade (or interpreted as the quantum Zeno effect [67, 68]; the blockade is actually induced by both dissipation and interaction when Δ_3 and γ are comparable). Due to this mechanism one can achieve many-body thermal equilibrium in a lattice even if there is large inelastic collision loss.

2.3.2 Effective Hamiltonian

Due to the dissipation-induced blockade discussed above, on each site we have only three relevant levels: $|0\rangle_i, |a\rangle_i,$ and $|b\rangle_i$ as the low energy configurations. The

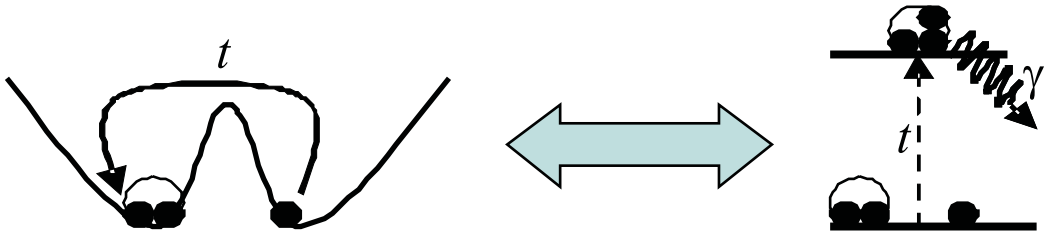

Figure 2.1: Illustration of the dissipation-induced blockade for multiple occupation (more than two) of a single lattice site. Similar to a two level transition with a detuning Δ_3 and a decay rate γ for the target level, the effective loss rate of the system is suppressed by a factor $t^2/(\gamma^2+\Delta_3^2)$, where t is the atomic tunneling rate.

energy difference between the sates $|a\rangle_i$ and $|b\rangle_i$ can be tuned with the external magnetic field via the Feshbach resonance. We then take into account the atomic hopping, which changes the level configurations of the neighboring sites under the constraint that the atom number be conserved. Thus, there are only three possible processes, as illustrated in Fig. 2.2. Corresponding to these configuration changes, the general Hamiltonian for this lattice system then takes the form

$$\begin{aligned} H = & \sum_i \left[(\Delta b_i^\dagger b_i - \mu(a_i^\dagger a_i + 2b_i^\dagger b_i)\right] \\ & - \sum_{\langle i,j\rangle} P\left[t_1 a_i^+ a_j + t_2(b_i^+ b_j^+)a_i a_j + t_3 b_i^+ b_j a_j^+ a_i + H.c.\right] P, \end{aligned} \tag{2.1}$$

where μ is the chemical potential and Δ is the energy detuning of the dressed molecule controlled with the magnetic field. The value of Δ characterizes the on-site atomic interaction magnitude. The hopping rates for the three processes illustrated in Fig. 2.2 are different, in general, due to the contributions from different bands (because the dressed molecule is a composite particle with population in multiple bands). The hopping takes place in the low energy Hilbert space specified by the projector $P \equiv \bigotimes_i (|0\rangle_i \langle 0| + |a\rangle_i \langle a| + |b\rangle_i \langle b|)$, and the summation in Eq. (1) is over all neighboring sites $\langle i,j\rangle$.

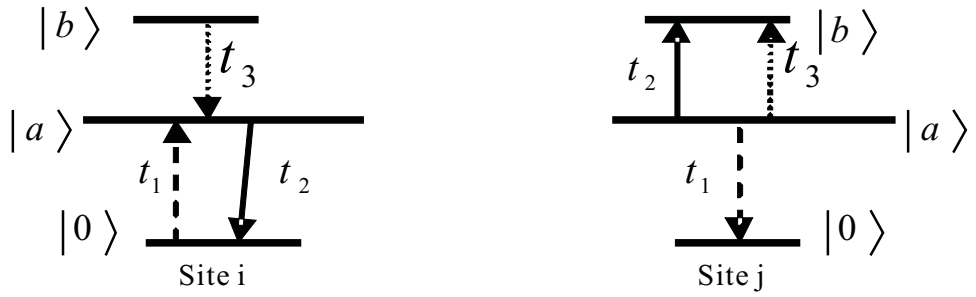

Figure 2.2: Illustration of different atomic hopping processes over the two neighboring sites described by the Hamiltonian (1), where each site has only three possible level configurations.

2.4 Numerical Simulation

The Hamiltonian 2.1, although much simplified compared with multi-band models, is still complicated, and in general it does not allow exact solutions. To understand some basic physical properties of the system, we limit ourselves in the following to the one-dimensional lattice where the atomic hopping along the other two dimensions are turned off with a high lattice barrier. In this case, we can solve this model with well controlled numerical simulations, and the results show rich phase transitions between the p-wave superfluid state and different kinds of insulator and metallic phases. We expect most of the phases found in the one-dimensional case have counterparts in higher dimensions. In particular, the p-wave superfluid state characterized by a quasi-long-range order with diverging pair susceptibility in one dimension can be easily stabilized to a true long-range order if we allow weak tunneling between the one-dimensional tubes [74, p.275 452].

We use the iTEBD algorithm, a recently developed method related to density matrix renormalization group techniques [38, 75], which allows direct calculation of the physical properties in the thermodynamic limit. Typically, the virtual dimension we used is up to 80 in order to limit cut-off errors to $\sim 10^{-5}$. The algorithm has been

shown to work with high precision compared to known results for the Hubbard model [76]. For simplicity, we take the hopping rates $t_1 = t_2 = t_3 = t$(Although t_1,t_2, and t_3 are different in the strongly interacting region, the recent results indicates their difference is not large and the phase diagram obtained here applies qualitatively to the case with slightly different t_i), and use t as the energy unit. Then we have effectively only two parameters, Δ and μ (in units of t) in the Hamiltonian 2.1. To figure out the complete phase diagram with respect to these two parameters, we calculate $\partial \langle H \rangle / \partial \Delta$ and $\partial \langle H \rangle / \partial \mu$ as functions of Δ or μ for the ground state of H, and use the characteristics of these curves to identify the phase transition points.

2.4.1 Dissipation induced insulator and p-wave superfulid

In Fig. 2.3, we show $\overline{n}_b = \left\langle b_i^\dagger b_i \right\rangle$ and $\overline{n}_a = \left\langle a_i^\dagger a_i \right\rangle$ as functions of Δ and μ. One can clearly see several quantum phase transitions from this figure. First, with a fixed chemical potential $\mu = -0.5t$, one has $\overline{n}_b = 1$ and $\overline{n}_a = 0$ with a large negative detuning Δ (corresponding to strong attractive atomic interaction). In this case, each site is doubly occupied with two atoms. More than two atoms cannot move to the same site because of the dissipation-induced blockade. So this is an insulator phase stabilized by the dissipation. As one increases Δ with $\Delta > -2.15t$, the number of atoms on each site begins to fluctuate. If one looks at the pair correlation $\left\langle b_i^\dagger b_j \right\rangle$, it shows quasi-long-range behavior with slow algebraic decay. In Fig. 2.4(a), we show this correlation in the k-space, defined as $P_k = (1/N) \sum_{\rho=0}^{N} \left\langle b_i^\dagger b_{i+\rho} \right\rangle e^{ik\rho}$. The correlation P_k is peaked sharply at $k = 0$. This corresponds to the p-wave superfluid phase. The p-wave character is inherited from the p-wave symmetry of the dressed molecule in space b_i (or the atomic pair on the same site). The p-wave nature of the pairing is also manifested in the atomic pair wavefunction at different sites $\langle a_i a_j \rangle$,

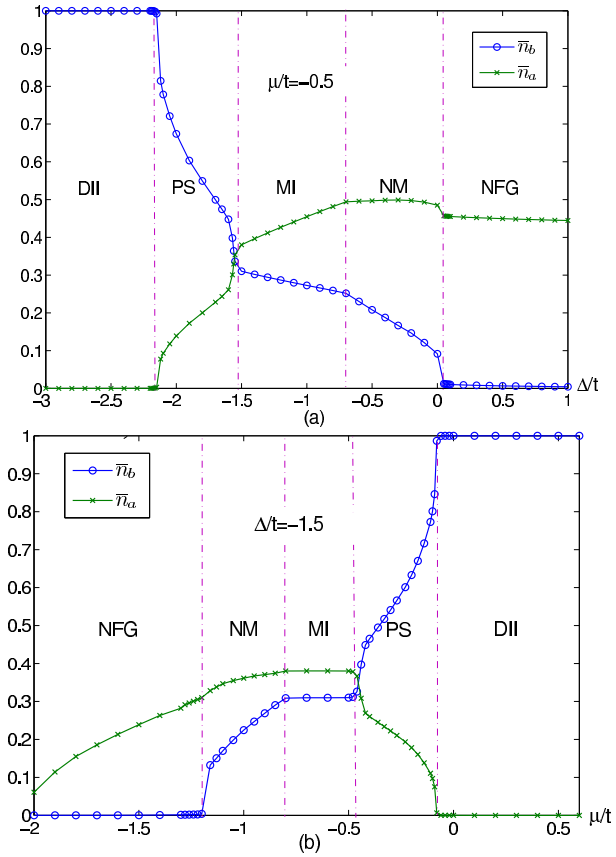

Figure 2.3: The dressed molecule number $\overline{n}_b$ (the double occupation probability) and the atom number $\overline{n}_a$ (the single occupation probability) shown as the function of Δ/t (with a fixed $\mu/t = -0.5$) in (a) and μ/t (with a fixed $\Delta/t = -1.5$) in (b). The non-analyticities of these curves signal a number of quantum phase transitions from the dissipation induced insulator state (DII), to a p-wave superfluid state (PS), to a Mott insulator state (MI), to a normal mixture state (NM), and finally to normal Fermi gas phase (NFG).

which is obviously antisymmetric under exchange of the sites. In the one-dimensional case, the p-wave superfluid state is characterized by a quasi-condensate of the atomic pairs with a diverging pairing susceptibility. If one allows weak coupling between the one-dimensional tubes in the optical lattice, the p-wave quasi-condensate can easily be stabilized into a real condensate with a true long range pairing order.

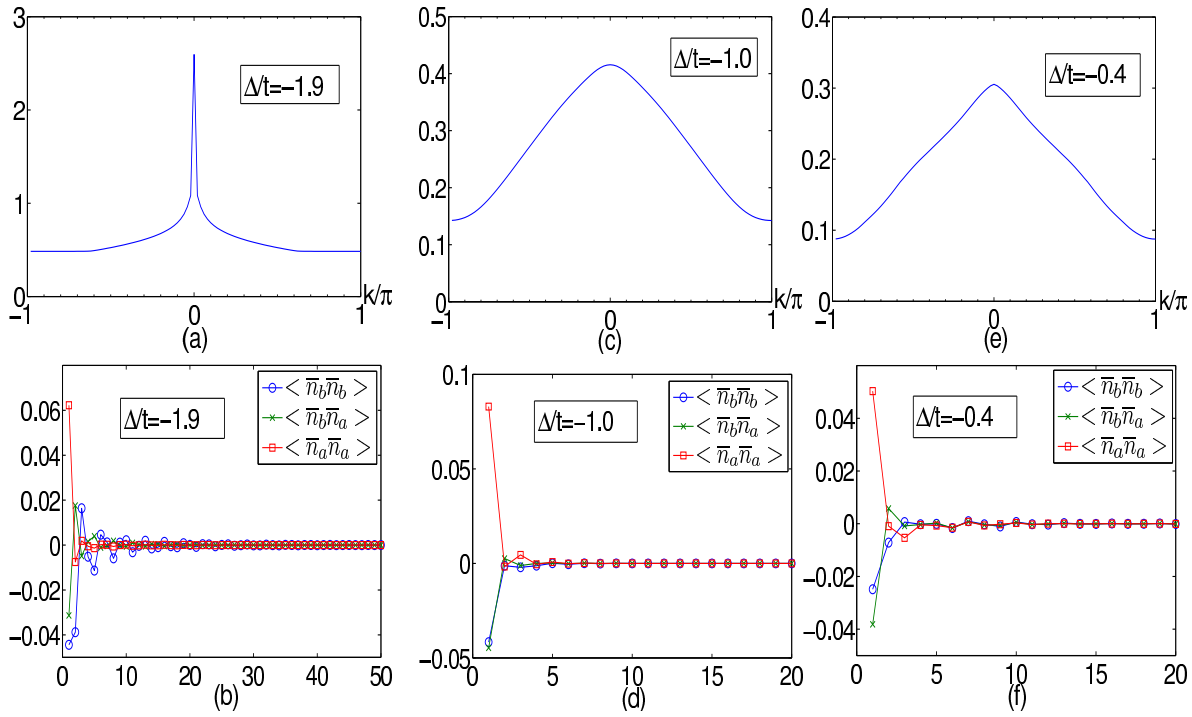

Figure 2.4: The correlation functions shown for the p-wave superfluid phase (a) and (b), the Mott insulator phase (c) and (d), and the normal mixture phase (e) and (f). Figures (a), (c) and (e) show in k-space the Fourier transform P_k of the pair correlation $\left\langle b_i^\dagger b_j \right\rangle$. Figures (b), (d) and (f) show the charge density correlations of $\langle n_{bi} n_{bj} \rangle$, $\langle n_{bi} n_{aj} \rangle$ and $\langle n_{ai} n_{aj} \rangle$ in real space. We take $\mu/t = -0.5$ for all the figures.

2.4.2 Mott insulator, mixture gas and single-component gas

If one further increases Δ in Fig. 2.3(a), one enters a phase where the total particle number per site $n = 2\overline{n}_b + \overline{n}_a$ is fixed at 1 (although the double occupation probability $\left\langle b_i^\dagger b_i \right\rangle$ varies with Δ). This is a Mott insulator state with a finite gap to charge excitations. This can be seen more clearly in Fig. 2.3(b), where we fix the detuning Δ, and show $\overline{n}_b$ and $\overline{n}_a$ as functions of the chemical potential μ. For this phase, the number density does not vary with μ, so the system is incompressible as one expects for a Mott insulator phase. The correlation functions for this phase is shown in Fig. 2.4, where both the pair correlation and the charge density wave correlations are of short range. As one further moves to the right side in Fig. 2.3(a),

there are two other phases: the normal mixture (NM) and the normal free gas (NFG). Both of these two phases are of a metallic nature with a finite compressibility (see Fig. 2.3(b)). The difference is that in the normal mixture phase, some sites are doubly occupied (with a finite $\left\langle b_i^\dagger b_i \right\rangle$). Several kinds of correlation functions for the normal mixture phase are shown in Fig. 2.4, and all of them decay rapidly with distance. In the NFG phase, the double occupation probability $\left\langle b_i^\dagger b_i \right\rangle$ reduces to zero, and one has a conventional single component free Fermion gas.

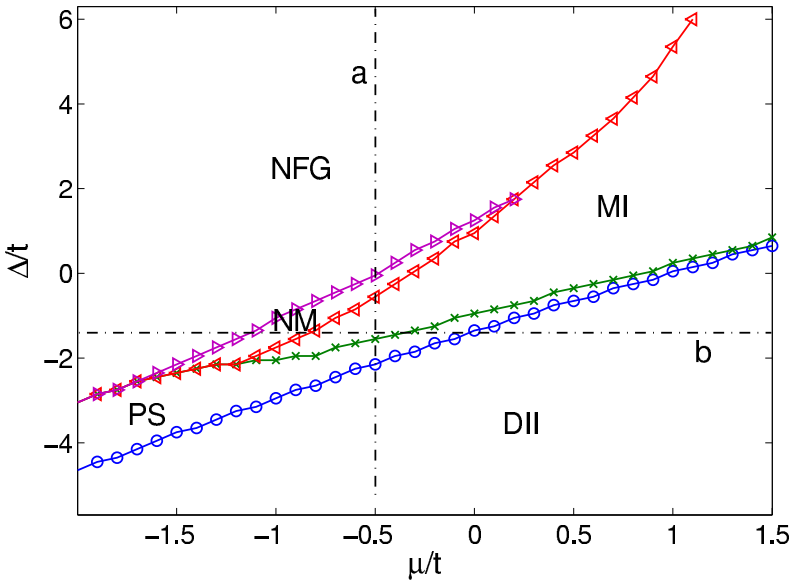

Figure 2.5: The complete phase diagram of the system versus two parameters μ/t and Δ/t. The five different phases are marked with the same notation as in Fig. 2.3. The black dashed lines a and b correspond to the parameters taken in Fig. 2.3(a) and Fig. 2.3(b).

2.4.3 Phase diagram

We have calculated the phase transition points for all Δ and μ, and the result is summarized in Fig. 2.5 to give a complete two-parameter phase diagram. The five different phases are marked there. Under real experimental conditions, there is typically a weak global harmonic trap in addition to the optical lattice potential. As one moves from the trap center to the edge, the effective chemical potential μ

gradually decreases under the local density approximation. So with a fixed interaction parameter Δ, a line in the phase diagram of Fig. 2.5 across different μ gives the phase separation pattern of the Fermi gas in a harmonic trap. With a large positive Δ, one has a Mott insulator state in the middle, surrounded by a normal Fermi gas. The phase transitions are most rich for small $|\Delta|$, where one can cross all the five different phases from the trap center to the edge. For large negative Δ, the region of the p-wave superfluid state increases, but the Mott insulator and the normal mixture states eventually disappear when $\Delta < -3t$. As the p-wave superfluid state has a large stability region in the phase diagram, such a phase can be prepared experimentally by adiabatically ramping the Hamiltonian parameters following certain trajectories that suppress the three-particle occupation [69, 77].

2.5 Chapter Summary

We suggest that the p-wave superfluid state near a Feshbach resonance can be stabilized in an optical lattice through a dissipation-induced blockade mechanism. We have derived the effective Hamiltonian for this system, and solved it in a one-dimensional lattice. The result shows a rich phase diagram.

CHAPTER III

Supersolid and charge-density-wave states from anisotropic interaction in an optical lattice

3.1 Overview

We show that anisotropy of the dipole interaction between magnetic atoms or polar molecules can stabilize new quantum phases in an optical lattice. Using the iPEPS tensor network algorithm based on the tensor network algorithm, we calculate the phase diagram of the resultant effective Hamiltonian in a two dimensional square lattice: an anisotropic Hubbard model of hard-core bosons with attractive interaction in one direction and repulsive interaction in the other direction. Besides the conventional superfluid and the Mott insulator states, we find the striped and the checkerboard charge-density-wave states and the supersolid phase that interconnect the superfluid and the striped solid states. The transition to the supersolid phase has a mechanism different from the case of the soft-core Bose-Hubbard model.

3.2 Introduction

The remarkable experimental realization of ultracold dipolar molecules [78, 79] and ultracold atoms with large magnetic moments [80, 81] opens up possibilities of probing novel phases of matter that are induced by strong dipole-dipole interaction.

Among these possibilities, a particularly interesting one is the supersolid phase, where superfluidity coexists with a charge density wave order [82]. In a square lattice, the supersolid state has been predicted to exist for soft-core bosons if the off-site interaction gets comparable with the on-site interaction [83]. For ultracold atoms, it is challenging to experimentally realize this condition, as even with the long-range dipole interaction, the interaction strength still falls off quickly with distance. In an optical lattice, the on-site interaction is typically much larger than the off-site interaction, and if one increases the interaction strength (or equivalently reduces the atomic tunnelling rate), one enters the hard-core boson region where each site can only have one or zero atoms due to the interaction blockade. For hard-core bosons in the conventional square lattice, with only the neighboring interaction, the supersolid state can not be stabilized [84], and one has to rely on more unusual interaction configurations (such as a Hamiltonian with strong next-nearest-neighbor interaction [85]) or lattice geometry (such as a triangular lattice [14]) to stabilize such a phase. A recent interesting study based on a quantum Monte Carlo simulation has shown, however, with true long-range interaction that falls off with distance by the cubic form, the supersolid state can be stabilized for hard-core bosons in a square lattice [86]. As the supersolid state can not be stabilized by the neighboring interaction alone, the small energy scale associated with the long-range tail of the dipole interaction clearly plays an important role in determining the stability region of the supersolid state in that case.

The dipole interaction has two characteristic features: first, it is relatively long-range; and second, the interaction form is anisotropic in space. Ref. [86] has shown that the long range tail of the dipole interaction, even under an isotropic interaction form, can lead to stabilization of the supersolid state. Complementary to this

research, in this chapter we show that by tuning the anisotropy of the dipole interaction, we can stabilize a supersolid state even if we neglect the small long range tail of the dipole interaction. The supersolid state here is of a different type compared with the case studied in [86] as we have a stripe instead of a checkerboard density-wave order. The anisotropy of the dipole interaction has been analyzed recently under a mean-field treatment of the Hamiltonian for the soft-core bosons [87, 88]. The mean-field approximation, however, typically overestimates the stability region of the supersolid state. For instance, it would predict a checkerboard supersolid state for hard-core bosons in a square lattice, which is actually unstable to quantum fluctuation [84]. In this paper, we use instead iPEPS tensor network algorithm to calculate the phase diagram of hard-core bosons in a two-dimensional square lattice. We construct quantitative phase diagrams under different interaction parameters, and analyze the properties of the transition from the striped solid phase to the supersolid state. The transition has a mechanism different from the case of the soft-core Bose Hubbard model [83].

3.3 Dipolar molecules with anisotropic interaction

We consider a system where bosonic dipolar molecules (or magnetic atoms) are confined to a two-dimensional (2D) optical lattice, denoted here as $x-z$ plane. Initially the orientation of the external field is controlled such that all the dipoles point to the y axis. The strength of the dipole-dipole interaction depends on θ_{ij} ,the angle between the orientation of the dipole moments and their relative positions, as $(1-3cos^2\theta_{ij})$. Thus we have isotropic repulsive interaction at the beginning when the direction of the dipole is perpendicular to the $x-z$ plane ($\theta_{ij}=\pi/2$). Due to the strong repulsive dipole interaction, we assume the system is in the hard-core boson

region with each site occupied by less than one molecule. Then we adiabatically tune the direction of the external field towards the $x-z$ plane to change the anisotropy of the dipole interaction. Depending on the angle θ_{ij}, the interaction may get attractive along one direction and repulsive along the other direction. With the attractive interaction, one may expect that more than one bosons can occupy the same site for the ground state. There is also concern about stability of the system under the attractive interaction. However, as we start with a configuration with no double occupation, the energy shift Δ from the strong on-site interaction forbids two bosons jumping to the same site due to the energy conservation. This is true independent of the sign of Δ, as long as its magnitude $|\Delta|$ is much larger than the atomic tunnelling rate. In addition, the possible instability of the double occupation (or multiple occupation) states will further suppress the probability of double occupation due to the dissipation-induced blockade mechanism (the quantum Zeno effect) [67, 68]. As a net result, when we tune the interaction to the attractive region, the system remains stable in an optical lattice and still stays in the hard-core boson region with negligible double occupation. As the dipole interaction falls off with distance pretty quickly by the cubic law, in this paper we keep the off-site interaction only to the order of nearest neighbors. So the focus of investigation here is on new properties induced by the anisotropy of the dipole interaction, not by its small long-range tail.

3.3.1 Effective spin Hamiltonian

The Hamiltonian of this system can then be described as hard-core bosons on a 2D square lattice with anisotropic nearest neighbor interactions

$$H = -\sum_{\langle i,j\rangle} t(b_i^\dagger b_j + h.c.) - \sum_i \mu b_i^\dagger b_i + \sum_j (V_x n_j n_{j\pm\hat{e}_x} + V_z n_j n_{j\pm\hat{e}_z}) \tag{3.1}$$

, where b_i^+ is the boson creation operator at site i, $n_i = b_i^+ b_i$, t is the atomic tunnelling rate over the nearest neighbors $\langle i,j\rangle$, μ is the chemical potential, and V_z (V_x) are respectively the nearest neighbor interaction rates in the z (x)-direction.

The hard-core bosons live in a truncated Hilbert space spanned by only two states $|0\rangle$ and $|1\rangle$, representing respectively zero or one boson on a site. The commutation relation of the hard-core boson operators is thus modified to $\left[b_i, b_i^+\right] = |0\rangle\langle 0| - |1\rangle\langle 1| = 1 - 2n_i$. With the well known mapping of the hard-core boson operators to the Pauli operators through $b_i^+ \to \sigma_i^+$ and $2n_i - 1 \to \sigma_i^z$, the hard core boson Hamiltonian in Eq. 3.1 is equivalent to the following anisotropic XXZ model

$$H = -\sum_{\langle i,j\rangle} J_{xy}(\sigma_i^x\sigma_j^x + \sigma_i^y\sigma_j^y) + \frac{V_x}{4}\sum_j \sigma_j^z\sigma_{j+\hat{e}_x}^z + \frac{V_z}{4}\sum_j \sigma_j^z\sigma_{j+\hat{e}_z}^z - h\sum_j \sigma_j^z, \tag{3.2}$$

where $J_{xy} = 2t$ and $h = \mu/2 - 2$. The chemical potential μ acts as an effective magnetic field along the z direction in the resulting XXZ model. With different signs of V_x and V_z, one can have ferromagnetic coupling in one direction and anti-ferromagnetic coupling in the other direction.

3.4 iPEPS calculation

We numerically study the phase diagram of this Hamiltonian by using the iPEPS algorithm [44]. The iPEPS algorithm is an extension of the well-known DMRG

(density-matrix renormalization group) method to 2D quantum systems. It is a variational approach based on the tensor network states (or called the PEPS states) that appropriately capture the entanglement structure of the 2D quantum systems. The iPEPS algorithm has been tested to work reliably for a number of 2D many-body models [89, 90]. We have tested our numerical codes for implementation of the iPEPS algorithms by comparing our calculation results with the known results for several many-body models, including the 2D Ising model with a transverse field and the XXZ model. The results are in quantitative agreement with the previous quantum Monte Carlo simulation and the PEPS calculation from other groups [89, 90], and the phase transition points can be determined with a pretty good precision (the relative error is typically about or within a percent level with $D = 4$). So we expect that with the same algorithm, we can reliably determine the phase diagram of the anisotropic XXZ model shown in Eq. (2). In our simulation, we use a bond dimension with $D = 4$ or 5 for the variational tensor network states and a large enough cutoff dimension χ (typically of the order of D^2) in contraction of the tensor network states to ensure converge of the ground state energy.

3.4.1 Convergence test

For an iPEPS algorithm, there are three sources of numerical errors. First, we have error from Trottor expansion of the time evolution operator [44]. This error can be reduced by choosing a small time step. Typically, in our simulation the final time step size is 10^{-5} (in the unit of the inverse of the atomic tunneling rate), which assures that the Trotter decomposition error is negligible. The other two sources of errors come from cutoff of the internal dimension D of the tensors to represent the tensor-network state and the internal dimension χ of the matrix product state to

calculate the contraction of the tensor network. For a given tensor network with the internal dimension D, we increase the cut-off dimension χ so that the convergence in the energy and the matrix element has been well achieved (with the relative error less than 0.1%). In Fig. 3.1, we show the convergence of the ground-state energy and a matrix element as a function of χ for a typical set of parameters of the Hamiltonian 3.1, where the convergence has been achieved already for a pretty moderate χ.

In numerical simulation, we vary the tensor dimension D from 2 to 5 (the calculation time gets too long beyond $D = 5$). In Fig. 3.1, we can see that the ground state energy decreases monotonically as D increases. There is a noticeable improvement of the ground state energy as D increases from 2 to 3, but as D further increases from 3 to 5, the improvement in the ground state energy has been less than 0.1%. For the matrix element $\left\langle b_i^\dagger b_{i+1} \right\rangle$ (which corresponds to the energy gradient with respect to the tunneling rate t, and is involved in calculation of the phase diagram), there is a noticeable difference between the values for the $D = 4$ and $D = 5$ cases, but this difference is still about a percent level. We expect that the relative errors of our following phase diagrams have a similar level of error amplitudes. This is further supported by comparison of the phase diagrams for the conventional XXZ model from the iPEPS calculation and from quantum Monte Carlo simulation (our simulation results are identical to those shown in Fig. 5 of Ref. [90], and thus not shown here to avoid overlap), where the relative error in the phase boundary is also within (or about) a percent level.

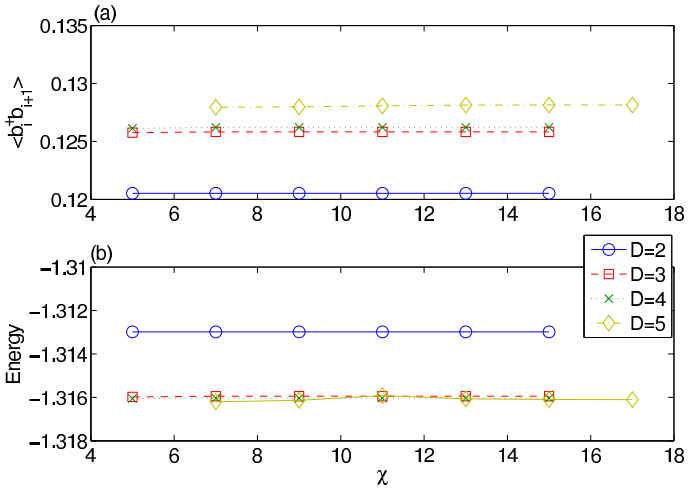

Figure 3.1: (a) Nearest neighbor correlation function and (b) Ground state energy (in the unit of hopping rate t) as functions of the cut-off dimension χ with different internal dimensions D for the tensor network states. The calculation is for the Hamiltonian 3.1 with parameters $V_x = 6t$, $V_z = -t$, and $\mu = 4t$.

3.4.2 Phase diagram

A typical phase diagram of the Hamiltonian 3.1 from the iPEPS calculation is shown in Fig. 3.2. We take $t = 1$ as the energy unit and scan over different μ and V_x with a fixed V_z. To identify different phases, we calculate the superfluid order parameter $\langle b_i \rangle$ and the boson occupation number $\langle n_i \rangle$ at different sites as functions of μ and V_x. These curves show different characteristic behaviors and we can use them to identify different phases.

Fig. 3.2 shows the phase diagram when V_z is fixed at $-t$ and V_x is scanned over the positive region. First, we note in Fig. 3.2 there is a large region of the charge density wave state at exactly half filling, which has a stripe order. This phase can be easily understood: with negative V_z and positive V_x, at half filling the particles arrange themselves into stripes along the z direction to maximize the neighboring interaction along the z direction and simultaneously minimize the repulsive coupling along the x direction. The most interesting feature from Fig. 3.2 is that the stripe phase is always

surrounded by a finite region of the supersolid state that interconnects the superfluid phase and the charge density wave state. The supersolid state here is characterized by coexisting of the superfluid order and the stripe charge density wave order. The optimal condition to get the supersolid state is to have V_z negative and comparable with the tunnelling rate t in magnitude.

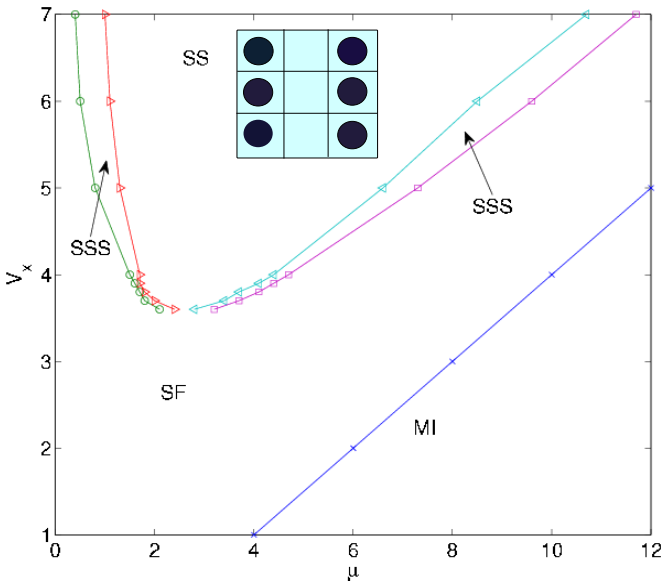

Figure 3.2: Zero-temperature Phase diagram of the extended Bose Hubbard model with anisotropic interaction shown in Eq. 3.1 for $V_z = -t$. As one varies the chemical potential μ and the interaction rate V_x (both in the unit of the hopping rate t), four different phases are observed, including the superfluid (SF) phase, the striped solid (SS) phase, the striped supersolid (SSS) phase, and the Mott insulator (MI) state. The inset shows schematically the particle filling pattern in the striped solid phase.

3.4.3 Order parameter profiles

To better understand the transition to the supersolid state, in Fig. 3.3 we show the evolution of the superfluid order parameter $\langle b_i \rangle$ and the particle occupation number $\langle n_i \rangle$ at two alternating sites i and $i+1$ along the x direction as we scan the chemical potential μ. Starting from a striped solid state at half filling, we enter the supersolid phase with either particle or hole doping. When we add particles to the half filled lattice (with increase of the chemical potential), while the occupation

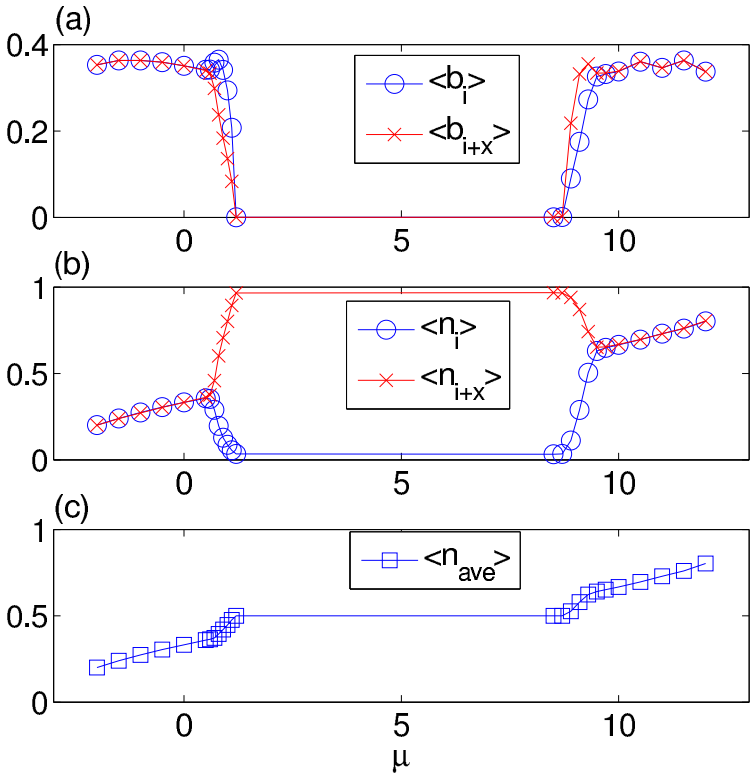

Figure 3.3: The order parameters and the filling numbers as functions of the chemical potential. (a) The superfluid order parameters $\langle b_i \rangle$ and $\langle b_{i+\hat{x}} \rangle$ at two alternating sites along the x-direction (the direction perpendicular to the stripes). (b) The filling number (the particle per site) $\langle n_i \rangle$ and $\langle n_{i+\hat{x}} \rangle$ at two neighboring sites along the x-direction. (c) The average number per site $\langle n_{ave} \rangle = (\langle n_i \rangle + \langle n_{i+\hat{x}} \rangle)/2$. The interaction parameters in these figures are taken as $V_x = 6t$ $V_z = -t$. The kinks in Figs. (a)-(c) mark two continuous phase transitions from the superfluid to the supersolid and then to the striped solid phase.

of the initially empty sites increases, the average occupation of the initially filled sites (which form the stripes) continuously decreases. This shows that with particle doping, some particles need to move from the initially filled stripes to the empty sites to build up the superfluid order. As the superfluid order increases, the charge density wave order continuously decreases and eventually vanishes, and one enters the normal superfluid phase. The transitions from the stripped solid phase to the supersolid and from the supersolid to the superfluid phase are both of the second order characterized by kinks in the first-order derivatives of the ground state energy.

We have a similar picture of the supersolid transition at the side of the hole doping where we exchange particles with holes.

This picture of the supersolid transition is different from the mechanism of the supersolid state for soft-core bosons in a lattice with large neighboring interaction [83]. In the latter case, starting with a checkerboard lattice at half filling, the supersolid phase only appears with particles doping (no supersolid with hole doping), and as one adds particles, these added particles continuously go to the already filled sites to maintain the checkerboard order. As one increases the chemical potential, the occupation of the initially filled sites continuously increases for the checkerboard supersolid phase (instead of the decrease for the stripped supersolid phase discussed above).

3.4.4 Superfluid and density-density correlations

In the supersolid state, we can look at both the superfluid and the density-density correlations, and these correlations are shown in Fig. 3.4. The superfluid density is not homogeneous in space. In Fig. 3.4(a), we can see that along the x direction (perpendicular to the stripe direction), the superfluid correlation shows the zigzag pattern, but it is extended to long range. Along the stripe (z) direction, the superfluid correlation is monotonic and approaches a constant nonzero value. This constant value, however, is different for the particle-dominated and the hole-dominated stripes. When the filling number is less than one half (hole doping to the stripe solid state), the superfluid density is larger in the particle-dominated stripes. The reverse is true for the supersolid state with the filling number larger than one half (see Fig. 3.4(c)). The density-density correlation is shown in Fig. 3.4(a), which shows a long-range zigzag pattern along the x direction, but with constant correlation along

the stripes (z direction) as the density distribution along the stripes is homogeneous.

3.4.5 Stability of the supersolid phase

In the phase diagram shown in Fig. 3.2, one can see that both the stripe solid state and the supersolid phase disappear when the repulsive interaction along the x direction becomes weak. As a result, there is only the conventional superfluid to the Mott insulator transition, and the stripe phase at half filling becomes unstable. This instability can be intuitively understood as follows: assume we have a stripe phase, and we move one particle from the filled stripe to the empty stripe to form a particle-hole excitation. The cost in the interaction energy is given by $2V_x - 2V_z$. At the same time, as the particle and the hole can freely move, the kinetic energy is lowered by an amount $8t$. The net energy cost is positive when $2V_x - 2V_z - 8t > 0$, and in this case the stripe phase is stable. Otherwise, the freely-moving particle-hole pairs will be continuously generated to form a superfluid phase and the stripe phase loses its stability. With this simple estimate, we see that for $V_z = -t$, the stripe phase becomes unstable when $V_x < 3t$, which roughly agrees with the accurate calculation of the boundary of the phase diagram shown in Fig. 3.2. This simple estimate also applies to the cases with different V_z. For instance, in the phase diagrams shown in Fig. 3.5 for different values of V_z, the point where the charge wave density (solid) phase loses its stability at half filling can still be roughly estimated by $V_x < V_z + 4t$.

As we increase or decrease the interaction V_z away from its optimal value around $-t$, the region of the supersolid phase gets smaller. With a stronger attractive interaction (larger $|V_z|$), the stripe solid phase gets larger in the phase diagram, however, the intermediate supersolid phase, which requires a careful balance of the interaction energy and the kinetic energy to enable coexistence of both the superfluid

and the charge-density wave orders, cannot be stabilized in this case. We have a direct transition from the superfluid phase to the striped solid phase. The evolution of the corresponding order parameter is shown in Fig. 3.6, which indicates that this transition is of the first order. With a weaker V_z, the supersolid region also gets smaller. As we turn off V_z or scan V_z to the positive region, the charge-density wave state at half filling has a checkerboard order instead of a stripe order. For the transition from the superfluid phase to the checkerboard solid phase, we do not find any supersolid state in the intermediate region. This finding is consistent with the result from quantum Monte Carlo simulation of the XXZ model in a square lattice (which corresponds to a particular case of the Hamiltonian 3.2 with isotropic coupling $V_z = V_x > 0$), which shows that the supersolid phase predicted by the mean-field theory is unstable to quantum fluctuation [84]. The evolution of the order parameters as functions of the chemical potential follow very similar curves as those shown in Fig. 3.6, and the transition from the superfluid to the checkerboard phase is also of the first-order.

3.5 Chapter Summary

We have shown that anisotropy of the dipole interaction between magnetic atoms or polar molecules can stabilize new quantum phases in an optical lattice. By tuning the orientation of the external field, we argue that the system can be described as a extended hard-core Bose-Hubbard model with attractive interaction along one direction and repulsive interaction along the other direction in a two-dimensional square lattice. Starting from appropriate initial states, the insatiability and the atom clustering associated with the attractive interaction can be overcome in an optical lattice through the blockade effect induced by both the atomic interaction and the

collision loss. Using a well controlled numerical method based on the tensor network algorithm, we calculate the phase diagram of the extended hard-core Bose-Hubbard model with anisotropic interaction, and find a significant region of the supersolid phase that interconnects the striped solid phase at half filling and the conventional superfluid state. The properties of the supersolid phase and the corresponding phase transitions are discussed and characterized through calculation of various kinds of correlation functions.

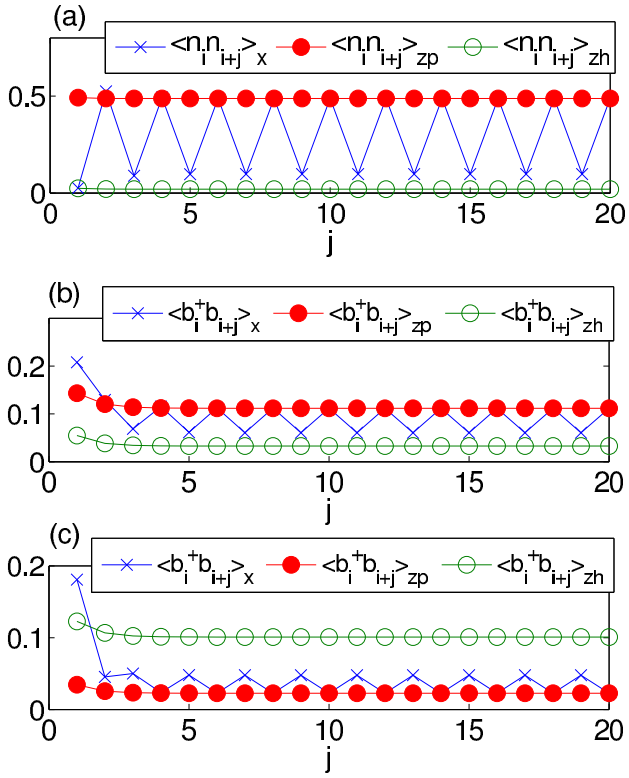

Figure 3.4: The density-density and the superfluid correlations in the supersolid phase. (a) and (b) are for the supersolid phase with hole doping to the striped solid state at half filling (with the parameters $V_z = -1$, $V_x = 6$, and $\mu = 0.9$ in the unit of the hopping rate t). The density-density (a) and the superfluid (b) correlations are shown along the x and the z directions, distinguished by the subindeces x (along the x-direction), zh (along the hole dominated stripe in the z direction), and zp (along the particle dominated stripe in the z direction). (c) represents the corresponding superfluid correlations for the supersolid phase with particle doping to the stripe solid phase (with the parameters $V_z = -1$, $V_x = 6$, and $\mu = 9.1$). One can see that with the hole doping, the superfluid correlation is stronger along the particle dominated stripe; the reverse is true for the case of the particle doping.

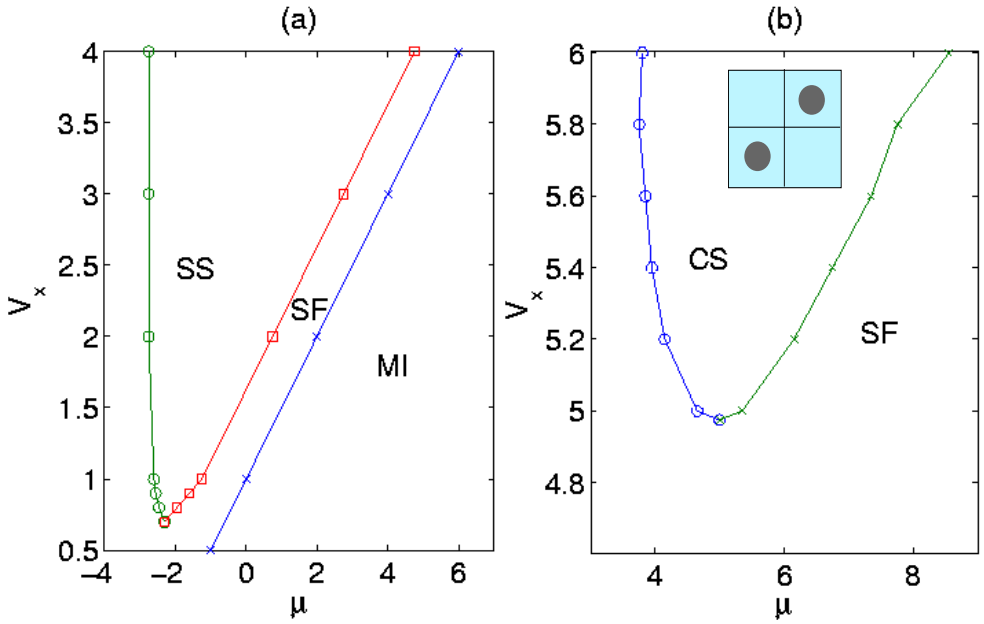

Figure 3.5: Phase diagram of the Hamiltonian 3.1 with interaction rate $V_z = -3$ for (a) and $V_z = 0$ for (b) (in the unit of the hopping rate t). There is no supersolid phase in either of these two cases. At half filling, one has a striped solid phase for (a) and a checkerboard solid phase for (b). The inset in (b) shows schematically the particle filling pattern in the checkerboard phase.

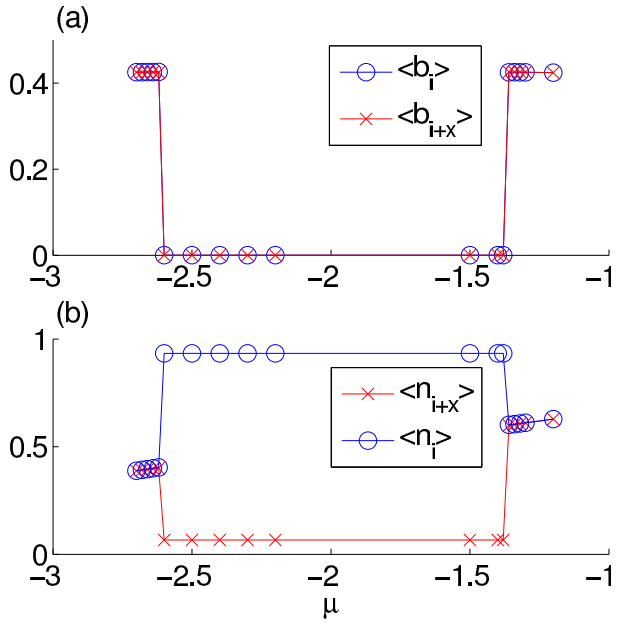

Figure 3.6: The superfluid (a) and the charge density wave (b) order parameters are shown as functions of the chemical potential μ for the phase diagram shown in Fig. 3.4 with the interaction parameters $V_x = 1$ $V_z = -3$ (in the unit of the hopping rate t). Notations have the same meaning as in Fig. 3.2. The transition from the superfluid to the striped solid phase is clearly of the first order.

CHAPTER IV

iPEPS study of anti-ferromagnetic Heisenberg model on the checkerboard lattice

4.1 Overview

We use the recently developed tensor network algorithm based on infinite projected entangled pair states (iPEPS) to study the phase diagram of frustrated anti-ferromagnetic $J_1 - J_2$ Heisenberg model on a checkerboard lattice. The simulation indicates a Nêel ordered phase when $J_2 < 0.88J_1$, a plaquette valence bond solid state when $0.88 < J_2/J_1 < 1.11$, and a stripe phase when $J_2 > 1.11J_1$, with two first-order transitions across the phase boundaries. The calculation shows that the cross dimer state proposed before is unlikely to be the ground state of the model, although such a state indeed arises as a metastable state in some parameter region.

A cold atom simulator of this model would be an interesting future direction, which might help resolve the true ground state in the large J_2 limit. However, there are several difficulties in the realization of this model. First, the superexchange interaction between the nearest neighbor pairs of atoms is small compared to the temperature which can be reached in the lab. Second, a scheme to induce a next-to-nearest neighbor coupling with a checkerboard pattern hasn't been conceived. We will leave these questions open and discuss only the quantum phases of this model

here.

4.2 Introduction

Understanding frustrated quantum magnetic models is a long standing difficult problem in strongly correlated physics. Theoretical tools to study these systems are limited. Exact diagonalization is limited by the small system size, and quantum Monte-Carlo simulation is hindered by the infamous sign problem. Among the frustrated models, the antiferromagnetic J_1-J_2 Heisenberg model on a checkerboard lattice (or called the crossed chain model) is an important example that has raised a lot of interest [91, 92, 93, 94, 95, 96, 97], due to its rich phase diagram and connection with real materials. This model is described by the Hamiltonian

$$H = J_1 \sum_{\langle i,j \rangle} \vec{S}_i \cdot \vec{S}_j + J_2 \sum_{\langle\langle i,j \rangle\rangle} \vec{S}_i \cdot \vec{S}_j \tag{4.1}$$

, where J_1 is the nearest-neighbor spin coupling rate on a square lattice and J_2 is the next-nearest-neighbor spin coupling rate on a checkerboard pattern of plaquettes, as depicted in Fig. 4.1. A number of works provide complimentary studies in different parameter regions. The complete phase diagram for this model, however, still remains controversial. It is known that the system has a collinear long-range Neel order when $J_2 << J_1$. At $J_1 \approx J_2$, the calculation based on the strong-coupling expansion predicts a plaquette valence bond solid as the ground state [95]. In the region with $J_2 > J_1 > 0$, the phase is still under debate. Possibilities include the fourfold degenerate state with long range spin order, supported with semi-classical studies [96] and large-N expansion calculation [97], the sliding Luttinger liquid phase, supported with perturbative random phase calculation and exact diagonalization of a small system [91], and the cross dimer state, supported with bosonization approach [93]

and two-step DMRG (density-matrix renormalization group) simulation [94].

Recently, tensor network algorithms emerge as a promising method to solve two-dimensional frustrated quantum systems [38, 44, 90, 98, 99]. There are different types of tensor network algorithms, but all the algorithms share the basic idea to describe the ground state of the model Hamiltonian as a tensor network state that respects the entanglement area law. The tensor network algorithms belong to the variational method and have no intrinsic sign problem for frustrated systems. The tensor network algorithms have been tested for a number of non-frustrated Hamiltonians, and the results agree pretty well with quantum Monte Carlo simulation [90]. Recently, the algorithms have also been applied to the frustrated Heisenberg model on a Kagome lattice [99] and the J_1-J_2-J_3 model on a square lattice [98].

In this chapter, we use the iPEPS(infinite PEPS) [38] tensor network algorithm, to simulate frustrated antiferromagnetic J_1-J_2 model on a a checkerboard lattice in the thermodynamic limit. We construct the complete phase diagram with the following findings: (1) the simulation shows two first-order phase transitions respectively at $J_2/J_1 = 0.88$ and $J_2/J_1 = 1.11$, first from a Neel state to a plaquette valence bond solid, and then to a spin ordered stripe phase. (2) In the region with $J_2/J_1 > 1.11$ (except for the special point $J_1 = 0$), our calculation supports the four-fold degenerate states proposed in Ref. [96] as the ground state. In particular, the spin stripe phase seems to be the most stable one under perturbation. (3) Our simulation provides strong evidence to show that the cross-dimer state is not the ground state of the system, although it indeed emerges as a metastable state in some parameter region (its energy is always significantly higher compared with the spin stripe phase).

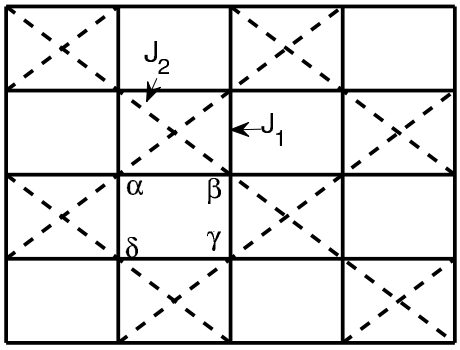

Figure 4.1: Illustration of the $J_1 - J_2$ Heisenberg model on a checkerboard lattice.

4.3 Implementation of the iPEPS Algorithm

4.3.1 Convergence test

In the iPEPS algorithm, at every site, we represent the state as a five-index tensor with one physical index (with dimension two for a spin-half system) and four virtual indices (with internal dimension denoted by D) [38]. The wave function can be obtained by contracting all the virtual indices. To obtain the expectation value of a physical quantity, we need to first contract the physical index to form a tensor network with internal dimension D^2, and this tensor network is then contracted from the infinite boundary through multiplication with a matrix product state with internal dimension χ. We tune the value of χ until convergence is achieved in the calculated physical quantity. As a thumb of rule, typically at $\chi \gtrsim D^2$, the relative error of energy induced by variation of χ has been reduced to the order of 10^{-5}, which indicates good convergence already. In Fig. 4.2(a) we show the ground state energy at $J_2/J_1 = 2$ as functions of χ for both $D = 4$ and $D = 5$. Indeed, the convergence in χ is ensured at our choice of χ values. The dominant error of the calculation is from the small value of the internal dimension D. As the calculation time scales with D as D^{12} (under choice of $\chi \sim D^2$) [38], the value of D in our simulation is limited to

be about 5. We compare the energy as well as several other quantities (including the phase boundary specified below in Fig. 4.3) calculated with $D = 4$ and $D = 5$, and the difference is within a percent level. In Fig. 4.2(b) the same quantity $\frac{\partial E}{\partial J_2}$ we used to characterize phase transitions is demonstrated from $D = 2$ to $D = 5$. Difference becomes very small beyond $D = 3$. As an estimate, we expect that the relative error of our numerical simulation, dominated by the limited value of D, is within or about a percent level for any short-range correlation function.

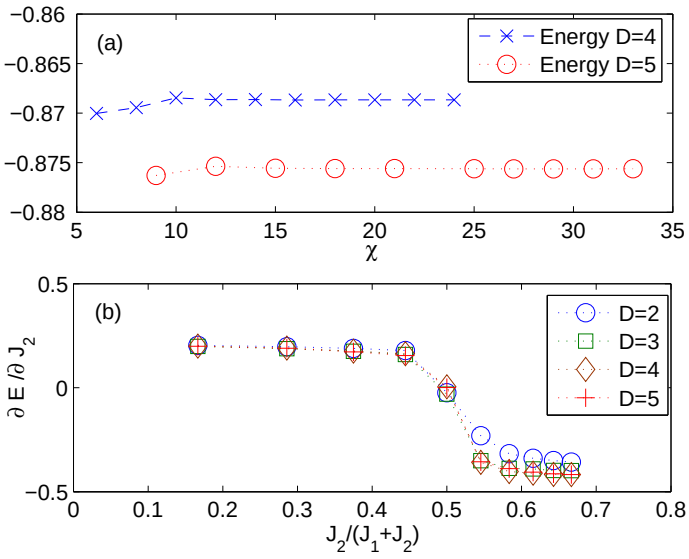

Figure 4.2: (a) Convergence of ground state energy at $J_2/J_1 = 2$ in χ for $D = 4$ and $D = 5$. (b) $\partial E/\partial J_2$ as functions of $J_2/(J_1 + J_2)$ for $D = 2, 3, 4$, and 5.

4.3.2 Translational symmetry breaking setup

The original iPEPS algorithm needs to assume translational symmetry for calculation in the thermodynamical limit. The ground state of the Hamiltonian 4.1 can spontaneously break the translational symmetry. To take into account the spontaneous symmetry breaking, we take a large unit cell and assume the translational symmetry only among different cells with no symmetry restriction for the tensors within the cell. In our simulation, the unit cell has 4×4 sites which is large enough

to incorporate the relevant ground states for this Hamiltonian that break the translational symmetry(A finite unit cell could suppress incommensurate spin orders, although such incommensurate orders do not sound to be a likely candidate for the ground state of the Hamiltonian 4.1). We apply imaginary time evolution to reach the ground state of the Hamiltonian. To avoid being stuck in a metastable state, we take a number of random initial states for the imaginary time evolution and pick up the ground state as the one which has the minimum energy over all the trials.

4.4 Phase Diagram

4.4.1 Plaquette order, magnetization, and derivative of Hamiltonian

In Fig. 4.3, we show the complete phase diagram for the Hamiltonian 4.1 from this calculation. To characterize the phase transition, we calculate derivative of the ground state energy $\frac{\partial E}{\partial J_2} = \sum_{\langle\langle i,j\rangle\rangle} \left\langle \vec{S}_i \cdot \vec{S}_j \right\rangle$ with respect to J_2 (J_1 is taken as the energy unit) and identify the singular point of this derivative as the phase transition point. To characterize properties of different phases, we calculate the spin order parameter $\left\langle \vec{S}_i \right\rangle$ for all sites i and the plaquette order parameter $Q_{\alpha\beta\gamma\delta}[100]$, defined by

$$\begin{aligned} Q_{\alpha\beta\gamma\delta} = 2 \Big[& \left\langle \vec{S}_\alpha \cdot \vec{S}_\beta \right\rangle \left\langle \vec{S}_\gamma \cdot \vec{S}_\delta \right\rangle + \left\langle \vec{S}_\alpha \cdot \vec{S}_\delta \right\rangle \left\langle \vec{S}_\beta \cdot \vec{S}_\gamma \right\rangle - \left\langle \vec{S}_\alpha \cdot \vec{S}_\gamma \right\rangle \left\langle \vec{S}_\beta \cdot \vec{S}_\delta \right\rangle \Big] \\ & + 1/2 [\left\langle \vec{S}_\alpha \cdot \vec{S}_\beta \right\rangle + \left\langle \vec{S}_\gamma \cdot \vec{S}_\delta \right\rangle + \left\langle \vec{S}_\alpha \cdot \vec{S}_\delta \right\rangle + \left\langle \vec{S}_\beta \cdot \vec{S}_\gamma \right\rangle \left\langle \vec{S}_\alpha \cdot \vec{S}_\gamma \right\rangle \\ & + \left\langle \vec{S}_\beta \cdot \vec{S}_\delta \right\rangle + 1/4] \end{aligned} \tag{4.2}$$

, where α, β, γ, and δ denote four spins on a plaquette as shown in Fig. 4.1. Different phases are associated with different characteristic values of these parameters. For instance, a spin ordered state is characterized by a significant value of $\left\langle \vec{S}_i \right\rangle$;

in contrast, the plaquette valence bond solid state is characterized by a near-unity $Q_{\alpha\beta\gamma\delta}$ and a vanishing $\left\langle \vec{S}_i \right\rangle$.

In the insets of Fig. 4.3, we show the order parameters $\left\langle \vec{S}_i \right\rangle$ and $Q_{\alpha\beta\gamma\delta}$ as functions of J_2/J_1. These order parameters change abruptly at the corresponding phase transition points, and the points of abrupt change are in agreement with the singularity points of $\frac{\partial E}{\partial J_2}$. The order parameters and the derivative of the ground state energy both have finite jumps at the phase transition points, which strongly indicates that we have two first-order transitions as we increase the ratio J_2/J_1, first from a Neel ordered state to a plaquette valence bond solid state at $J_2/J_1 = 0.88$, and then from the valence bond solid state to another spin-ordered phase (its nature will be discussed below) at $J_2/J_1 = 1.11$. The possibility of two second order phase transitions with a coexistence region of the spin and the valence bond solid orders in the intermediate region has been discussed in the literature [101]. Within the resolution of our numerical simulation (the resolution is 0.01 for the ratio J_2/J_1 near the phase transition points), we do not find a coexistence region and the result supports a direct first-order transition.

4.4.2 Patterns of local spin-spin correlations

The nature of ground states in these three phases are further studied through calculation of the spin correlation function. In Fig. 4.4, We show the nearest-neighbor spin-spin correlation $\left\langle \vec{S}_i \cdot \vec{S}_j \right\rangle$ and orientation of local spins with respect to the first spin on the up-left corner in each 16-site unit-cell for three different J_2 values. At $J_2 = 1$, strong nearest-neighbor spin correlations (valence bonds) around the plaquettes breaking the lattice translational symmetry suggests a plaquette ordered state near this point, consistent with the finding in Fig. 4.3. At $J_2 = 0.5$, the spin

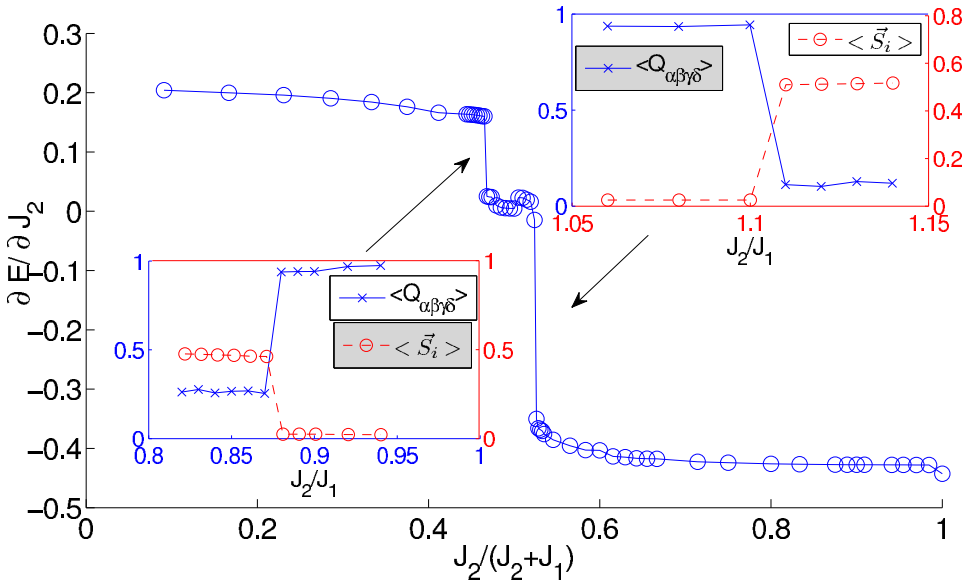

Figure 4.3: The main plot shows $\partial E/\partial J_2$ as a function of $J_2/(J_1+J_2)$. Insets show the plaquette order (solid line with crosses) and the spin order (red dashed line with circles) as functions of J_2/J_1near the transition points.

orientation indicates a conventional Neel ordered state. At $J_2 = 2$, antiferromagnetic Neel order appears along the diagonal chains, but not in the horizontal or vertical axes. With imaginary time evolution starting from randomly chosen initial states, we actually get two different kinds of spin configurations shown in Fig. 4.4(c) and 4.4(d) for the final state. Their energies are almost degenerate within resolution of our numerical program. These spin configurations are in agreement with the four-fold degenerate states found in Ref. [96] based on the large-S expansion (the other two degenerate states are obtained from Fig. 4.4(c) and 4.4(d) through a 90-degree rotation of the spin orientation). The spin configuration in Fig. 4.4(c) is called the Neel*-state in Ref. [93], where the single-site spin $\uparrow$ or $\downarrow$ in the conventional Neel state is replaced by the two-site unit $\uparrow\uparrow$ or $\downarrow\downarrow$. The configuration in Fig. 4.4(d) represents a spin stripe phase, where the spin orientations form a stripe along the horizontal or vertical direction, breaking the lattice rotational symmetry. The stripe phase is also predicted in the large-N calculation [97].

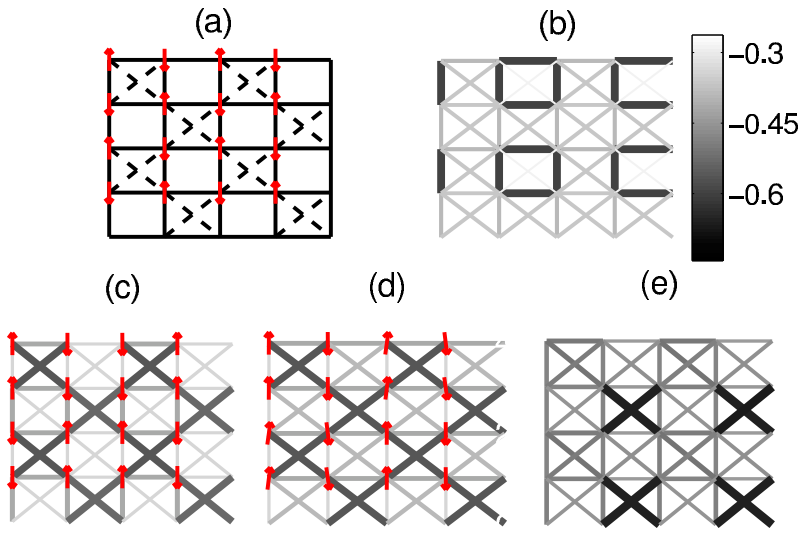

Figure 4.4: The upper left figure (a) shows orientations of local spins (red arrows) on the checkerboard lattice at $J_2 = 0.5$. The upper right figure (b) shows nearest neighbor spin-spin correlations $< \vec{S}_i \cdot \vec{S}_j >$ along horizontal, vertical and diagonal bonds on a 16-site unit-cell at $J_2 = 1.0$. The width and colors of the bonds are scaled such that the negative correlation is represented by thicker bonds with darker color. The lower figures show both spin orientation and correlations $< \vec{S}_i \cdot \vec{S}_j >$ in a Neel* state (c) and a stripe phase (d) at $J_2 = 2$. (e) illustrates the dimer state, which appears as a metastable state at some parameters.

4.4.3 Metastable dimer states at large J_2

To further clarify the phase at $J_2 = 2$, we also show the spin-spin correlation $\left\langle \vec{S}_i \cdot \vec{S}_j \right\rangle$ in Fig. 4.4(c) and 4.4(d). Strong nearest-neighbor spin correlation appears along the diagonal chains. However, the distribution of these spin correlations does not break the symmetry of the lattice, so it is not a cross dimer or other valence bond solid state. The cross dimer state is predicted for this model in [93, 94] for some region of J_2/J_1. In a cross dimer state, the nearest-neighbor spin correlations form the cross dimer pattern illustrated by Fig. 4.4(e). We indeed get this kind of cross dimer configuration from the imaginary time evolution starting from a pure cross dimer state for a certain region of J_2/J_1 as shown in Fig. 4.5. However, the energies of the cross dimer states are strictly higher than the four-fold degenerate

states shown in Fig. 4.4(c) and 4.4(d). So the cross dimer state is only a metastable phase in this region and does not give the real ground state. We compare the energy of our calculation with the energy of the DMRG calculation in Ref. [94], and our energy is significantly lower than the corresponding result in [94] on the side $J_2 > J_1$. For instance, at $J_2 = 2$, our result shows a ground state energy of $E = -0.876J_1$ for a stripe state, much lower than the energy of $E \simeq -0.75J_1$ for a cross dimer state at the corresponding point in Ref. [94]. Because of this large energy difference, it is unlikely that the cross dimer state emerges as the real ground state of the system.

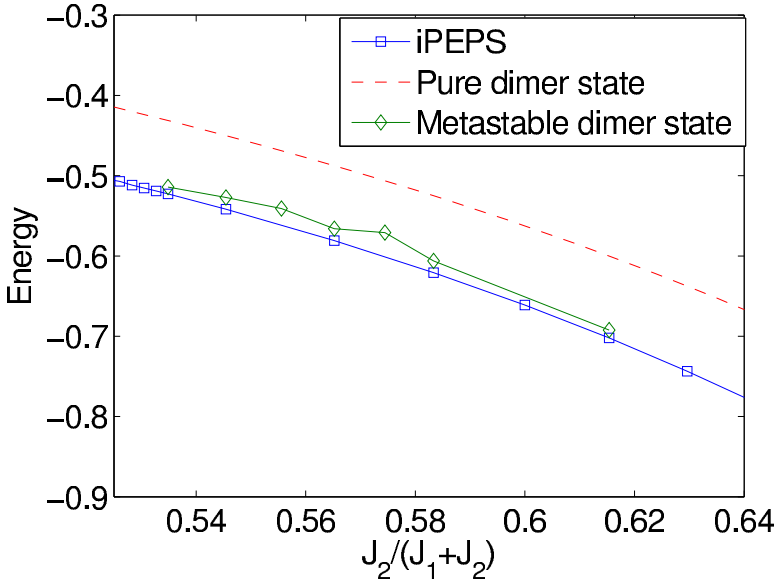

Figure 4.5: Ground state energy calculated by iPEPS (blue squares) for different $J_2/(J_2 + J_1)$. The dashed line denotes energy of a pure dimer state, the green diamonds denote energy of meta-stable dimer states calculated by iPEPS with imaginary time evolution from an initial pure dimer state.

4.4.4 Discussion on states at large J_2

Some literature predicts a sliding Luttinger liquid state on the $J_2 > J_1$ side of the antiferromagnetic checkerboard model [91, 92]. We do not find evidence to support a transition to a sliding Luttinger liquid state in our numerical simulation. Of course, due to the limitation of the internal dimension D of the variational tensor network

state in our calculation, it is possible that the sliding Luttinger liquid state is poorly approximated by the tensor network state with a small internal dimension and thus missed in our numerical simulation. We can not rule out this possibility, however, we feel its chance is small due to the following test: we know at the limiting point $J_1 = 0$, the model reduces to decoupled Heisenberg chains whose ground state is described by a Luttinger liquid with algebraic decay of the spin correlation function. We use the same tensor network algorithm to calculate the long range spin correlation for the limiting case at $J_1 = 0$. At this 1D limiting point, we can have a much larger internal dimension D in numerical simulation, and in Fig. 4.6(a) we compare the result with D varying from 2 to 30. We see that result at $D = 5$ has qualitatively shown the correct algebraic decay of the spin correlation function and the $D = 15$ result almost converged to the result at $D = 30$. The improvement with larger internal dimension does not change the qualitative behavior. So we do not necessarily need a large internal dimension for the tensor network algorithm to uncover the algebraic decay associated with a spin liquid state although it indeed gives a better estimate of the power law exponent. Keeping the same internal dimension at $D = 5$, we turn on J_1 (now a 2D model with $J_2 > J_1 > 0$) and find that the spin correlation $\langle \vec{S}_i \vec{S}_{i+d} \rangle$ points to a long range order with a non-varnishing mean value $\langle \vec{S}_i \rangle$ (the imaginary time evolution in the tensor network algorithms typically leads to a symmetry spontaneously broken state when there is a long range order). When we subtract the mean value and draw the spin correlation $\langle \vec{S}_i \vec{S}_{i+d} \rangle - \langle \vec{S}_i \rangle \langle \vec{S}_{i+d} \rangle$, the subtracted spin correlation can be well fit with an exponentially decaying function (see Fig. 6(b)), which is consistent with a long ranged ordered state and does not support a spin liquid state with algebraic decay along the diagonal chain.

Although our numerical program can not distinguish the energy of the four de-

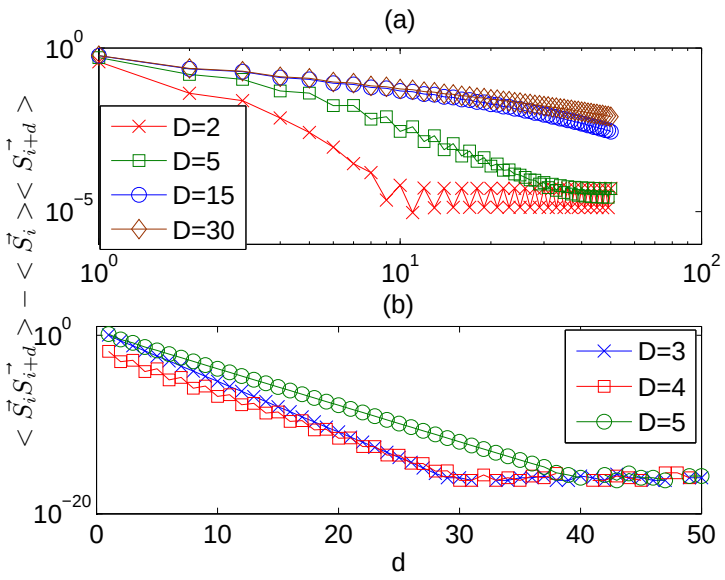

Figure 4.6: (a) Long-range spin correlations for a antiferromagnetic Heisenberg chain obtained with $D = 2$ (crosses), $D = 5$ (squares), $D = 15$ (circles), and $D = 30$ (diamonds) in log-log plot. (b) The same correlation along a diagonal chain for 2D checkerboard lattice calculated with $D = 3$ (crosses), $D = 4$ (squares), and $D = 5$ (circles) at $J_2 = 2$ in semi-log plot.

generate states shown in Fig. 4.4(c,d) at the $J_2 > J_1$ side, it is very likely that the stripe phase will emerge as the real ground state in practice because of its robustness to perturbation in the Hamiltonian. In real realization of the model Hamiltonian 4.1, the J_1 coupling along the horizontal and the vertical directions might be slightly different, or apart from the J_2 coupling on the checkerboard pattern, there might be small antiferromagnetic J_2 coupling along the other plaquettes. With any of these types of perturbation (which sound to be inevitable in practice), the energy of the Neel*-state will be lifted, and the stripe phase will emerge as the unique ground state of the system.

4.5 Chapter Summery

We have used the iPEPS method, a type of tensor networks algorithms, to calculate the ground states of the frustrated anti-ferromagnetic J_1-J_2 Heisenberg model

on a checkerboard lattice. We construct the complete phase diagrams, indicting two first order phase transitions, first from a Neel state to a plaquette valence bond solid and then to a spin stripe phase. The calculation helps to clarify some of the previous debates on the phase diagram of this important model and provides a novel example for applications of the recently developed tensor network algorithms to frustrated systems.

CHAPTER V

Evidence of spin liquid with hard-core bosons in a square lattice

5.1 Overview

We show that laser assisted hopping of hard core bosons in a square optical lattice can be described by an antiferromagnetic $J_1 - J_2$ XY model with tunable ratio of J_2/J_1. We numerically investigate the phase diagram of the $J_1 - J_2$ XY model using both the tensor network algorithm for infinite systems and the exact diagonalization for small clusters and find strong evidence that in the intermediate region around $J_2/J_1 \sim 0.5$, there is a spin liquid phase with vanishing magnetization and valence bond orders, which interconnects the Neel state on the $J_2 \ll J_1$ side and the stripe antiferromagnetic phase on the $J_2 \gg J_1$ side. This finding opens up the possibility of studying the exotic spin liquid phase in a realistic experimental system using ultracold atoms in an optical lattice.

5.2 Introduction

A spin liquid phase is an exotic state of matter that does not break any symmetry of the Hamiltonian and has no conventional order even at zero temperature [31]. A number of microscopic Hamiltonians with frustrated quantum magnetic interaction

could support a spin liquid phase [31, 102, 103, 104, 105, 106, 107]. In particular, very recently, numerical investigations based on complementary methods have found strong evidence that the antiferromagnetic J_1-J_2 Heisenberg model may have a spin liquid phase in a square lattice [104, 105, 106]. On the experimental side, several materials are suspected to be in a spin liquid phase at very low temperature [31]. However, due to complication of physics in these materials, it is hard to make a direct connection of the prediction from the simplified microscopic models and the phenomenology observed in real materials [31]. Ultracold atoms in an optical lattice provides a clean platform to realize microscopic models to allow for controlled comparison between theory and experiments [108, 19]. Proposals have been made to implement the frustrated magnetic models in an optical lattice [109] and various required configurations of the optical lattices have been realized experimentally [110, 8]. However, the direct magnetic Heisenberg coupling, which comes from the higher-order super-exchange interaction, is very weak under typical experimental conditions [109, 111]. It is still very challenging to reach the extremely low temperature required to observe the ground state of the magnetic Heisenberg model in an optical lattice.

In this chapter, we show strong evidence that a spin liquid phase can emerge in an antiferromagnetic J_1-J_2 XY model in a square lattice. The calculations are based on two complementary methods: the recently developed tensor network algorithm applied directly to infinite systems [44, 112, 113] and the exact diagonalization of small clusters which is combined with the finite size scaling to infer the phase diagram [114, 115]. Both methods suggest that in a small region around $J_2/J_1 \approx 0.5$, magnetization and valence bond solid orders all vanish, indicating a spin liquid phase as the ground state. Different from a Heisenberg model, a XY model can be realized with

hard-core bosons in an optical lattice with local boson occupancy as pseudo-spins. Through control of the laser assisted hopping in a square lattice [23, 24, 116, 10], we propose a scheme to implement the effective antiferromagnetic couplings for both the neighboring and the next neighboring sites with a tunable ratio of J_2/J_1. In this implementation, both J_2 and J_1 are determined by the hopping rates of the hard-core bosons in an optical lattice, which are much larger than the conventional super-exchange interaction for ultracold atoms in the Heisenberg model [109, 111]. The large J_1-J_2 couplings open up the possibility to experimentally realize this model and observe its spin liquid phase based on the state-of-the-art technology.

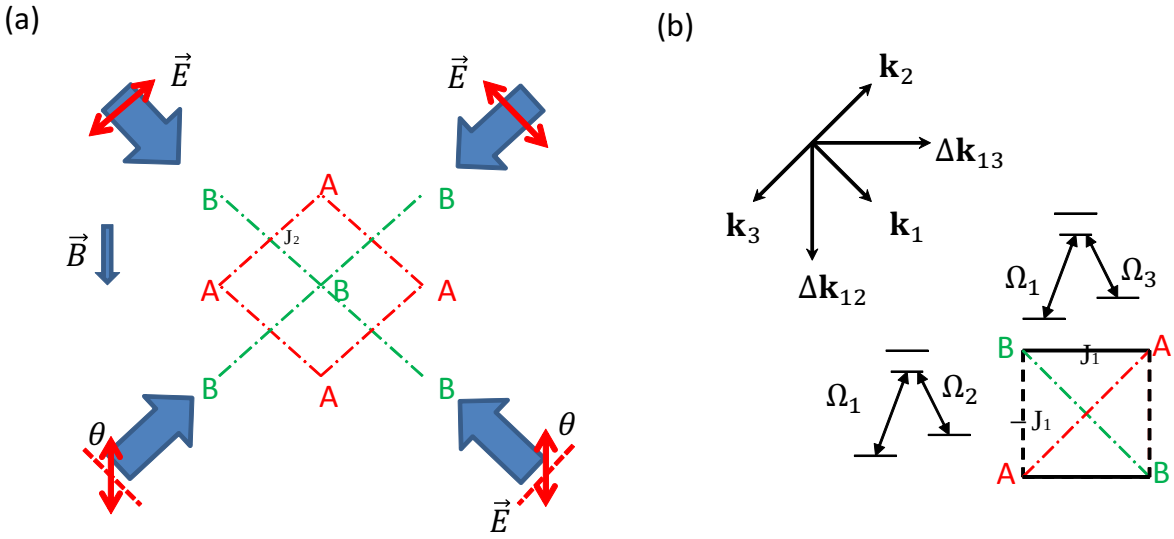

Figure 5.1: (a) Implementation of the $J_1 - J_2$ XY model with cold bosons in a bipartite spin-dependent optical lattice, where the J_2 coupling is due to the atomic hopping in the same sub-lattice. We choose $\vec{B} = (0, -1, 0), \vec{E} = \frac{1}{\sqrt{2}}(1, 1, 0), \frac{1}{\sqrt{2}}(1, -1, 0)$ and $(0, 0, 1)$ with $\theta = \pi/2$ (b) The configuration of the wave-vectors for the three Raman laser beams. The J_1 coupling(shown as solid lines and dashed lines) is induced by the three Raman laser beams (the direct J_1 hopping of the atoms is turned off by the large potential shift between the two sub-lattices).

5.3 Implementation of J_1-J_2 XY model

The J_1-J_2 XY model is represented by the Hamiltonian

$$H = J_1 \sum_{\langle i,j \rangle} (X_i X_j + Y_i Y_j) + J_2 \sum_{\langle\langle i,j \rangle\rangle} (X_i X_j + Y_i Y_j), \tag{5.1}$$

where X, Y represent the Pauli operators σ_x and σ_y, $\langle i,j \rangle$ and $\langle\langle i,j \rangle\rangle$ denote respectively the neighboring and the next neighboring sites in a square lattice as shown in Fig. 5.1(b). To realize this model with hard core bosons, we consider ultracold atoms in different hyperfine spins $|a\rangle$ and $|b\rangle$ loaded into alternating square lattices A and B as shown in Fig. 5.1(a). This configuration can be experimentally realized with the spin-dependent lattice potential [117]. Atoms in spins $|a\rangle$ (or $|b\rangle$) freely tunnel in the lattice A (or B) with the hopping rate t, however, a direct hopping between the A, B lattices is forbidden due to the spin-dependent potential shift. Instead, the inter-lattice hopping is introduced by the laser induced Raman transition as shown in Fig. 5.1(a). We use three Raman beams, with wave-vectors $\mathbf{k}_1$, $\mathbf{k}_2$, and $\mathbf{k}_3$ and Rabi frequencies $\mathbf{\Omega}_1$, $\mathbf{\Omega}_2$, and $\mathbf{\Omega}_3$, respectively. The directions of the laser beams are shown in Fig. 5.1(b) with $\Delta\mathbf{k}_{12} = \mathbf{k}_1 - \mathbf{k}_2 = k_\Delta \hat{y}$ and $\Delta\mathbf{k}_{13} = \mathbf{k}_1 - \mathbf{k}_3 = k_\Delta \hat{x}$. The laser induced inter-lattice hopping rates for the neighboring sites are then given by

$$t_x = \int w^* (x_i, y_i) \frac{\mathbf{\Omega}_1^* \mathbf{\Omega}_3}{\delta} e^{ik_\Delta x} w (x_{i+1}, y_i) \, dxdy, \tag{5.2}$$

and

$$t_y = \int w^* (x_i, y_i) \frac{\mathbf{\Omega}_1^* \mathbf{\Omega}_2}{\delta} e^{ik_\Delta y} w (x_i, y_{i+1}) \, dxdy, \tag{5.3}$$

for the hopping along the x, y directions respectively, where δ is the detuning. Assume $\mathbf{\Omega}_3 = -\mathbf{\Omega}_2$ and the Wannier function $w(x_i, y_i)$ symmetric along the x, y directions, we have $t_x = -t_y = t'$ (we can always choose $t' > 0$ by setting an

appropriate relative phase between $\mathbf{\Omega}_1$ and $\mathbf{\Omega}_3$). If the on-site atomic repulsion U satisfies $U \gg t, t'$, we have the hard-core constraint with at most one boson per site. The hard-core bosons in this square lattice are then described by the Hamiltonian

$$H = t' \sum_{\langle i,j \rangle_x} a_i^\dagger b_j - t' \sum_{\langle i,j \rangle_y} a_i^\dagger b_j - t \sum_{\langle\langle i,j \rangle\rangle} (a_i^\dagger a_j + b_i^\dagger b_j) + H.c. \tag{5.4}$$

Bosonic operators a_i, b_j satisfy the same commutators as the Pauli operators σ_i^-, σ_j^-, so with the mapping $a_i \longrightarrow \sigma_i^-$ and $b_j \longrightarrow \sigma_j^-$ for the odd numbers of rows, and $a_i \longrightarrow -\sigma_i^-$ and $b_j \longrightarrow -\sigma_j^-$ for the even numbers of rows, the Hamiltonian 5.4 is mapped to the J_1-J_2 XY model in Eq. 5.1 with $J_1 = t'/2 > 0$ and $J_2 = t/2 > 0$. Apparently, the ratio J_2/J_1 is tunable by changing the magnitude of the Rabi frequencies $\mathbf{\Omega}_1^* \mathbf{\Omega}_3$.

5.4 Numerical Simulation

In the following, we calculate the phase diagram of the Hamiltonian 5.1 as a function of the dimensionless parameter J_2/J_1 (J_1 is taken as the energy unit). We limit our discussion to a half-filling case. In the limit $J_2/J_1 \ll 1$, the J_1 term dominates and the ground state is magnetized with a Neel order at the momentum $k = (\pi, \pi)$. In the opposite limit $J_2/J_1 \gg 1$, the ground state has a stripe magnetic order at the momentum $(\pi, 0)$ or $(0, \pi)$, which minimizes the energy of the J_2 term. In the intermediate region with $J_2/J_1 \sim 0.5$, the Hamiltonian is highly frustrated with competing interaction terms. Our main purpose is to find out the phase diagram in this region through controlled numerical simulations.

Our numerical simulations are based on two complimentary methods: exact diagonalization (ED) for small clusters [114, 115] and tensor network simulation for infinite systems [112, 44, 113]. The ED method is limited by the cluster size, and we

use extrapolation based on the finite-size scaling to infer the phase diagram for the infinite system. The tensor network algorithm is an recently developed simulation method inspired by quantum information theory [112, 44]. It can be considered as an extension of the density matrix renormalization group (DMRG) method to the two dimensional case, replacing the matrix product state in the DMRG method with the tensor network state that better matches the geometry of the underlying lattice [112]. We use a particular version of the tensor network algorithms, the infinite projected entangled pair states (iPEPS) method [44], which applies directly to infinite systems using the translational symmetry. To take into account the ordered states for the Hamiltonian 5.1 that spontaneously break the translational symmetry, in our simulation we take a unit cell (typically 2×2 and 4×4) that is large enough to incorporate the relevant symmetry breaking orders [49]. We apply imaginary time evolution to reach the ground state of the Hamiltonian. To avoid being stuck in a metastable state, we take a number of random initial states for the imaginary time evolution and choose the ground state as the one which has the minimum energy over all the trials. The accuracy of the iPEPS simulation depends on the internal dimension D of the tensor network state. The simulation time scales up very rapidly with the dimension D, which limits D to a small value in practice. We typically take D between 4 to 6 in our simulation.

5.4.1 Local measurement from iPEPS method

Figure 5.2 shows the major result from the iPEPS simulation. First, we look at the average magnetization $m_s = (1/N_s)\sum_i \sqrt{X_i^2 + Y_i^2 + Z_i^2}$ as a function of J_2/J_1, where the average is taken over the N_s sites in the unit cell. The calculation shows that for small or large J_2/J_1, the ground states are magnetic (with the Neel

or the stripe order, respectively), which is consistent with our intuitive picture. In the intermediate region with $0.46 \leq J_2/J_1 \leq 0.54$, there is a sudden drop of all the magnetic orders to a tiny value. Although the iPEPS method under a small dimension D could be biased toward a less entangled state, which is typically an ordered state, it would not be biased toward a disordered spin liquid state. So, when we see a big sudden drop of the magnetic orders from the simulation, it must be a real effect, strongly indicating there is a new phase in the intermediate region with vanishing magnetic orders. The remaining small m_s may be due to the finite dimension D and should vanish when D is scaled up.

To figure out the property of the phase in the intermediate region, we further check different kinds of valence bond solid orders. We calculate all the neighboring valence bonds $\langle \sigma_i \cdot \sigma_j \rangle$ in the unit cell and the result is shown in Fig. 5.2. For a valence bond solid state, the spatial symmetry should be spontaneously broken for the valence-bond distribution. Figure 5.2 shows that in the entire region of J_2/J_1, the valence bond distribution has the same symmetry as the underlying Hamiltonian, which indicates that the ground state of the Hamiltonian 5.1 has no valence bond solid orders. Together with the above calculation of the magnetic orders, this suggests that the Hamiltonian 5.1 has a spin liquid phase with no orders in the intermediate region with $0.46 \leq J_2/J_1 \leq 0.54$. This spin liquid phase seems to have the same feature as the $Z2$ spin liquid in the intermediate coupling region of the J_1-J_2 Heisenberg model found in the recent numerical simulation [104, 105, 106].

5.4.2 Long-range spin-spin and dimer correlations from iPEPS

To further confirm this picture, we calculate the long-range spin correlation and dimer correlation with the iPEPS method and the result is shown in Fig. 5.3 for

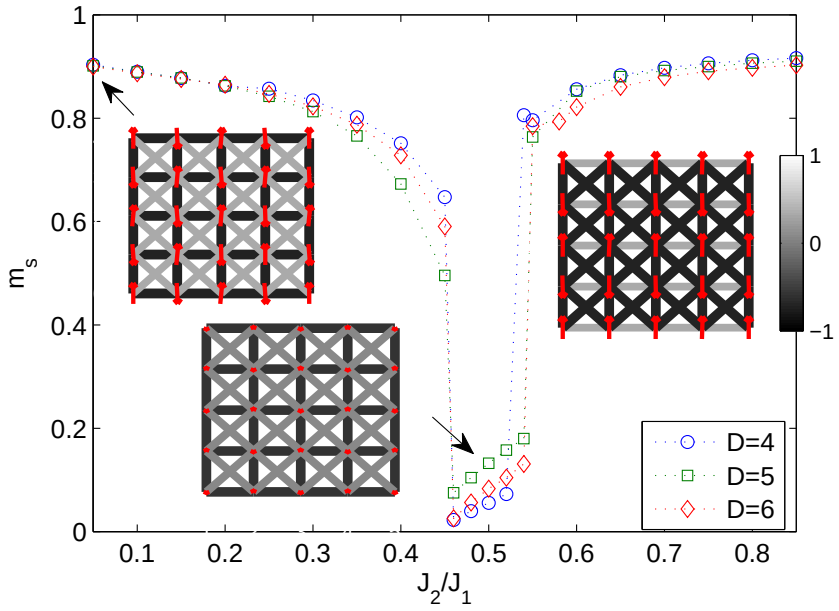

Figure 5.2: Average magnetization m_s as a function of J_2/J_1. The insets show the spin configuration and the valence bond distribution $\langle \sigma_i \cdot \sigma_j \rangle$ at $J_2/J_1 = 0$, 0.5, and 0.9 obtained with the iPEPS on a 4×4 unit cell with $D = 6$. The width and color of the bonds are scaled such that the negative energy is shown by thicker bond with darker color and the positive energy is shown by thinner bond with lighter color and the length of the spin is proportional to its magnetic moment m_s.

$J_2/J_1 = 0.1, 0.5$ and 0.9. The spin correlation $\langle \sigma_i \cdot \sigma_j \rangle$ is calculated along the diagonal direction $\hat{x} + \hat{y}$. Both the Néel and the stripe phases have long-range correlations, with constant or staggered values along the diagonal direction. The intermediate phase has an exponentially decaying spin-spin correlation, which is in agreement with the behavior of the $Z2$ spin liquid phase with a finite spin gap [31, 104, 105, 106]. The dimer operator D_i^α is defined by $D_i^\alpha = \sigma_i \cdot \sigma_{i+\alpha}$ for the bond $(i, i+\alpha)$, where $\alpha = \hat{x}$ or $\hat{y}$ denote the orientation of the dimer. In Fig. 5.3(c), we show the dimer-dimer correlations $\langle \Delta D_i^x \Delta D_j^x \rangle$ and $\langle \Delta D_i^y \Delta D_j^y \rangle$ at $J_2/J_1 = 0.5$ along the diagonal direction, where $\Delta D_i \equiv D_i - \langle D_i \rangle$. The correlations are exponentially decaying with distance, in agreement with a spin liquid phase with no dimer orders.

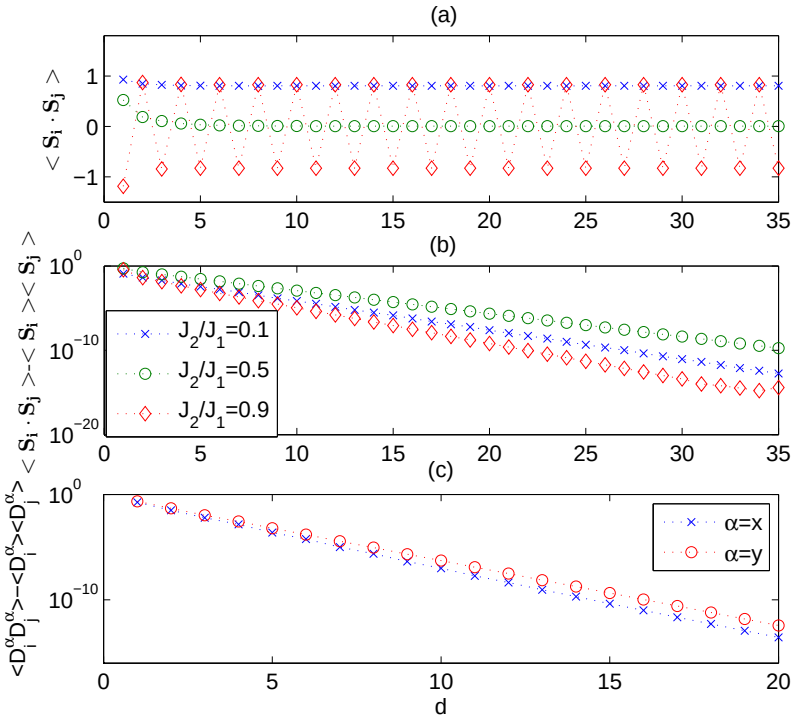

Figure 5.3: (a) Spin-spin correlation $\langle \sigma_i \cdot \sigma_j \rangle$ as a function of distance d along the diagonal direction at $J_2/J_1 = 0.1$ (cross), 0.5 (circle) and 0.9 (open diamond). (b) Semi-log plot of spin-spin correlation $\langle \Delta\sigma_i \cdot \Delta\sigma_j \rangle$ after subtracting the local averages. (c) Semi-log plot of dimer-dimer correlation $\langle \Delta D_i^\alpha \Delta D_j^\alpha \rangle$ ($\alpha = x, y$) as a function of distance d along the diagonal direction at $J_2/J_1 = 0.5$.

5.4.3 Structure factors from exact diagonalization methods

In the following, we present study of the Hamiltonian 5.1 with the complementary ED method, which provides further evidence for a spin liquid phase in the intermediate region. To be consistent with the periodic boundary condition required for the finite size scaling and to incorporate the momentum $k = (\pi, \pi)$ responsible for the Neel order, the size of the clusters for the ED is taken to 16, 20 and 32 sites. From the spin correlation $\langle \sigma_i \cdot \sigma_j \rangle$, we calculate the corresponding static structure factor $m_s^2(\mathbf{k}, N) = (1/N) \sum_{ij} e^{i\mathbf{k}\cdot(\mathbf{r}_i - \mathbf{r}_j)} \langle \Delta\sigma_i \cdot \Delta\sigma_j \rangle$, where N is the size of the cluster and $\Delta\sigma_i \equiv \sigma_i - \langle \sigma_i \rangle$. The Neel order and the stripe order correspond to peaks at $\mathbf{k} = (\pi, \pi)$ and $(\pi, 0)$, respectively. Finite-size clusters always have non-zero order

parameters, and one needs to do finite size scaling, with a simple scaling formula $m_s^2(\mathbf{k}, N) = m_s^2(\mathbf{k}, \infty) + a/\sqrt{N}$ ($\sqrt{N}$ corresponds to the linear size), to infer the value of $m_s^2(\mathbf{k}, \infty)$ for the infinite system. In Fig. 5.4, we show the finite size scaling for $m_s^2(\mathbf{k}, N)$ at $J_2/J_1 = 0, 0.5$, and 0.9 in three different regions. The results are consistent with the findings from iPEPS method, i.e., there is a stripe order with $\mathbf{k} = (\pi, 0)$ at $J_2/J_1 = 0.9$ and a Neel order with $\mathbf{k} = (\pi, \pi)$ at $J_2/J_1 = 0$. At $J_2/J_1 = 0.5$, the finite-size scaling indicates a vanishing stripe order. However, at $\mathbf{k} = (\pi, \pi)$, the data become non-monotonic with N due to the shape of the cluster and the finite-size scaling becomes inconclusive in this case. The non-monotonic shape effect has also been observed in ED for the J_1-J_2 Heisenberg model [114, 115].

To check for possible valence bond solid orders from ED, we similarly calculate the structure factors $m_d^2(\mathbf{k}, N) = (1/N)\sum_{ij} e^{i\mathbf{k}\cdot(\mathbf{r}_i - \mathbf{r}_j)}\langle \Delta D_i^x \Delta D_j^x \rangle$ and $m_p^2(\mathbf{k}, N) = (1/N)\sum_{ij} e^{i\mathbf{k}\cdot(\mathbf{r}_i - \mathbf{r}_j)}(\langle P_i P_j \rangle$, corresponding respectively to the dimer order D_i^x and the plaquette order $P_i = (Q_i + Q_i^{-1})/2$, where Q_i (Q_i^{-1}) is the clockwise (counter-clockwise) cyclic permutation operator on the plaquette i with its explicit (lengthy) expression given in [100, 49]. The rotational symmetry is always preserved at finite size, so we only need to check one component of the dimer order, say D_i^x. At finite size, the structure factors peak at $\mathbf{k} = (\pi, 0)$ for the dimer order D_i^x and at $\mathbf{k} = (\pi, \pi)$ for the plaquette order P_i, however, an extrapolation to the infinite system at these momenta as shown in Fig. 5.5 indicates vanishing dimer and plaquette orders in all three regions of J_2/J_1. This result, again, is in agreement with the finding from the iPEPS calculation.

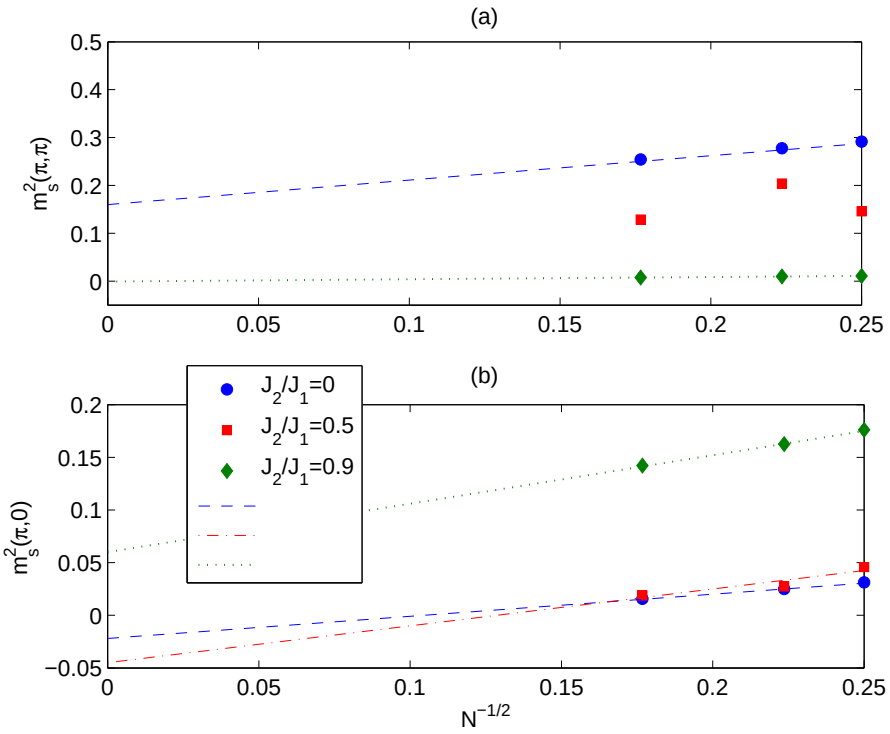

Figure 5.4: Finite size scaling of the magnetic order parameter at (a) $\mathbf{k} = (\pi, \pi)$ and (b) $\mathbf{k} = (\pi, 0)$ at $J_2/J_1 = 0$ (dot), 0.5 (square), and 0.9 (diamond).

5.5 Connect to Experiments

5.5.1 Experimental signature of different phases

Before concluding this chapter, we briefly discuss the experimental signature of the three different phases for the Hamiltonian 5.1 in the implementation with hard-core bosons. The Neel ordered state and the stripe phase correspond to Bose-Einstein condensates at the momenta $\mathbf{k} = (\pi, \pi)$ and $\mathbf{k} = (\pi, 0)$, respectively. The standard time-of-flight imaging measurement can then reveal the condensate peak at these nontrivial momentum points [19]. The spin liquid phase, on the other hand, would not show any condensation peaks due to a lack of magnetic orders. Furthermore, the exponentially decaying spin-spin correlation ensures a spin gap[104, 105, 106] which implies a charge gap in implementation with hard-core bosons. We therefore

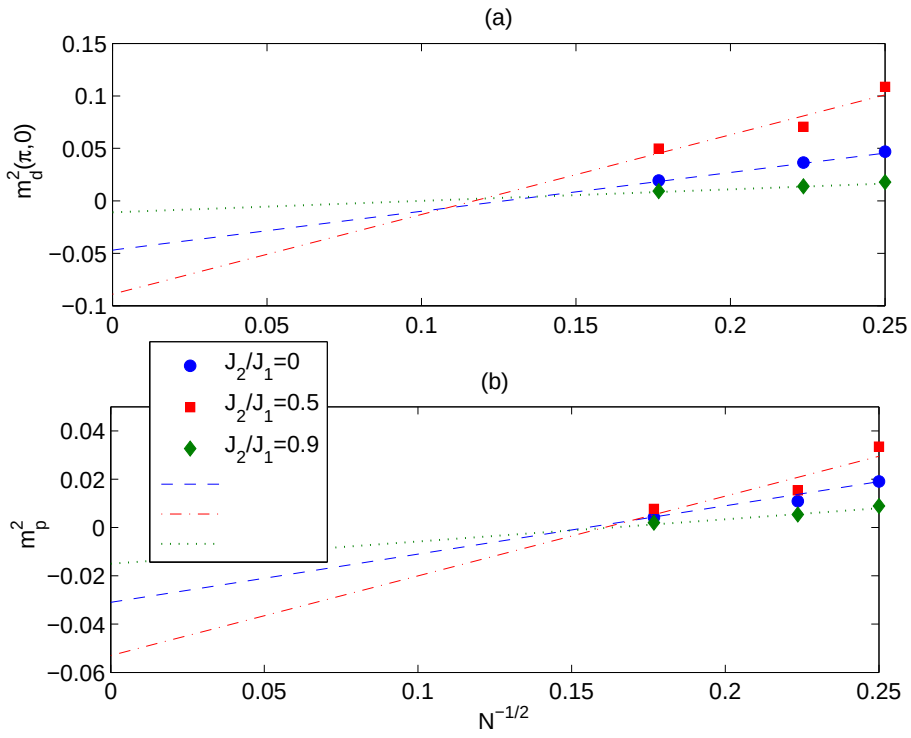

Figure 5.5: Finite size scaling of (a) the dimer order parameter at $\mathbf{k} = (\pi, 0)$ and (b) the plaquette order parameter at $\mathbf{k} = (\pi, \pi)$ at $J_2/J_1 = 0$ (dot), 0.5 (square), and 0.9 (diamond).

expect to see an incompressible phase at half filling, which is different from the Mott insulator state at the integer filling.

5.5.2 Harmonic trap and finite temperature

In a realistic experimental setup with a harmonic trapping potential we could estimate the radius of a half-filling region given by $R_{hf} = \sqrt{(2\mu(0) - \Delta_T)/M\omega^2}$. The triplet spin gap Δ_T is roughly equal to the energy needed to break a singlet pair, which in our system is about J_2. We choose ^{23}Na atoms in the optical lattice with $\lambda = 594.71$ nm and $E_R = 24.4$ khz[118]. Assuming a lattice depth $V_0 = 10$ E_R and a moderate Rabi frequency $\mathbf{\Omega}_1\mathbf{\Omega}_2/\delta = 0.2$ E_R we find the tunneling energy $J_2 \sim 500$ hz and laser-induced tunneling $J_1 \sim J_2$. For ^{87}Rb with $\lambda = 767$ nm one could get $J_2 \sim 75$ hz. Considering a trap($\omega = 2\pi \times 110$ Hz) for ^{23}Na we get

$R_{hf} \sim 20$ lattice constant and for ^{87}Rb a trap ($\omega = 2\pi \times 10$ Hz) roughly gives us $R_{hf} \sim 30$ lattice constant. The temperature required to observe this phase is at the same order of J_2 which as estimated before are about 200 nK for ^{23}Na and 25 nK for ^{87}Rb. Compared with the characteristic super-exchange interaction energy scale J^2/U, where U is the on-site interaction energy, the temperature required is (U/J) times higher. It is also be distinguished from a charge density wave state since the density distribution in this case is still homogeneous without any solid order.

5.6 Chapter Summary

We have proposed an experimentally feasible scheme to implement the J_1-J_2 XY model with ultracold hard-core bosons in a square optical lattice. Through detailed numerical simulation of this model using two complementary methods, we find strong evidence that this model has a spin liquid phase in the intermediate region of J_2/J_1. The proposed experimental implementation, with tunable ratio of J_2/J_1, opens up a realistic possibility to look for the long-pursued spin liquid phase in a well controlled Hamiltonian model.

CHAPTER VI

Quantum magnetism of quarter filled ultracold $F = \frac{3}{2}$ fermions on a square lattice

6.1 Overview

We use infinite projected entangled-pair states(iPEPS) algorithm to study the phase diagram of quarter filling $F = \frac{3}{2}$ fermions on the square lattice in the strong interaction regime, which are characterized by a Heisenberg exchange Hamiltonian with $SO(5)$ symmetry. Depending on the ratio of spin exchanges J_0 and J_2 from the bond spin singlet and quintet channel we identify a Nêel phase at large J_0/J_2, a magnetic dimer phase at $J_0/J_2 \sim 1$, and a non-magnetic dimer phase at small J_0/J_2.

6.2 Introduction

Recently it has been shown that quantum systems governed by high-dimensional symmetry groups, such as $SU(N)$ and $Sp(2N)$, can provide fruitful exotic quantum effects. Among them, the study of the $SU(N)$ quantum magnetism has a long history.[119, 120, 121, 122, 123, 124, 125, 126, 127, 128, 129, 130, 131] One of practical proposals is the Kugel-Khomskii model,[132] which is used to describe the interplay between spin and orbital degrees of freedom in transition-metal oxides.[133, 134, 135, 136, 137, 138, 139] In this model the orbital degree is described as a pseudo-spin

operator and the model exhibits a full $SU(4)$ symmetry. Alternatively, ultracold fermionic alkaline-earth atoms can play a fundamental role as large-hyperfine spin and provide another platform to study even higher symmetry quantum magnetism (for $N > 4$).[140, 141, 142] For example, recent experiments have demonstrated an $SU(6)$ Mott insulating state by an atomic Fermi gas of ^{173}Yb in a 3D optical lattices,[143] the $F = \frac{9}{2}$ fermi gas of ^{87}Sr,[144, 145] a Mott-insulator to superfluid transition of bosonic Yb atoms in the optical lattice,[146] and the $SU(2) \times SU(6)$ system by a degenerate Fermi gas of mixture of ^{171}Yb and ^{173}Yb.[147] Theoretically, the Mott insulators of alkaline earth atoms have been suggested to have other exotic many-body phases, such as the four-site singlet plaquette ordering[148, 149] and quantum liquid states.[150, 151, 152, 153]

On the other hand, the simplest high-dimensional symplectic group is the $Sp(2N)$ group at $N = 2$, which can be established in the spin-3/2 system.[154, 155, 156, 149] Rather than the $SU(4)$ group, the $Sp(4)$ group, or isomorphically the $SO(5)$ symmetry, is more intrinsic in the spin-3/2 system since a spin-3/2 fermion forms the fundamental (spinor) representation of the $Sp(4)$ symmetry.[154] In this chapter, we study a specific $Sp(4)$ Heisenberg exchange model, which is derived in the strong interaction limit on a optical lattice at quarter filling. The novel magnetic model has two spin exchange channels: spin singlet J_0 and quintet J_2. The 1D phase diagram has been studied using the method of bosonization[155, 156] and numerically confirmed by the Density matrix renormalization groups method.[149] The 2D problem is more challenging. The Quantum Monte Carlo suffers notorious sign problems. Up to now, only at $J_2 = 0$ but $J_0 = J$ (the $SU(4)_B$ point), where the fundamental representation and anti-fundamental representation are in staggered arrangement, the ground state is found to be a Néel ordering state.[123, 125, 157] At $J_0 = J_2 = J$,

(the $SU(4)_A$ point) where each site is in the fundamental representation, however, the controversy still remains. The exact diagonalization studies on a 4×4 cluster suggest an $SU(4)$ singlet plaquette nature[137, 138, 149]. A variational Monte Carlo study concludes a spin liquid ground state.[158] Recently a study combined with the

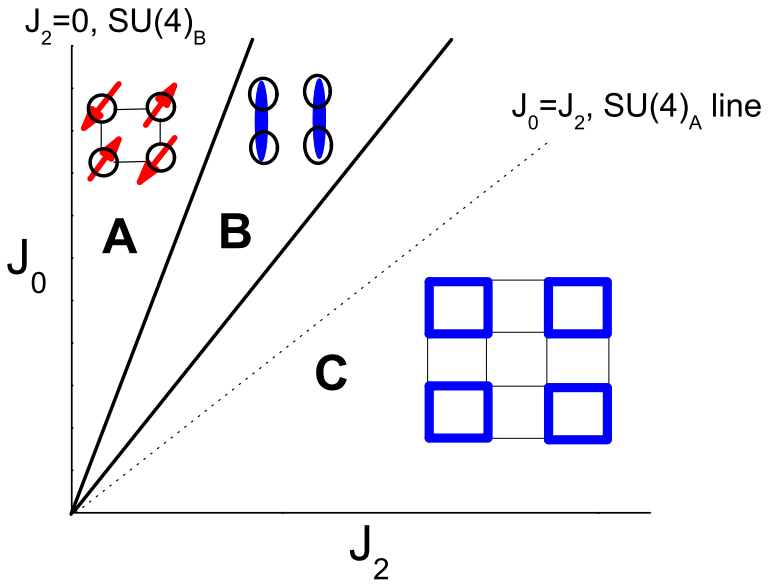

Figure 6.1: The tentative $Sp(4)$ phase diagram in the 2D $Sp(4)$ Heisenberg model. Phase A is a Néel ordering. Phase B denotes a $Sp(4)$ dimerized state. Phase C denotes a possible 4-site singlet plaquette state. J_0 and J_2 denote the spin singlet and quintet exchanged, respectively. The two $SU(4)$ limits are shown in the $SU(4)_{A,B}$ lines.

infinite-projected entangled-pair states method (iPEPS), exact diagonalization, and flavor-wave theory provides evidence of an $SU(4)$ symmetry broken dimer state.[43] Beyond these two special points, only a 4×4 exact diagonalization study[149] is conducted on the whole $Sp(4)$ parameter space, which, however, may suffer strong finite size effects. So far, for the 2D problem, only Ref. [156] gives the tentative $Sp(4)$ phase diagram which is shown in Fig. 6.1.

Complementary to the small cluster exact diagonalization study,[149] here we employ the iPEPS algorithm to investigate the $Sp(4)$ magnetic exchange model for other J_2/J_0 values in the thermodynamic limit. The main result is as follows. We

found that there exist three different phases. The $Sp(4)$ Néel state as suggested by previous work[149] is confirmed to exist with a finite extent including the $SU(4)_B$ line. This property agrees with the schematic phase A in Fig. 6.1. On the $J_0 = J_2$ line, a translation symmetry broken dimer state shown as the phase B dominates. Interestingly, the dimers carry magnetization. When $J_0 < J_2$, we find this model also exhibits another possible phase, which preserves the $SO(5)$ symmetry in spin pattern but still carries the dimerization pattern as depicted in the phase C. This signals a singlet nonmagnetic dimer order.

This chapter is organized as follows. In Sec. 6.3 we outline the $Sp(4)/SO(5)$ algebra and describe the corresponding high symmetry exchange Hamiltonian. A novel numerical method, the iPEPS algorithm is introduced in Sec. 6.4. This algorithm can be used to study the 2D system without worrying about sign problems. In Sec. 6.5 we show the iPEPS results to analyze the ground state behavior and support the phase diagram picture. Finally we summarize and propose open questions for the 2D exchange model behind the iPEPS results.

6.3 The $SO(5)/Sp(4)$ magnetic exchange Model

The $Sp(4)/SO(5)$ symmetry can be considered in the single-band $F = \frac{3}{2}$ ultracold fermionic Hubbard model on a 2D square lattice. The Hamiltonian reads

$$H = -t \sum_{\langle i,j \rangle, \sigma} c^{\dagger}_{i,\sigma} c_{j,\sigma} - \mu \sum_{i} n_{i,\sigma} + \frac{U}{2} \sum_{i} n_i (n_i - 1), \tag{6.1}$$

where σ runs $F_z = \pm\frac{3}{2}, \pm\frac{1}{2}$ and $U > 0$ is repulsive. The Hubbard Hamiltonian preserves the $SU(4)$ symmetry intrinsically. However, the Pauli exclusion principle prohibits two electrons with the triplet ($S_T = 1$) and the septet ($S_T = 3$) spin wavefunction staying on the same site. Therefore, the Hubbard interaction term is

reduced to

$$H_U = U_0 \sum_{i\sigma} P^\dagger_{00,i} P_{00,i} + U_2 \sum_{i,m=-2,\cdots,2} P^\dagger_{2m,i} P_{2m,i}, \tag{6.2}$$

where $P^\dagger_{00,i}$ and $P^\dagger_{2m,i}$ are the singlet and quintet pairing operators given by[154, 156]

$$P^\dagger_{Fm,i} = \sum_{\alpha\beta} \langle \frac{3}{2}\frac{3}{2} Fm | \frac{3}{2}\frac{3}{2} \alpha\beta \rangle c^\dagger_{\alpha,i} c^\dagger_{\beta,i}, \tag{6.3}$$

where $\langle \frac{3}{2}\frac{3}{2} Fm | \frac{3}{2}\frac{3}{2} \alpha\beta \rangle$ is the Clebsh-Gordan coefficient. As $U_0 = U_2$, the Hubbard model still has an $SU(4)$ symmetry. Fine tuning is needed to acquire the $SU(4)$ symmetry, however. The more generic case is as $U_0 \neq U_2$. The prohibited $S_T = 1$ and $S_T = 3$ channels together form a 10-dimensional degrees of freedom, implying a hidden $Sp(4)$ symmetry.

The $Sp(4)$ group, or isomorphically the $SO(5)$ group, is the subgroup of the $SU(4)$ group. Physically, the $SO(5)$ group can visualized as a rotational symmetry group defined on the 5-dimensional axis space. The $SU(4)$ algebra is spanned by 15 generators, of which 10 are time-reversal odd, whereas the remaining 5 generators are time-reversal even. The 10 time-reversal odd $SU(4)$ generators form the $Sp(4)$ group, and in this paper they are denoted as $L_{ab}(i) = -\frac{1}{2} c^\dagger_{\alpha,i} \Gamma^{ab}_{\alpha\beta} c_{\beta,i}$, where $\Gamma^{ab} = -\frac{i}{2}[\Gamma^a, \Gamma^b]$ and Γ^a for $a = 1 - 5$ are the five Dirac Gamma matrices. The explicit structures of Γ^a and Γ^{ab} can be found in Refs. [156, 149, 159]. By the chosen convention, L_{15} and L_{23} are good quantum numbers and span the Cartan subalgebra of the $Sp(4)$ group (similar to F_z of the $SU(2)$ group).

With the strong repulsive interactions, following the derivation in Ref. [160], the Heisenberg type exchange can be obtained through the second order perturbation theory as $J_0 = 4t^2/U_0$ and $J_2 = 4t^2/U_2$. At *quarter-filling*, the new exchange Hamiltonian can be expressed in terms of the 10 $Sp(4)$ generators L_{ab} and the 5-component

$Sp(4)$ vector n_a as

$$\begin{aligned} H &= \sum_{\langle i,j\rangle}\Big\{\frac{J_0+J_2}{4}\sum_{1\le a<b\le 5} L_{ab}(i)L_{ab}(j) \\ &+ \frac{3J_2-J_0}{4}\sum_{a=1-5} n_a(i)n_a(j)\Big\}. \end{aligned} \tag{6.4}$$

where $n_a(i) = \frac{1}{2}c^\dagger_{\alpha,i}\Gamma^a_{\alpha\beta}c_{\beta,i}$ are invariant under the $SO(5)$ rotation. In the $SU(2)$ language, the 3 rank-1 spin operators $\{F_x, F_y, F_z\}$ can be translated from the generators of $\{L_{ab}\}$ and $\{n_a\}$ as $F^+ = \sqrt{3}(L_{34}+iL_{24}) - (L_{12}+iL_{25}) + i(L_{13}+iL_{35})$ and $F_z = L_{23}+2L_{15}$. In the following we parameterize $J_0 = \sqrt{2}\sin\theta J$ and $J_2 = \sqrt{2}\cos\theta J$ and set J as our energy unit. Under such a convention, the $SU(4)_{A,B}$ are at $\theta = 45°$ and 90°, respectively.

From Eq. (6.4), it is clear to see the two $SU(4)$ limits. At $J_0 = J_2 = J$, the Hamiltonian on a bond becomes

$$\frac{J}{2}\Big\{\sum_{1\le a<b\le 5} L_{ab}(i)L_{ab}(j) + \sum_{a=1-5} n_a(i)n_a(j)\Big\}, \tag{6.5}$$

which is $SU(4)$ invariant. On the other hand, as $J_2 = 0$ the $SU(4)_B$ Hamiltonian is recast as

$$\frac{J}{4}\Big\{\sum_{1\le a<b\le 5} L_{ab}(i)L_{ab}(j) - \sum_{a=1-5} n_a(i)n_a(j)\Big\}. \tag{6.6}$$

This form seems to break the $SU(4)$ symmetry. However, in a bipartite lattice (A, B sublattices) by performing the particle-hole transformation to one of sublattices, e.g. $L'_{ab}(i) = L_{ab}(i)$ for all i and $n'_a(i) = -n_a(i)$ for $i \in A$ but $n'_a(i) = n_a(i)$ for $i \in B$,[156, 149] we can have

$$\frac{J}{4}\Big\{\sum_{1\le a<b\le 5} L'_{ab}(i)L_{ab}(j) + \sum_{a=1-5} n'_a(i)n_a(j)\Big\}, \tag{6.7}$$

which also shows an $SU(4)$ invariance. Our goal here is to explore the generic 2D exchange model Eq. (6.4) for all $\theta \neq 90°$ in the thermodynamic limit.

6.4 iPEPS method

One of modern tools to study the 2D $Sp(4)$ Heisenberg model is the infinite-projected-pair state algorithm (iPEPS).[161, 44] In the iPEPS ansatz, any arbitrary wave functions can be represented as the tensor network states,[162, 113, 163] which is typically written as (if there are two sites in a unit cell)

$$|\Psi\rangle = \mathrm{Tr} \prod_{i\in A, j\in B} A_{w_i x_i y_i z_i}[\sigma_i] B_{w_j x_j y_j z_j}[\sigma_j] |\sigma_i \sigma_j\rangle, \tag{6.8}$$

where site tensors A and B are rank-5 tensors due to a physical bond (the spin index σ) and four virtual bonds of dimension D connecting to four nearest neighbor sites ($wxyz$) and the trace is taken on all connected virtual bonds. To incorporate possible translational symmetry broken patterns with four-site periodicity,[138, 149] we extend the unit cell to a 4×4 cluster, namely totally 16 different tensors in our iPEPS calculations. The variational ground state $|\Psi_0\rangle$ is reached by performing an imaginary time evolution projecting onto a trivial wave function $|\Psi_T\rangle$

$$|\Psi_0\rangle = \lim_{\tau\to\infty} \frac{e^{-\tau H}|\Psi_T\rangle}{||e^{-\tau H}|\Psi_T\rangle||}. \tag{6.9}$$

To be unbiased, we input the trial wavefunctions randomly. We take a number of the random initial states for the imaginary time evolution and pick up the ground state as the one which has the minimum energy over all the trials to avoid being stuck in a metastable state. For large bond dimensions $D \geq 5$, $\mathbb{Z}_2$ symmetry[164, 165] is implemented in the calculation.

In the iPEPS the expectation values and correlation functions in the the thermodynamic limit can be computed by introducing boundary tensors to approximately contract the tensor network. Another virtual bond dimension χ associated to this boundary tensor is used to control the accuracy. As a rule of thumb $\chi \gtrsim D^2$ should be used to ensure the convergence of the results.

To benchmark our results we compare the ground state energy per bond ($E_0/2N$) with another iPEPS work[43] at $\theta = 45°$ and show in Fig. 6.2 (a). Thereafter N is denoted as the number of sites so that the number of bonds is $2N$. Our ground state energy at $D = 7$ is $E_0/2N = -0.3467$, which is close to the earlier result $E_0/2N \sim -0.35$ at $D = 8$.[43] Our iPEPS result in the $D \to \infty$ limit shows a asymptotic convergent behavior. The resultant ground state energy seems to extrapolate to the

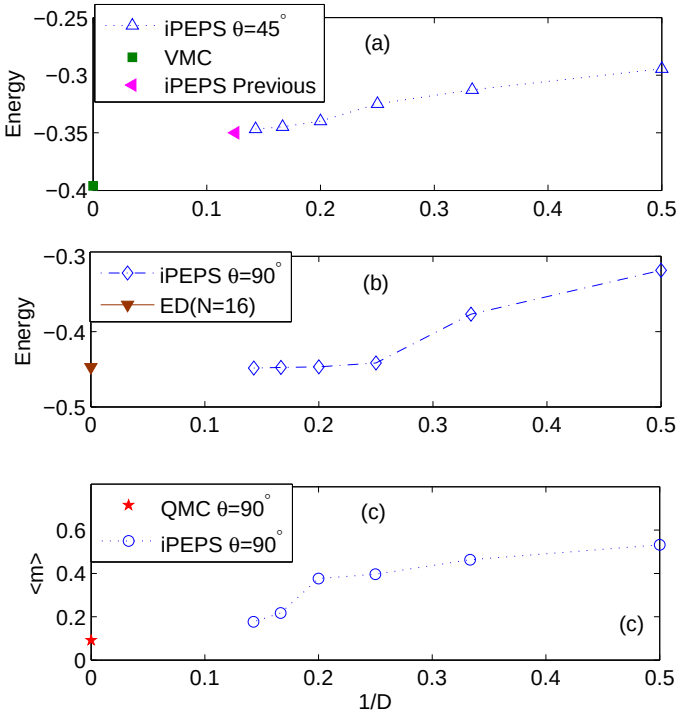

Figure 6.2: The Ground state energy per bond $E_0/2N$ as functions of $1/D$ at (a) $\theta = 45°$ and (b) $\theta = 90°$. (c) shows the staggered $SU(2)$ magnetization $\langle m \rangle_s$ at $\theta = 90°$ as functions of $1/D$. For comparison, we mark the ground state energies at $\theta = 45°$ and $\theta = 90°$ in (a) and (b) from other methods,[158, 43, 149] respectively, as well as the magnetization at $\theta = 90°$ from quantum Monte Carlo[123] in (c).

variational Monte Carlo result $E_0/2N = -0.396$.[158] In the other $SU(4)$ limit, the $1/D$ extrapolated value of $E_0/2N$ at $\theta = 90°$ in Fig. 6.2 (b) also shows comparable to the previous exact diagonalization study,[149] which roughly estimates as $E_0/2N = -0.4473$ in the $N \to \infty$ limit.

A more strict test is to examine the staggered magnetization at $\theta = 90°$ with the previous Quantum Monte Carlo results. It is known that at this point the $SU(4)$ Heisenberg model supports a Néel order ground state on the square lattice with a small $SU(2)$ magnetization $\langle m \rangle_s = 0.091$.[123, 119] By the iPEPS, Fig. 6.2 (c) shows the staggered $SU(2)$ magnetization at $\theta = 90°$ as a function of $1/D$, where $\langle m \rangle_s = \sqrt{\langle F_x \rangle_s^2 + \langle F_y \rangle_s^2 + \langle F_z \rangle_s^2}$, where $\langle O \rangle_s = \frac{1}{N} \sum_i (-1)^i \langle O_i \rangle$ means the staggered average. We found that up to $D = 7$ the $D \to \infty$ extrapolation is consistent with the Quantum Monte Carlo study in Ref. [123]. These benchmarks show that our iPEPS calculations can obtain a good description for the ground state wavefunction and provide well-controlled physical quantities. In the following section, we present the iPEPS results for other values of θ.

6.5 Numerical results

We calculate $SU(2)$ spin configurations $\langle F_z \rangle$, the bond energy $\langle h_{ij} \rangle$ configuration, where h_{ij} is the two-sites Hamiltonian as shown in Eq. (6.4) and two-point spin-spin correlation functions $\langle \vec{F}_i \cdot \vec{F}_j \rangle$. The ground state pictures are summarized in Fig. 6.3. Note that we consider 16 sites in a unit cell in the iPEPS calculations. The magnetization magnitudes and bond intensities are denoted by red arrows and blue lines, respectively. The thickness of bonds scales as the corresponding bond energy value and the length of the spin scales as the magnetization magnitudes.

Our iPEPS results confirm the existence of the Néel order in a finite region since the staggered spin configuration still survives at $\theta = 60°$ [c.f. Fig. 6.3 (b)]. Surprisingly, at $\theta = 45°$, the iPEPS shows both a dimerized pattern and a non-vanishing magnetization on each site in Fig. 6.3 (c). The spin orientations between different dimers show a staggered structure, which agrees with the former results[43].

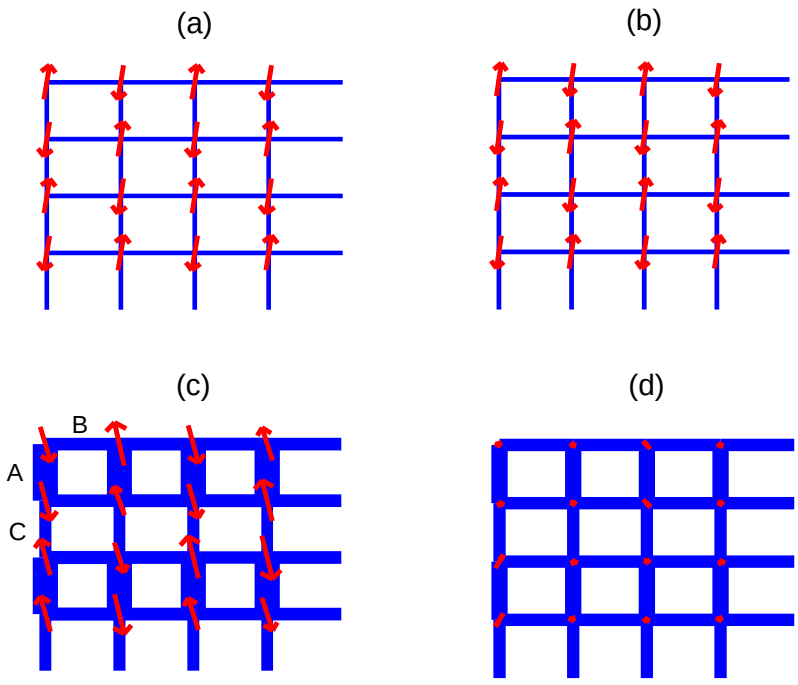

Figure 6.3: Bond-energy and spin-configuration pattern from iPEPS calculation on a 4×4 unit cell at (a) $\theta = 90°$, (b) $\theta = 60°$, (c) $\theta = 45°$, and (d) $\theta = 10°$. The thickness of bonds is proportional to its energy in magnitudes and the length of the spin is proportional to its magnetization. In (c) A, B, and C denote three different bonds in a dimerized state. All presented results use $D = 7$.

At small θ, we infer that the ground state is a dimer phase which does not break the $SO(5)$ symmetry as described in Fig. 6.3 (d). The suggested plaquette phase is not observed.

6.5.1 Spin configurations

First, let us analyze the ground state spin configuration. In the iPEPS calculations, the spontaneous $Sp(4)$ symmetry breaking allows us to measure the local moment directly. For convenience we present spin configurations by projecting $SU(2)$ spin (F_x, F_y, F_z) to $x - z$ plane. The $SU(2)$ spin patterns in Fig. 6.3 (a) and (b) confirm that the Néel phase exists not only at $\theta = 90°$ but also extends to $\theta = 60°$.

The Néel state can be identified not only by the staggered $SU(2)$ spin pattern but also other local measurements. To further understand the nature of the phase, we demonstrate several local order parameters calculated by the iPEPS at $D = 7$ for all θ values in Fig. 6.4. In the $SO(5)$ language we can further consider the staggered

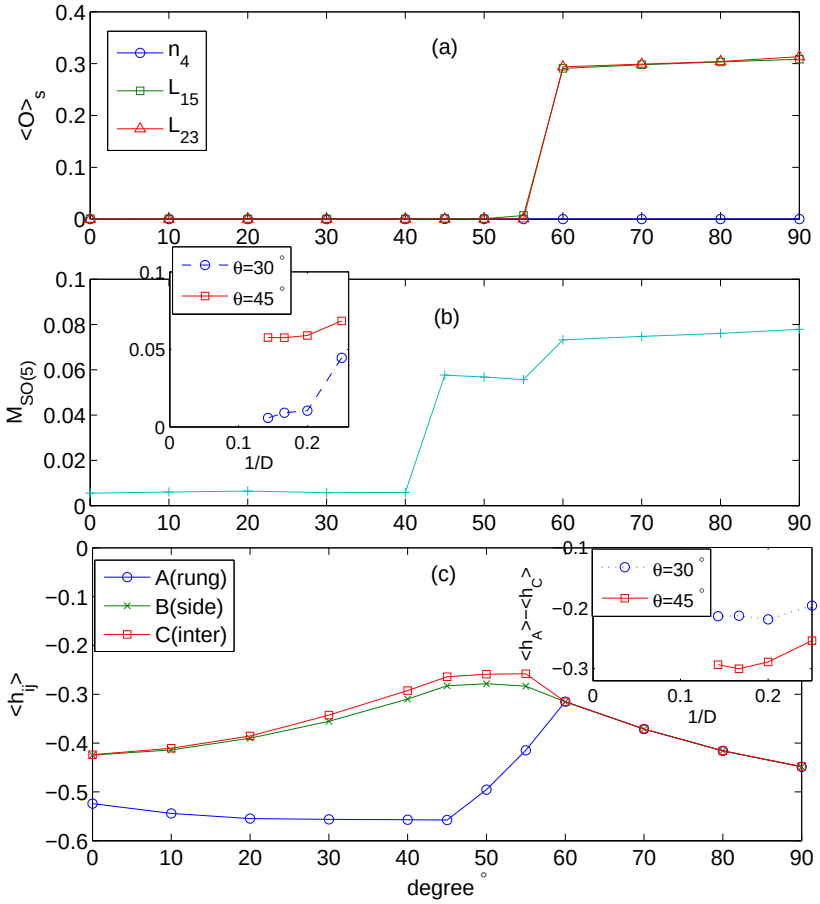

Figure 6.4: (a) Staggered average of $\langle L_{15}\rangle_s$, $\langle L_{23}\rangle_s$ and $\langle n_4\rangle_s$ as functions of θ. (b) The $SO(5)$ magnetization $M_{SO(5)}$ as a function of θ. (c) The bond energy $\langle h_{ij}\rangle$ on A, B and C bonds vs θ. All presented results use $D = 7$. In (b) and (c) the insets show the finite D scaling of the M_{SO5} and the difference in energy of bond A and C at $\theta = 30°$ (blue cycles) and $\theta = 45°$ (red squares).

average $\langle O\rangle_s = \sum_i (-1)^i \langle O_i\rangle$ over all lattice sites on three diagonal $SU(4)$ operators $O = L_{15}$, L_{23} and n_4. Fig. 6.4 (a) shows that $\langle L_{15}\rangle_s = \langle L_{23}\rangle_s$ for all parameters due to the $SO(5)$ symmetry. The value of $\langle L_{15}\rangle_s$ drops to zero dramatically at

$\theta < 60°$, indicating the vanishing staggered magnetization. While $\langle L_{ab}\rangle_s$ shows a staggered behavior in the Néel phase, $\langle n_a\rangle_s$ has the zero staggered magnetization. Such behavior was realized that n_4 has the uniform magnetization.[149] At $\theta = 90°$, we can perform the particle-hole transformation $L'_{ab} = L_{ab}$ and $n'_a = -n_a$ on one of sublattices but keep the other remain, as mentioned in Sec. 6.3. This brings the behavior of $\langle n_a\rangle$ opposite to a staggered arrangement so n_a has a uniform magnetization.

In the $Sp(4)$ Heisenberg exchange model, we further calculate the $Sp(4)/SO(5)$ magnetization which is defined as[166]

$$M_{SO(5)} = \frac{1}{N}\sqrt{\sum_{i,a,b}\langle L_{ab}(i)\rangle^2}, \tag{6.10}$$

where L_{ab} are the 10 $SO(5)$ generators. A finite $M_{SO(5)}$ implies that the $SO(5)$ symmetry is spontaneously broken in the thermodynamic limit, which has a physical meaning similar to measure the local $SU(2)$ moment. In Fig. 6.4 (b) we observe that the $SO(5)$ local moment still survives even at $\theta < 60°$ and vanishes as $\theta < 45°$. This implies that in the region of $45° < \theta < 60°$ there exist finite local moments, but not in a staggered pattern. At $\theta = 45°$, the sudden drop on the $SO(5)$ magnetization suggests a magnetic phase transition. Below 45°, the ground state is nonmagnetic. To confirm this result in the infinite D limit we compare the finite D scaling behaviors of $M_{SO(5)}$ at $\theta = 30°$ and $\theta = 45°$. In the inset of Fig. 6.2 (c) we can clearly observe that $M_{SO(5)}$ at $\theta = 30°$ seems to extrapolate to a small value, but saturates to a finite value at $\theta = 45°$ in the infinite D limit.

6.5.2 Bond energy configurations

Next we examine the bond configurations by calculating $\langle h_{ij}\rangle$. A translational symmetry breaking phase can be easily identified through observing the bond-energy

with a staggered pattern due to the existence of dimerization. On the other hand, a homogeneous bond pattern shows no translational symmetry broken. We start our discussion on the region of $60^\circ < \theta < 90^\circ$. In Fig. 6.3 (a) and (b), the bond-energy distribution is homogeneous implying that there is no further spatial symmetry breaking. This feature matches up our previous ground state identification of this regime where it is the $Sp(4)$ Néel state, which breaks the $SO(5)$ symmetry but preserves the translation symmetry.

Let us move to the regime of $45^\circ < \theta < 60^\circ$. In this regime, the staggered magnetization is zero but there exists a finite $SO(5)$ local moment. Meanwhile, the bond energy in Fig. 6.3 (c) shows a clear signature of dimerized pattern with non-vanishing magnetization. It is suggested that at $\theta = 45^\circ$ the ground state has a Néel like order with dimers alternating between pairs of colors at this point.[43] The feature of coexisting finite $Sp(4)$ local moments and spatial dimerization indicates the signal of a magnetic dimer phase.

In an $SU(2)$ case , the spin-singlet dimer is $|\frac{1}{2}, 0\rangle = \frac{1}{\sqrt{2}}(|\sigma, \bar{\sigma}\rangle - |\bar{\sigma}, \sigma\rangle)$, and the triplet dimers are $|\frac{1}{2}, 1\rangle = \frac{1}{\sqrt{2}}(|\sigma, \bar{\sigma}\rangle + |\bar{\sigma}, \sigma\rangle)$, $|\sigma, \sigma\rangle$ and $|\bar{\sigma}, \bar{\sigma}\rangle$, where $\sigma = \frac{1}{2}$. In a two-site $Sp(4)$ exchange problem, the representation is decomposed as $4 \otimes 4 = 1 \oplus 5 \oplus 10$. The singlet state spans the identity representation, 5-dimensional and 10-dimensional states span the vector representation and the adjoint representation, respectively. The 5-component dimers (with Casmir $C = 4$) always have lower energy than the 10-component dimers and can be written as the combination of $a|\frac{3}{2}, 0\rangle \pm b|\frac{1}{2}, 0\rangle$ or other more complicated forms, depending on the value of θ.

To further understand the dimerization phase, we calculate the bond energy for all θ. In Fig. 6.3 (c), we can see that there exists a staggered bond energy configuration. For convenience, we choose "A" bonds which have stronger bond energy than the

neighboring bonds which we define "B" bonds. The "C" bond is selected as the bond which is perpendicular to the A and B bonds. The schematic positions of the A, B and C bonds are labeled in Fig. 6.3(b). In Fig. 6.4 (c), the energy on B and C bonds are similar but the two bonds have well-separated energy compared to the A bond energy. Fig. 6.3 (c) and Fig. 6.4 (c) indicate $(\pi, 0)$ dimer configuration and the dimerization signature persists in the region of $\theta < 60°$. We do not find the (π, π) staggered dimer configuration to be a ground state in our calculation. Since our iPEPS algorithm is biased to neither of them we suggest a staggered dimer state is not likely to be a true ground state. The occurrence of dimerized behavior and vanishing staggered magnetization almost takes place at the same θ point. This signature implies that $\theta = 60°$ is a transition from Néel ordering to the magnetic dimer phase.

Upon decreasing θ, the dimerized pattern with vanishingly small magnetization is observed. This pattern exists in a finite regime of $0 \leq \theta < 45°$. The representative ground state picture is depicted in Fig. 6.3 (d) chosen at $\theta = 10°$. The small magnetization in this region hints a non-magnetic ground state. For the $Sp(4)$ exchange, a two-site nonmagnetic dimer (Casimir $C = 0$) universal written as

$$|\frac{3}{2}, C = 0\rangle = \frac{1}{\sqrt{2}}(|\frac{3}{2}, 0\rangle - |\frac{1}{2}, 0\rangle).$$

Although the dimerization is weak compared to larger θ values, we still can see the possible dimer ordering pattern shown in Fig. 6.3 (d). To confirm the weak dimer pattern at small θ, we show the energy difference of A and C bonds as functions of $1/D$ at $\theta = 30°$ and $45°$ in the inset of Fig. 6.4(c). The energy difference persists as we increase the D values and show the convergent behavior. This confirms the dimer pattern as a robust feature in both phases.

6.5.3 Two-point $SU(2)$ spin-spin correlations

To ensure the long-range magnetic order we calculate the two-point $SU(2)$ spin-spin correlation functions $\langle \vec{F}_i \cdot \vec{F}_j \rangle$ of spins along the diagonal direction on our unit cell in Fig. 6.5. In the Néel phase as distinguished at $60° < \theta < 90°$, we indeed observe true long-range orders. At $\theta = 60°$ and $\theta = 90°$, the two-point spin-spin correlations

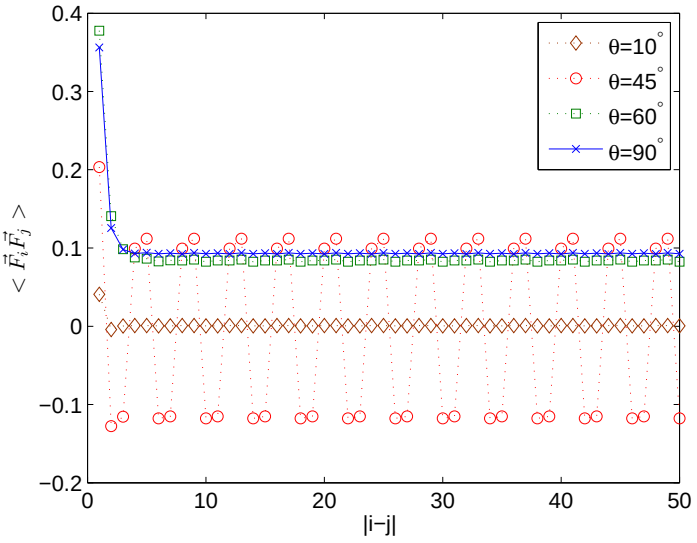

Figure 6.5: (Color online) The two-point spin-spin correlation functions $\langle \vec{F}_i \cdot \vec{F}_j \rangle$ of spins sitting on the diagonal direction in the unit cell evaluated at $D = 7$ at $\theta = 10°$(diamond), $\theta = 45°$(circle), $\theta = 60°$(square), and $\theta = 90°$(cross).

saturate to finite values, which indicates the long-ranged correlation behavior. At $\theta = 45°$ which belongs to a magnetic dimer phase, the correlation function exhibits a four-site periodicity in correspondence to the dimer pattern shown in Fig. 6.3(c). Besides, a convergent finite spin-spin correlation in the long distance is also found whihc confirms a magnetic order. On the other hand, the correlation function at $\theta = 10°$ exhibits an exponential decays and goes to zero after 2 sites. Such extremely short correlation suggests that this belongs to a non-magnetic phase and is consistent with the phase picture given in Fig. 6.3 (d).

6.6 Chapter Summary

To sum up, we study a $SO(5)$ spin Heisenberg model which can be realized with quart-filled spin $\frac{3}{2}$ fermions in the square optical lattice. Numerical results are obtained through iPEPS tensor network algorithm. We find three different phases: a Nêel phase at large θ, a magnetic dimer phase around $\theta = \pi/4$, and a dimer phase preserving $SO(5)$ symmetry at small θ. Previous studies with ED and analytic method confirm the Nêel phase at large θ. The magnetic dimer phase has also been shown in a recent work. Our results suggest a new dimer phase with $SO(5)$ symmetry at small θ, which has not been reported before.

CHAPTER VII

Topological Bose-Mott Insulators in a One-Dimensional Optical Superlattice

7.1 Overview

We study topological properties of the Bose-Hubbard model with repulsive interactions in a one-dimensional optical superlattice. We find that the Mott insulator states of the single-component (two-component) Bose-Hubbard model under fractional fillings are topological insulators characterized by a nonzero charge (or spin) Chern number with nontrivial edge states. For ultracold atomic experiments, we show that the topological Chern number can be detected through measuring the density profiles of the bosonic atoms in a harmonic trap.

7.2 Introduction

Ultracold atoms in optical lattices can be used to simulate strongly correlated many-body models that are central to the understanding of condensed matter physics. This simulation has attracted a lot of attention as the optical lattice experiments offer unparalleled controllability and new tools to study many-body physics [2, 28, 109, 167]. As a remarkable example, the Bose-Hubbard (BH) model has been experimentally realized with ultracold atoms and a quantum phase transition from a

superfluid to a Mott insulator described by this model has been observed [2]. On the other hand, systems with nontrivial topological properties, such as quantum Hall systems and topological insulators, are of fundamental importance in physics [168]. Recently, studying topological phases with ultracold atoms has raised great interest [109, 169, 170, 171, 172, 116, 173, 174]. In general, it requires complicated control of experimental systems to realize topological phases with ultracold atoms. An interesting question is whether one can observe topological phases in a simple BH type of model, which can be readily implemented by many experimental groups. Topological properties of bosonic systems, however, have not been well-studied in literature, partly for the reason that the topological invariants are usually defined as an integration over all the occupied states in the momentum space [175, 176]. This definition does not apply directly to the bosonic system as many bosons can occupy the same momentum state.

In this chapter, in contrast to the conventional wisdom, we show that the BH model in a one-dimensional (1D) optical superlattice displays nontrivial topological properties. We demonstrate that the Mott insulators of the single-component (two-component) BH model at fractional fillings belong to topological matter with its phase characterized by a nonzero integer charge (or spin) Chern number. For Mott insulators, the bulk system has a gap in the excitation spectrum induced by the interaction. For a topologically nontrivial Mott insulator state characterized by a nonzero Chern number, we further show that there are protected edge states inside the bulk gap under the open boundary condition. The Mott insulators at integer fillings for this system remain topologically trivial with a zero Chern number and no edge states. The topological properties discussed here are reminiscent of those in topological Mott insulators theoretically predicted in Ref. [15] for the

Fermi-Hubbard model in a honeycomb lattice with frustrated next-neighbor interactions. Remarkably, we here show that topological Mott insulators can appear in a simple 1D BH model in an optical superlattice, which, besides being conceptually interesting, makes the experimental realization of topological matter much easier in the ultracold atomic system. We propose a scheme to detect the topological Chern number by observation of the plateaus of the density profile with ultracold atoms in a weak global harmonic trap as it is the case for experiments.

7.3 Single-component BH model in a superlattice

We consider a single-component bosonic gas loaded into a 1D optical lattice, which is described by the BH model

$$H = -J \sum_{\langle ij \rangle} b_j^\dagger b_i + \sum_j \left[U n_j (n_j - 1)/2 + V_j n_j \right], \tag{7.1}$$

where $V_j = V \cos(2\pi\alpha j + \delta)$ denotes a periodic superlattice potential [177], b_j and $b_j^\dagger$ correspond to the bosonic annihilation and creation operators of atoms on the jth lattice site, $n_j = b_j^\dagger b_j$ is the number operator, and J and U represent the hopping rate and the on site interaction strength, respectively. We consider in this chapter a commensurate superlattice potential V_j with $\alpha = p/q$ (p, q are integers) being a rational number and δ an arbitrary tunable phase, which has been experimentally realized [177]. We take J as the energy unit by setting $J = 1$.

The ground-state phase diagram of the Hamiltonian Eq.(7.1) is well-studied [178, 28, 2]. For a sufficiently large U, the system is in a gapped Mott insulator phase at commensurate fillings with $\nu \equiv N_b/N = m\alpha$, where m is an integer, N_b is the atom number, and N is the number of lattice sites. Away from the commensurate fillings or for a small U, the system is in a superfluid state [178]. In this chapter, we focus on the study of the topological properties of the Mott insulator phase.

7.3.1 The energy gap and the Chern number of the ground state

The topological property is best characterized by the Chern number. To calculate the Chern number, we first perform exact diagonalization of the Hamiltonian Eq.(7.1) on a chain of N sites with periodic or open boundary conditions [179]. The ground state is nondegenerate and separated from the higher eigenstates by a finite gap Δ at the commensurate fillings. This gap is shown in Fig. 7.1 as a function of the interaction strength U at $\nu = 1/3$. The gap increases monotonically with U and then saturates at a finite value. For a large U, the atoms become hard-core bosons. In this case, each site is occupied by no more than one atom. The hard-core boson Hubbard model can be mapped to a model of free fermions. From that mapping, we find that the saturation value of the gap is 1.08 (in units of J) at a large U for an infinite system. The gap should decrease to zero as U drops below a critical value U_c where the system transits to a superfluid phase. In Fig. 7.1, due to the finite size effect, the saturation value of the energy gap is above 1.08 for a large U and does not drop exactly to zero as U diminishes. However, as the number of lattice sites increases, we clearly see the tendency that the gap approaches these limiting values at the two ends.

Now, we investigate the topological property of the system by calculating the Chern number. For fermions, the Chern number is defined as an integration over the occupied states in the momentum space[175]. This definition can not be extended to the bosonic system as many bosons can occupy the same momentum state. Fortunately, there is another way to calculate the Chern number for interacting systems[180]: suppose the ground state has a gap to the excited state and it depends on the parameters θ, δ through a generalized periodic boundary condition $|\Psi(j+N,\theta,\delta)\rangle = e^{i\theta}|\Psi(j,\theta,\delta)\rangle$, where j denotes an arbitrary site, θ is the twist

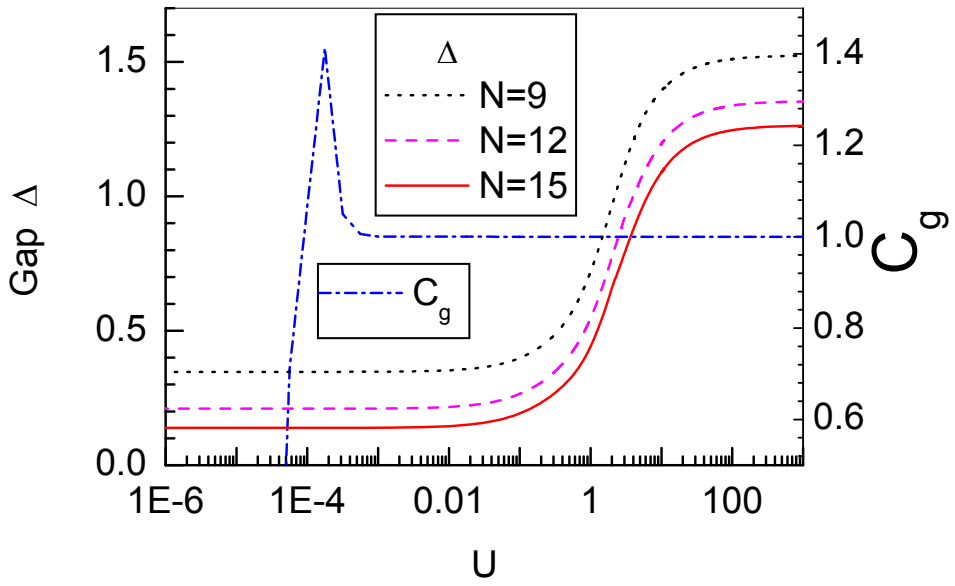

Figure 7.1: The energy gap Δ and the Chern number C_g defined by Eq.(7.2) as functions of the interaction strength U. The number of lattice sites $N = 9, 12, 15$ are used for exact diagonalization, and we take $N = 15$ for calculation of C_g. Other parameters include $V = 1.5$, $\delta = 2\pi/3$, $\alpha = 1/3$, and $\nu = 1/3$.

angle, and δ is the phase in the superlattice potential V_j. Under this boundary condition, we numerically diagonalize Hamiltonian Eq.(7.1) and derive the ground state $|\Psi(\theta, \delta)\rangle$, which is a non-degenerate state separated from the excited state by a nonzero energy gap Δ when $U > U_c$. For the ground state $|\Psi(\theta, \delta)\rangle$ where θ and δ vary on a torus, one can define the Chern number C_g as a topological invariant by the following formula [180]

$$C_g = \frac{1}{2\pi} \int_0^{2\pi} d\theta \int_0^{2\pi} d\delta (\partial_\theta A_\delta - \partial_\delta A_\theta), \tag{7.2}$$

where the Berry connection $A_\mu \equiv i\langle\Psi(\theta, \delta)|\partial_\mu|\Psi(\theta, \delta)\rangle$ $(\mu = \delta, \theta)$. We numerically calculate the Chern number C_g using the method for a discrete manifold [181]. When the parameter $\alpha = 1/3$, we find for this boson system that the Chern number $C_g = 1$ (-1) for the filling fraction $\nu = 1/3$ $(2/3)$ and $C_g = 0$ when $\nu = 1$. As an example, we show the value of C_g as a function of U at $\nu = 1/3$ in Fig. 7.1, where the manifold of torus is discretized by 5×5 meshes in the calculation. When the system

is in the gapped Mott state with $U > U_c$, C_g is quantized to be exactly at 1, while C_g is unquantized when the system enters the gapless superfluid phase. Because of quantization of C_g, the finite size effect seems to have a minimal influence, and we can use exact diagonalization of a small system to get the exact value of C_g in Fig. 7.1 for the Mott phase (however, because of the finite-size gap, C_g is still approximately unity in some region of the superfluid phase near the transition point). This calculation unambiguously shows that this bosonic system is in a topological Mott insulator phase with nonzero Chern number at the fractional filling of the optical lattice.

7.3.2 Edge states

The appearance of edge states at the boundary is usually considered to be a hallmark of nontrivial topological properties for the bulk system. Under the periodic boundary condition, this interacting system is gapped at the fractional filling $\nu = 1/3$ (or 2/3). However, under the open boundary condition, edge states confined to the boundary can appear inside the energy gap, signaling the nontrivial topological properties of the bulk insulator. The quasiparticle energy spectrum ΔE_n is determined by the additional energy required to add an atom to a system with n atoms, that is,

$$\Delta E_n^{(O,P)} \equiv E_{n+1}^{(O,P)} - E_n^{(O,P)}, \tag{7.3}$$

where $E_n^{(O)}$ ($E_n^{(P)}$) is the ground-state energy of the system with n atoms under the open (periodic) boundary condition[182]. In Fig. 7.2(a) , we show the quasi-particle energy spectrum for a system with 96 lattice sites near the filling $\nu = 1/3$ under both periodic and open boundary conditions. The calculation is done using the density matrix renormalization group method [17, 18], which provides a reliable approach to precisely calculate energies for any 1D systems. Near the filling $\nu = 1/3$, the quasi-

particle energy spectrum is split into two branches separated by a finite gap. The calculation clearly shows that two states appear in the gap of the energy spectrum under the open boundary condition. In Fig. 7.2(b), we show the quasi-particle energy spectrum as a function of phase δ under the open boundary condition. Inside the gap between the lower and the upper branches of the energy spectrum, one can see two edge modes (which are degenerate in energy at $\delta = 2\pi/3$) that connect these two branches of the bulk spectrum as one varies phase δ.

To verify that the in-gap modes indeed correspond to the edge states, we numerically calculate the excitation distribution of these modes and find that they are confined near the edges of the chain. The distribution of the quasi-particle can be defined as

$$\Delta n_j = \langle \Psi^g_{n+1} | n_j | \Psi^g_{n+1} \rangle - \langle \Psi^g_n | n_j | \Psi^g_n \rangle, \tag{7.4}$$

where $|\Psi^g_n\rangle$ denotes the ground state wave function of the system with n bosonic atoms. The distribution of the in-gap quasi-particle modes for $N = 96$ sites under filling $\nu = 1/3$ is plotted in Fig. 7.2(c). As expected, the in-gap states mainly distribute near the two edges, especially for a large V. For instance, 99% of the quasi-particle modes at $V = 10$ are localized at the two edge sites.

7.4 Two-component BH model in a superlattice and spin Chern number

If the phase δ in Eq. 7.2 is replaced by $-\delta$, we find that the Chern number is -1 (1) for $\nu = 1/3$ (2/3), that is, the sign of the Chern number is flipped. This fact implies that we can realize a topological insulator characterized by a nontrivial spin Chern number with a two-component bosonic gas in a 1D optical superlattice. To this end, we consider a simple case where the inter-component atomic collision

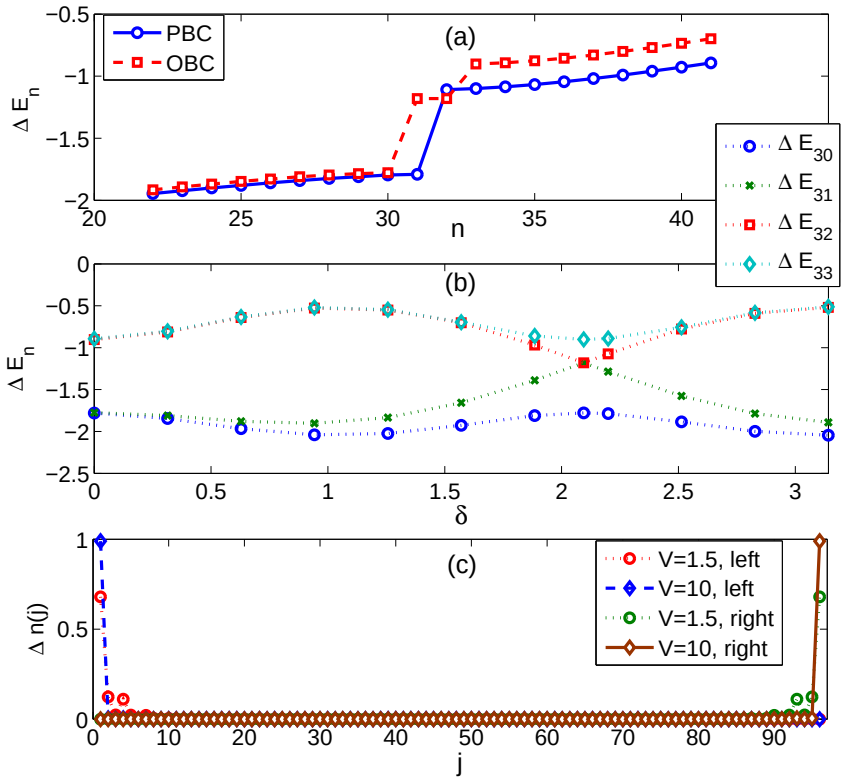

Figure 7.2: (a) The quasi-particle energy spectrum ΔE_n (see the definition by Eq. 7.4) versus n under the periodic (PBC) or open (OBC) boundary condition. The calculation is done in a 96-site lattice near the filling $\nu = 1/3$ with $V = 1.5$, $U = 10$, $\delta = 2\pi/3$, and $\alpha = 1/3$. (b) The edges of the lower (ΔE_{30}) and the upper (ΔE_{33}) branches of the energy spectrum and the two in-gap modes ($\Delta E_{31}$and ΔE_{32}) as functions of the phase δ under the open boundary condition. (c) The distribution of the two in-gap modes along the chain at $V = 1.5,\ 10$. The other parameters for (b) and (c) are the same as those for (a).

is turned off, e.g., through Feshbach resonance, and the system is described by a decoupled two-component BH model with the Hamiltonian

$$H = -J \sum_{\langle ij \rangle \sigma} b_{i\sigma}^{\dagger} b_{j,\sigma} + \sum_{j,\sigma} [\frac{U_\sigma}{2} n_{j\sigma}(n_{j\sigma} - 1) + V_{j\sigma} n_{j\sigma}], \tag{7.5}$$

where the potential $V_{j\sigma} = V \cos(2\pi\alpha j + \delta_\sigma)$ with $\delta_\uparrow = -\delta_\downarrow = \delta$, $b_{j\sigma}$ denotes the bosonic annihilation operator with the pseudo-spin $\sigma = \uparrow, \downarrow$, and U_σ is the intra-component interaction rate for spin σ. For this decoupled two-component BH model, we have the Chern number $C_g^\uparrow = -C_g^\downarrow$. So, although the total charge Chern number $C_g^\uparrow + C_g^\downarrow$ cancels out to zero, the spin Chern number $C_g^s = C_g^\uparrow - C_g^\downarrow$ [183] is non-vanishing at fractional fillings. The nonzero spin Chern number is usually associated with the quantum spin Hall effects in two-dimensional systems [183]. For our 1D system, spin edge states appear when the spin Chern number is nonzero. For an example with $\alpha = 1/3$, we have $C_g^s = 2$ at the fractional fillings $\nu = 1/3$ (2/3) and $C_g^s = 0$ at the integer filling. The edge states are similar to those shown in Fig. 7.2. The spin up (down) edge state is confined near the left (right) edge, respectively.

7.5 Experimental detection

We now discuss how to measure the topological Chern number in a practical experimental setting. For atomic experiments, apart from the optical superlattice potential, the bosons are confined in a weak global harmonic trap. For simplicity, we consider the large-U limit where the system is described by hard-core bosons with no more than one atom occupying the same lattice site. The total potential, including the optical superlattice and the global harmonic trap, is described by

$$V_j = V \cos(2\pi\alpha j + \delta) + V_H (j - j_0)^2, \tag{7.6}$$

where j_0 denotes the position of the trap center and V_H is the strength of the harmonic trap. We use the Jordan-Wigner transformation, $b_j^\dagger = f_j^\dagger \prod_{m=1}^{j-1} e^{-i\pi f_m^\dagger f_m}$ and $b_j = \prod_{m=1}^{j-1} e^{i\pi f_m^\dagger f_m} f_j$, to map the hard-core BH model to non-interacting fermion Hamiltonian $H_F = -J\sum_j (f_j^\dagger f_{j+1} + h.c.) + \sum_j V_j f_j^\dagger f_j$, where $f_j^\dagger$ and f_j are the creation and annihilation operators for spinless fermions, respectively[178, 184]. The particle density of hard-core bosons coincides with that of non-interacting fermions as we have $n_j = \langle b_j^\dagger b_j \rangle = \langle f_j^\dagger f_j \rangle = n_j^F$ with the Jordan-Wigner transformation; however, the momentum distribution for bosons is typically very different from that for fermions.

After the hard-core bosons are mapped to fermions, there is a simple way to figure out the Chern number. The ground state of free fermions is a Slater determinant, i.e., a product of single particle states $|\Psi_g^F\rangle = \prod_{m=1}^{N_f} \sum_{n=1}^{N} P_{nm} f_n^\dagger |0\rangle$, with $N_f = N_b$ the number of fermions and P the matrix of the components of $|\Psi_g^F\rangle$. Supposing that the n-th eigenstate of a single particle is denoted by $|\psi_n\rangle = \sum_j \phi_{j,n} f_j^\dagger |0\rangle$, the eigenvalue equation $H_F|\psi_n\rangle = E_n|\psi_n\rangle$ can be written in terms of the following Harper equation [173]

$$-J(\phi_{j+1,n} + \phi_{j,n}) + V\cos(2\pi\alpha + \delta)\phi_{j,n} = E_n \phi_{j,n}, \tag{7.7}$$

where $\phi_{j,n}$ is the amplitude of the particle wave function of the j-th site and E_n is the n-th single-particle eigen-energy. Compared with the Harper equation in a magnetic field, we know that α corresponds to the magnetic flux [176]. Therefore, we can define the local density difference as

$$\delta n_j = \frac{n_j(\alpha_1) - n_j(\alpha_2)}{\alpha_1 - \alpha_2}. \tag{7.8}$$

The Chern number C_g can then be obtained through the Streda formula $C_g = \delta n_j$ under the condition that $n_j(\alpha_\eta)$ $(\eta = 1, 2)$ is the local density associated with the

plateau at α_η[171, 170, 173, 174].

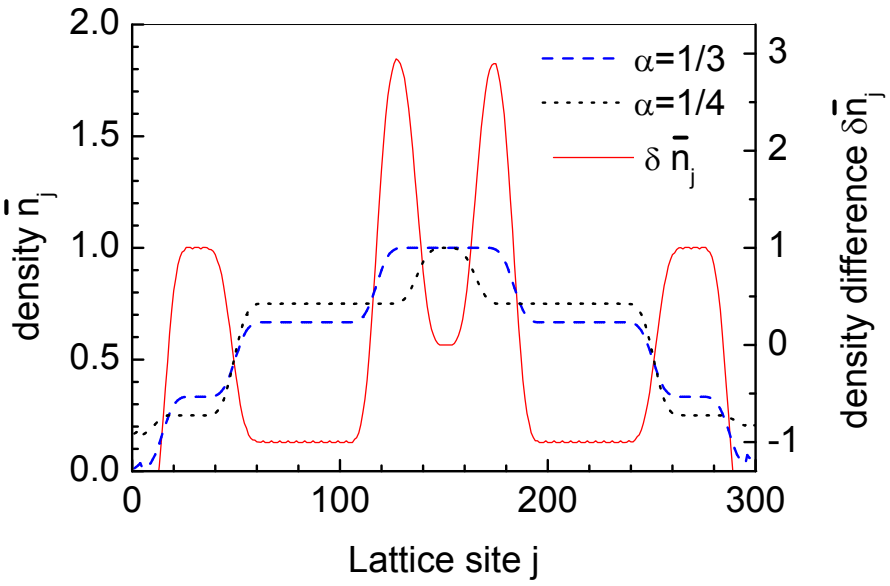

Figure 7.3: The average density profiles $\bar{n}_j$ and the density difference $\delta\bar{n}_j$ for $\alpha_1 = 1/3$ and $\alpha_2 = 1/4$. The values of $\delta\bar{n}_j$ represent the corresponding Chern numbers at the plateaus with the fillings $\nu = 1/3, 2/3, 1$ for $\alpha = 1/3$ and $\nu = 1/4, 3/4, 1$ for $\alpha = 1/4$. The other parameters are $N = 300$, $N_b = 180$, $M = 4$, $V = 10$, $\delta = \pi/2$, and $V_H = 0.001$.

Following the method outlined in Ref. [178], we numerically calculated the average density profiles for $\alpha = 1/3, 1/4$, with the results shown in Fig. 7.3. To reduce the oscillations in density profiles induced by modulation of the potentials, we define the local average density $\bar{n}_j = \sum_{m=-M}^{M} n_{j+m}/(2M+1)$, where $2M+1$ is the length to average the density, which corresponds to the position resolution in the experimental detection. We take $M \ll N$, e.g., $M = 4$ and $N = 300$ in Fig. 7.3, as it is typical for experiments. As one can see from the density profiles $\bar{n}_j$ in Fig. 7.3, plateaus appear at the rational fillings $\nu = 1/3, 2/3, 1$ for $\alpha = 1/3$, and $\nu = 1/4, 3/4, 1$ for $\alpha = 1/4$ (the gap at half filling in the case of $\alpha = p/q$ with an even q is generally closed at an integer δ/π [176]). Using the Streda formula Eq. (7.8), we obtain $C_g = \delta n_j = 1, -1$ at the fractional fillings $\nu = \alpha, 1-\alpha$, and $C_g = 0$ at the integer filling $\nu = 1$. The width of the plateaus is associated with the size of the energy gap.

To make detection of the Chern number easier, we can adjust the frequency of the harmonic trap to move the target plateaus to the center of the trap. For example, if we choose $V_H = 10^{-4}J$ and other parameters as those given in Fig. 7.3, the plateaus at $\nu = 2/3$ for $\alpha = 1/3$ and $\nu = 3/4$ for $\alpha = 1/4$ are moved to the center of the trap spanning from the 65th to the 235th lattice site. With such a wide plateau, it is straightforward to read out the Chern number $C_g = \delta\bar{n}_j = -1$ for this case.

7.6 Chapter Summary

In summary, we have shown that for bosonic atoms in a 1D optical super-lattice, the Mott insulator states of the corresponding BH model at fractional fillings are topologically nontrivial, characterized by nonzero Chern number and existence of edge states. We further predict that the topological Chern number can be detected by measuring the plateaus in the density profile when the atoms are trapped in a global harmonic potential. The model discussed in this chapter represents one of the simplest experimental systems to show intriguing topological properties, and the proposed detection method allows one to confirm these topological properties with the state-of-the-art technology.

CHAPTER VIII

Conclusions

8.1 Summary

In this dissertation, we have investigated the possibility to realize novel quantum phases with cold neutral atoms, polar molecules or dipolar atoms in an optical lattices. As novel manipulation methods and higher resolution microscopes are available in the cold atoms experiments it is important to have numerical results for these strongly correlated systems to serve as a guide in exploration of interesting physics there.

We have shown that spinless fermions with a Feshbach resonance in an optical lattice can have a stable p-wave superfluid phase. The effective model of this system is constructed by introducing a dressed molecule consisting of closed channel molecules and open channel atom pairs. The decay of Feshbach molecules due to three body collision processes is suppressed by the dissipation induced blockade mechanism. It has been shown the net collision loss is inversely proportional to the square of inelastic collision rate and the on-site atom-dressed-molecule interaction[67, 68]. This reduction in the population of three body states is the analogy of the quantum Zeno effect while in our case it is induced both by the enhanced interaction in optical lattices and dissipation. We have studied a limited one dimensional case and mapped

out the phase diagram in the plane of the chemical potential and interaction energy with the iTEBD method. In one dimension there is no true condensate thus a p-wave superfluid is identified with a quasi-long range order of superfluid order parameter, which shows a prominent kink at zero momentum in the Fourier space. Besides the p-wave superfluid there are two different insulating phases showing non-zero charge gaps. One is a Mott insulator with a conserved total number of atoms and molecules. The other is a dissipation induced insulator phase with a filling of one molecule per site. Here the dissipation induced phase is unique to cold atom systems since in condensed matter systems electrons can not decay and leave the system.

Since many condensed matter systems are studied in two dimension and interesting physics such as Quantum Hall effects and Berezinsky-Kosterlitz-Thouless phase transition occur there it is of great importance to have numerical methods that work in dimension higher than one. We have implemented the tensor network algorithm(iPEPS) which is a natural extension of the DMRG methods to 2D space and can be applied to retrieve physical properties in the thermodynamic limit directly. To demonstrate its ability in dealing with two dimensional frustrated systems we have studied the phase diagram of the Heisenberg model on a checkerboard lattice. It is generally believed depending on the ratio of nearest to next nearest neighbor coupling strength there are three different phases in this model. In a limiting case with zero next nearest neighbor coupling, which recovers the Heisenberg model on a square lattice the system is in a Neêl state with a long range antiferromagnetic order. This order survives up to a finite next nearest neighbor coupling. At an intermediate coupling strength, where the system is most frustrated we find a plaquette valence bond state. A plaquette state is a singlet consisted of four spins on the corner of a square. In our study we choose a 4×4 unit cell which is necessary to incorporate a

plaquette ordering. Indeed, the plaquette patterns can be seen clearly in our results as we draw the bond energy configuration. The plaquette phase occupies a finite region in the parameter space, which connects to the Neêl phase at the small nearest neighbor coupling side through a first order transition. The above two phases are also confirmed by other studies. However, it is the phase at large next nearest neighbor coupling strength that brings controversy. There are suggestion of a sliding Luttinger liquid[91], a fourfold degenerate long range spin order state[96, 97], and the cross dimer state[93, 94]. Our results support the fourfold degenerate state as a true ground state. We check long range spin orders by computing spin-spin correlation functions. The convergence of spin-spin correlation functions to a finite value at long distances suggests this phase has a true long range order. The cross-dimer states is also found as a meta-stable state with slightly higher energy in our calculation. However, due to the limited virtual dimension used in the calculation we could not rule out the possibility of a sliding Luttinger liquid state as a true ground state.

Ultracold polar molecules and dipolar atoms are also interesting topics in quantum simulation. We have demonstrated the anisotropic nature of dipole-dipole interaction can be used to stablize interesting charge density wave and supersolid phases. We propose to prepare the systems such that the bosonic atoms or molecules have attractive interaction in one direction and repulsive interaction in the other direction in a two dimensional square lattice. This is done by first preparing a Mott insulator with all the dipoles pointing along the direction perpendicular to the plane. Through adiabatically tuning the direction of the external field to be aligned in one lattice axis we have strong attractive interaction in this direction while the repulsive interaction remains in the other. The stability of the system is ensured due to strong interaction and dissipation blockade mechanism, which allows us to effectively write down

an extended hard-core Bose-Hubbard model in a square lattice. We have shown that at half-filling there is a large region of the charge density wave state with a stripe order. Away from half-filling the stripe charge density wave is surrounded by a supersolid phase where on top of the stripe charge density pattern we observe a nonzero superfluid order. The mechanism of this supersolid phase is different from those found with the soft-core bosons where a supersolid appears only at particle doping. The superfluid phase is connected to the supersolid on both small and large chemical potential sides. With a stronger attractive interaction the stripe phase gets larger while the region of supersolid phase will shrink if we increase or decrease the attractive interaction strength away from its optimal value roughly around the hopping energy $-t$. If interaction on both directions is positive we have a checkerboard charge density wave instead of a stripe one. We found no supersolid in this case, which is consistent with former Quantum Monte Carlo studies.

We have shown that it is possible to study a spin liquid phase in the cold atom system. We suggest from numerical evidences that a spin liquid is reachable through simulating a J_1-J_2 XY model. A J_1-J_2 XY model is equivalent to a system with hard-core bosons with both nearest and next nearest neighbor hopping in the square lattice. We choose to use spin dependent optical lattices and Raman laser beams to implement a system with a next nearest hopping comparable to the nearest one. A similar scheme which is used to induce magnetic field in the cold atom systems has been demonstrated in the experiment recently. We calculate the phase diagram of the J_1-J_2 XY model by two complementary methods: the iPEPS tensor network algorithm and the ED method. The phase diagram at large J_1/J_2 and at large J_2/J_1 can be understood from the limit cases. With only nearest neighbor hopping J_1 the system has a Neêl ordering while it has a stripe spin order at only next nearest

neighbor hopping J_2. Both phases extend over a finite region if we turn on a finite J_2 or J_1 from the limit case respectively. This is confirmed in the ED and the iPEPS calculation by computing the spin-spin correlations and the corresponding structure factors. Both show evidence of the Neêl order(the stripe order) at small(large) J_2/J_1. Around the most frustrated point $J_2/J_1 = 0.5$ there is a region without any spin orders. The intermediate region found here has properties similar to those observed in a spin liquid phase in the J_1-J_2 Heisenberg model[104]. We check the possibility of a dimer valence bond solid and a plaquette valence bond solid by computing the structure factors with the ED method and the long range dimer-dimer correlation function with the iPEPS method. Although both orders show peaks in the corresponding structure factors in the region of intermediate coupling strength with the ED method they vanish after extrapolations. Therefore we suggest it is a finite size effect. Furthermore, in the iPEPS calculation the dimer-dimer correlations always decay exponentially, which excludes the possibility of a valence bond order here. The spin ordered phases can be observed in the time of flight image while the spin liquid phase can be observed in the harmonic trap as a plateau due to its finite triplet spin gap.

We have demonstrated that the iPEPS method is able to capture the ground state property of a Heisenberg type model with $SO(5)$ symmetry. Following the success in the observation of an $SU(6)$ Mott insulator[6] a class of high symmetry spin model might be able to be reached in the cold atom experiment in the future. We suggest in this particular model there are a Nêel phase, a magnetic dimer phase, and a non-magnetic dimer phase. The existence of a Nêel phase and a magnetic dimer agrees with several earlier studies. However, the dimer phase without magnetic ordering has not yet been reported. In this region people suspect a plaquette valence bond phase

from an earlier ED calculation but we do not find supportive evidences of it in our results. We confirm in this phase that the dimer orders persists after extrapolation of the virtual dimension D and the dimer-dimer correlations take finite values in the long range limit.

Finally, we have shown that a topological phase could be realized in a 1D optical superlattice. We find repulsively interacting bosons with fractional fillings can carry a nonzero Chern number and edge states. Furthermore, their Chern number can be measured from the density profiles in the harmonic trap. The simple structure of this model makes it a promising candidate to experimental implementation.

8.2 Outlook

As novel manipulation schemes become accessible in the cold atom experiments it is interesting to consider how we can use them to construct new systems and to study important physics there. Several state-of-art advances in experiments have been made in recent years: light assisted spin-orbital coupling, quantum degenerate gas of dipolar atoms, polar molecules, orbital condensates, and high symmetry group fermions. Some of these are unique to cold atoms and thus have no correspondent systems in the condensed matter. It provides great opportunity to explore systems which are not considered before.

Numerical input on these studies could provide some guides to understand their physics. Our tensor network methods in general can be applied to study these systems when confined in the optical lattices. Since the cold atom experiments are performed in finite temperature a future direction is to consider finite temperature effect on our calculation. Although we expect at low enough temperature which is comparable to the energy scale in the system our calculation might still be able to capture

the important physics there. It is still interesting to discuss the transition in the temperature axis.

Another important issue is to improve the accuracy of the calculation of the ground state properties. Since the main error is from the finite virtual dimension D it is crucial to include a larger D in the calculation. Two different approaches have been considered: tensors with symmetry structure and Monte Carlo sampling in tensor network contraction. We expect that by incorporating symmetry into our tensor network method we could even study systems with more complicated entanglement structure.

To sum up we expect the work presented in this dissertation will provide guides in searching for novel quantum phases in cold atom systems and trigger more development of tensor network algorithms.

APPENDIX

APPENDIX A

Exact Diagonalization

In this appendix we outline our implementation of the exact diagonalization method used in Chapter V. For $S = 1/2$ systems it is convenient to store a basis vector by first converting its spin configuration into a sequence of binary numbers, namely by setting $|\uparrow\rangle = 1$ and $|\downarrow\rangle = 0$ then converting it into a decimal number. Any operator can then be stored as a $2^n \times 2^n$ matrix with system size n, which is constructed by applying the operator on all the basis states. However, for the largest cluster we studied here($n = 32$) there are about 4.3 billion states, which makes it impossible to store the whole Hamiltonian in this basis. A standard procedure around this difficulty is to consider a symmetrized basis.[185, 186] In our implementation we choose a set of symmetry group including:

1. Translational symmetry.

2. Reflection symmetry on x, y axis and on $(1, 1)$ direction if a state has the same eigenvalue of x and y reflection.

3. We limit our study to the $\sum_{i=1}^{n} S_i^z = 0$ case.

4. Spin inversion symmetry Iv: $Iv|\uparrow\rangle = |\downarrow\rangle$.

, which reduce the number of basis states to about 2.4 million. The most time-consuming part is to go through all 4.3 billion states to find out the representative states. This step requires the computer to apply above symmetry group operations on every state. Since applying operations on different states can be done independently from each other we can divide the whole basis searching work into smaller pieces and assign them to a modern multi-core machine. The speedup is directly proportional to the number of cores available at hand.

Once the symmetrized basis is constructed the next step is to calculate the Hamiltonian matrix. This is done by applying Hamiltonian to each symmetrized basis state. A basis state after the action of Hamiltonian will generally no longer remains in the basis. Thus the same set of symmetry operations is performed to find the corresponding representative state. The index of the representative state in the basis is then found by a binary search.

For a system with local interactions the Hamiltonian matrix is often sparse. We can adopt the large scale sparse matrix eigenvalue solver to find the low lying states of the system. For example the Lanczos algorithm is a standard method used in the implementation of the ED method. In our implementation we use the *eigs* function defined in MATLAB.

We perform the measurement of correlation functions by first constructing the corresponding operators in the symmetrized basis. The procedure is exactly the same as calculating the Hamiltonian matrix. The expectation value is computed by simple multiplication of these operator matrices and the ground state vector.

Another issue regards the choice of system sizes and geometry. There are several possible clusters which can cover the square lattice periodically such as N=8, 10, 16, 18, 20, 26, 32, 34, ... However, due to different geometry of these clusters not every

of them has all the crystal momentum which are important to candidate ground states. For this reason in order to study the transition of Neél phase or the stripe phase to a different phase we are limited to choose clusters with N=16, 20, and 32.

BIBLIOGRAPHY

BIBLIOGRAPHY

[1] RichardP. Feynman. Simulating physics with computers. 21(6-7):467–488–, 1982.

[2] Markus Greiner, Olaf Mandel, Tilman Esslinger, Theodor W. Hansch, and Immanuel Bloch. Quantum phase transition from a superfluid to a mott insulator in a gas of ultracold atoms. *Nature*, 415(6867):39–44, January 2002.

[3] P. Soltan-Panahi, J. Struck, P. Hauke, A. Bick, W. Plenkers, G. Meineke, C. Becker, P. Windpassinger, M. Lewenstein, and K. Sengstock. Multi-component quantum gases in spin-dependent hexagonal lattices. *Nat Phys*, 7(5):434–440, May 2011.

[4] Robert Jordens, Niels Strohmaier, Kenneth Gunter, Henning Moritz, and Tilman Esslinger. A mott insulator of fermionic atoms in an optical lattice. *Nature*, 455(7210):204–207, September 2008.

[5] U. Schneider, L. HackermÃijller, S. Will, Th. Best, I. Bloch, T. A. Costi, R. W. Helmes, D. Rasch, and A. Rosch. Metallic and insulating phases of repulsively interacting fermions in a 3d optical lattice. *Science*, 322(5907):1520–1525, 2008.

[6] Shintaro Taie, Rekishu Yamazaki, Seiji Sugawa, and Yoshiro Takahashi. An su(6) mott insulator of an atomic fermi gas realized by large-spin pomeranchuk cooling. *Nat Phys*, 8(11):825–830, November 2012.

[7] Seiji Sugawa, Kensuke Inaba, Shintaro Taie, Rekishu Yamazaki, Makoto Yamashita, and Yoshiro Takahashi. Interaction and filling-induced quantum phases of dual mott insulators of bosons and fermions. *Nat Phys*, 7(8):642–648, August 2011.

[8] Jonathan Simon, Waseem S. Bakr, Ruichao Ma, M. Eric Tai, Philipp M. Preiss, and Markus Greiner. Quantum simulation of antiferromagnetic spin chains in an optical lattice. *Nature*, 472(7343):307–312, April 2011.

[9] Y.-J. Lin, R. L. Compton, K. Jimenez-Garcia, J. V. Porto, and I. B. Spielman. Synthetic magnetic fields for ultracold neutral atoms. *Nature*, 462(7273):628–632, December 2009.

[10] M. Aidelsburger, M. Atala, S. Nascimbène, S. Trotzky, Y.-A. Chen, and I. Bloch. Experimental realization of strong effective magnetic fields in an optical lattice. *Phys. Rev. Lett.*, 107:255301, Dec 2011.

[11] Amodsen Chotia, Brian Neyenhuis, Steven A. Moses, Bo Yan, Jacob P. Covey, Michael Foss-Feig, Ana Maria Rey, Deborah S. Jin, and Jun Ye. Long-lived dipolar molecules and feshbach molecules in a 3d optical lattice. *Phys. Rev. Lett.*, 108:080405, Feb 2012.

[12] Georg Wirth, Matthias Olschlager, and Andreas Hemmerich. Evidence for orbital superfluidity in the p-band of a bipartite optical square lattice. *Nat Phys*, 7(2):147–153, February 2011.

[13] Parvis Soltan-Panahi, Dirk-Soren Luhmann, Julian Struck, Patrick Windpassinger, and Klaus Sengstock. Quantum phase transition to unconventional multi-orbital superfluidity in optical lattices. *Nat Phys*, 8(1):71–75, January 2012.

[14] Stefan Wessel and Matthias Troyer. Supersolid hard-core bosons on the triangular lattice. *Phys. Rev. Lett.*, 95:127205, Sep 2005.

[15] S. Raghu, Xiao-Liang Qi, C. Honerkamp, and Shou-Cheng Zhang. Topological mott insulators. *Phys. Rev. Lett.*, 100:156401, Apr 2008.

[16] N. Y. Yao, C. R. Laumann, A. V. Gorshkov, S. D. Bennett, E. Demler, P. Zoller, and M. D. Lukin. Topological flat bands from dipolar spin systems. *Phys. Rev. Lett.*, 109:266804, Dec 2012.

[17] S. R. White. *Phys. Rev. B*, 48:10345, 1993.

[18] Ulrich SchollwÃűck. The density-matrix renormalization group in the age of matrix product states. *Annals of Physics*, 326(1):96–192, January 2011.

[19] Immanuel Bloch, Jean Dalibard, and Wilhelm Zwerger. Many-body physics with ultracold gases. *Rev. Mod. Phys.*, 80:885–964, Jul 2008.

[20] Rudolf Grimm, Matthias WeidemÃijller, and Yurii B. Ovchinnikov. Optical dipole traps for neutral atoms. volume Volume 42, pages 95–170. Academic Press, 2000.

[21] Jason P. Kestner. *Effective single-band Hamiltonians for stronly interacting ulatracold fermions in a optical lattice.* PhD thesis, University of Michigan, 2009.

[22] Paul R. Berman and Vladimir S. Malinovsky. *Principles of Laser Spectroscopy and Quantum Optics.* Princeton University Press, 2010.

[23] D Jaksch and P Zoller. Creation of effective magnetic fields in optical lattices: the hofstadter butterfly for cold neutral. *New Journal of Physics*, 5(1):56–, 2003.

[24] Fabrice Gerbier and Jean Dalibard. Gauge fields for ultracold atoms in optical superlattices. *New Journal of Physics*, 12(3):033007–, 2010.

[25] Neil W. Ashcroft and N. David Mermin. *Solid State Physics*. 1976.

[26] W. Kohn. Analytic properties of bloch waves and wannier functions. *Phys. Rev.*, 115:809–821, Aug 1959.

[27] Andrew John Daley. *Manipulation and simulation of cold atoms in optical lattices*. PhD thesis, University of Innsbruck, 2005.

[28] D. Jaksch, C. Bruder, J. I. Cirac, C. W. Gardiner, and P. Zoller. Cold bosonic atoms in optical lattices. *Phys. Rev. Lett.*, 81:3108–3111, Oct 1998.

[29] E. Gull and A. J. Millis. Energetics of superconductivity in the two-dimensional hubbard model. *Phys. Rev. B*, 86:241106, Dec 2012.

[30] Alexander Altland and Ben Simons. *Condensed Matter Field Theory*. 2006.

[31] Leon Balents. Spin liquids in frustrated magnets. *Nature*, 464(7286):199–208, March 2010.

[32] B J Powell and Ross H McKenzie. Quantum frustration in organic mott insulators: from spin liquids to unconventional superconductors. *Reports on Progress in Physics*, 74(5):056501, 2011.

[33] Minoru Yamashita, Norihito Nakata, Yoshinori Senshu, Masaki Nagata, Hiroshi M. Yamamoto, Reizo Kato, Takasada Shibauchi, and Yuji Matsuda. Highly mobile gapless excitations in a two-dimensional candidate quantum spin liquid. *Science*, 328(5983):1246–1248, 2010.

[34] S. R. White. *Phys. Rev. Lett.*, 69:2863, 1992.

[35] Guifré Vidal. Efficient classical simulation of slightly entangled quantum computations. *Phys. Rev. Lett.*, 91:147902, Oct 2003.

[36] Guifré Vidal. Efficient simulation of one-dimensional quantum many-body systems. *Phys. Rev. Lett.*, 93:040502, Jul 2004.

[37] A J Daley, C Kollath, U SchollwÃűck, and G Vidal. Time-dependent density-matrix renormalization-group using adaptive effective hilbert spaces. *Journal of Statistical Mechanics: Theory and Experiment*, 2004(04):P04005, 2004.

[38] G. Vidal. Classical simulation of infinite-size quantum lattice systems in one spatial dimension. *Phys. Rev. Lett.*, 98:070201, Feb 2007.

[39] F. Verstraete, M. M. Wolf, D. Perez-Garcia, and J. I. Cirac. Criticality, the area law, and the computational power of projected entangled pair states. *Phys. Rev. Lett.*, 96:220601, Jun 2006.

[40] Philippe Corboz, Jacob Jordan, and Guifré Vidal. Simulation of fermionic lattice models in two dimensions with projected entangled-pair states: Next-nearest neighbor hamiltonians. *Phys. Rev. B*, 82:245119, Dec 2010.

[41] Philippe Corboz, Román Orús, Bela Bauer, and Guifré Vidal. Simulation of strongly correlated fermions in two spatial dimensions with fermionic projected entangled-pair states. *Phys. Rev. B*, 81:165104, Apr 2010.

[42] Marc Cheneau, Peter Barmettler, Dario Poletti, Manuel Endres, Peter Schausz, Takeshi Fukuhara, Christian Gross, Immanuel Bloch, Corinna Kollath, and Stefan Kuhr. Light-cone-like spreading of correlations in a quantum many-body system. *Nature*, 481(7382):484–487, January 2012.

[43] Philippe Corboz, Andreas M. Läuchli, Karlo Penc, Matthias Troyer, and Frédéric Mila. Simultaneous dimerization and su(4) symmetry breaking of 4-color fermions on the square lattice. *Phys. Rev. Lett.*, 107:215301, Nov 2011.

[44] J. Jordan, R. Orús, G. Vidal, F. Verstraete, and J. I. Cirac. Classical simulation of infinite-size quantum lattice systems in two spatial dimensions. *Phys. Rev. Lett.*, 101:250602, Dec 2008.

[45] Tomotoshi Nishino and Kouichi Okunishi. Corner transfer matrix renormalization group method. *Journal of the Physical Society of Japan*, 65(4):891–894, 1996.

[46] Román Orús and Guifré Vidal. Simulation of two-dimensional quantum systems on an infinite lattice revisited: Corner transfer matrix for tensor contraction. *Phys. Rev. B*, 80:094403, Sep 2009.

[47] Y.-J. Han, Y.-H. Chan, W. Yi, A. J. Daley, S. Diehl, P. Zoller, and L.-M. Duan. Stabilization of the p-wave superfluid state in an optical lattice. *Phys. Rev. Lett.*, 103:070404, Aug 2009.

[48] Y.-H. Chan, Y.-J. Han, and L.-M. Duan. Supersolid and charge-density-wave states from anisotropic interaction in an optical lattice. *Phys. Rev. A*, 82:053607, Nov 2010.

[49] Y.-H. Chan, Y.-J. Han, and L.-M. Duan. Tensor network simulation of the phase diagram of the frustrated J_1-J_2 heisenberg model on a checkerboard lattice. *Phys. Rev. B*, 84:224407, Dec 2011.

[50] Y-H Chan and L-M Duan. Evidence of a spin liquid with hard-core bosons in a square lattice. *New Journal of Physics*, 14(11):113039, 2012.

[51] Shi-Liang Zhu, Z. D. Wang, Y. H. Chan, and L. M. Duan. Topological bose-mott insulators in one-dimensional optical superlattices.

[52] C. A. Regal, M. Greiner, and D. S. Jin. Observation of resonance condensation of fermionic atom pairs. *Phys. Rev. Lett.*, 92:040403, Jan 2004.

[53] M. W. Zwierlein, J. R. Abo-Shaeer, A. Schirotzek, C. H. Schunck, and W. Ketterle. Vortices and superfluidity in a strongly interacting fermi gas. *Nature*, 435(7045):1047–1051, June 2005.

[54] A. Altmeyer S. Riedl S. Jochim J. Hecker Denschlag C. Chin, M. Bartenstein and R. Grimm. Observation of the pairing gap in a strongly interacting fermi gas. *Science*, 305:1128, 2004.

[55] Joseph Kinast, Andrey Turlapov, John E. Thomas, Qijin Chen, Jelena Stajic, and Kathryn Levin. Heat capacity of a strongly interacting fermi gas. *Science*, 307(5713):1296–1299, 2005.

[56] M. W. Zwierlein, C. A. Stan, C. H. Schunck, S. M. F. Raupach, A. J. Kerman, and W. Ketterle. Condensation of pairs of fermionic atoms near a feshbach resonance. *Phys. Rev. Lett.*, 92:120403, Mar 2004.

[57] J. P. Gaebler, J. T. Stewart, J. L. Bohn, and D. S. Jin. p-wave feshbach molecules. *Phys. Rev. Lett.*, 98:200403, May 2007.

[58] J. Zhang, E. G. M. van Kempen, T. Bourdel, L. Khaykovich, J. Cubizolles, F. Chevy, M. Teichmann, L. Tarruell, S. J. J. M. F. Kokkelmans, and C. Salomon. p-wave feshbach resonances of ultracold ^{6}Li. *Phys. Rev. A*, 70:030702, Sep 2004.

[59] J. Fuchs, C. Ticknor, P. Dyke, G. Veeravalli, E. Kuhnle, W. Rowlands, P. Hannaford, and C. J. Vale. Binding energies of ^{6}Li p-wave feshbach molecules. *Phys. Rev. A*, 77:053616, May 2008.

[60] Yasuhisa Inada, Munekazu Horikoshi, Shuta Nakajima, Makoto Kuwata-Gonokami, Masahito Ueda, and Takashi Mukaiyama. Collisional properties of p-wave feshbach molecules. *Phys. Rev. Lett.*, 101:100401, Sep 2008.

[61] V. Gurarie, L. Radzihovsky, and A. V. Andreev. Quantum phase transitions across a p-wave feshbach resonance. *Phys. Rev. Lett.*, 94:230403, Jun 2005.

[62] S. S. Botelho and C. A. R. SÃą de Melo. Quantum phase transition in the bcs-to-bec evolution of <i>p</i>-wave fermi gases. *Journal of Low Temperature Physics*, 140:409–428, 2005. 10.1007/s10909-005-7324-3.

[63] Tin-Lun Ho and Roberto B. Diener. Fermion superfluids of nonzero orbital angular momentum near resonance. *Phys. Rev. Lett.*, 94:090402, Mar 2005.

[64] Chi-Ho Cheng and S.-K. Yip. Anisotropic fermi superfluid via p-wave feshbach resonance. *Phys. Rev. Lett.*, 95:070404, Aug 2005.

[65] M. Jona-Lasinio, L. Pricoupenko, and Y. Castin. Three fully polarized fermions close to a p-wave feshbach resonance. *Phys. Rev. A*, 77:043611, Apr 2008.

[66] J. Levinsen, N. R. Cooper, and V. Gurarie. Stability of fermionic gases close to a p-wave feshbach resonance. *Phys. Rev. A*, 78:063616, Dec 2008.

[67] N. Syassen, D. M. Bauer, M. Lettner, T. Volz, D. Dietze, J. J. GarcÃŋa-Ripoll, J. I. Cirac, G. Rempe, and S. DÃijrr. Strong dissipation inhibits losses and induces correlations in cold molecular gases. *Science*, 320(5881):1329–1331, 2008.

[68] J J Garcia-Ripoll, S Durr, N Syassen, D M Bauer, M Lettner, G Rempe, and J I Cirac. Dissipation-induced hard-core boson gas in an optical lattice. *New Journal of Physics*, 11(1):013053, 2009.

[69] A. J. Daley, J. M. Taylor, S. Diehl, M. Baranov, and P. Zoller. Atomic three-body loss as a dynamical three-body interaction. *Phys. Rev. Lett.*, 102:040402, Jan 2009.

[70] S.-K. Yip. Energy levels of two identical fermions in a harmonic trap near a p-wave feshbach resonance. *Phys. Rev. A*, 78:013612, Jul 2008.

[71] L.-M. Duan. Effective hamiltonian for fermions in an optical lattice across a feshbach resonance. *Phys. Rev. Lett.*, 95:243202, Dec 2005.

[72] L.-M. Duan. General hubbard model for strongly interacting fermions in an optical lattice and its phase detection. *EPL (Europhysics Letters)*, 81(2):20001, 2008.

[73] J. P. Kestner and L.-M. Duan. Level crossing in the three-body problem for strongly interacting fermions in a harmonic trap. *Phys. Rev. A*, 76:033611, Sep 2007.

[74] S. A. Kivelson E. W. Carlson, V. J. Emery and D. Orgad. *The Physics of Superconductors*. Springer, 2003.

[75] U. Schollwöck. The density-matrix renormalization group. *Rev. Mod. Phys.*, 77:259–315, Apr 2005.

[76] B Wang and L-M Duan. Superfluidity of fermions with repulsive on-site interaction in an anisotropic optical lattice near a feshbach resonance. *New Journal of Physics*, 10(7):073007, 2008.

[77] M. Roncaglia, M. Rizzi, and J. I. Cirac. Pfaffian state generation by strong three-body dissipation. *Phys. Rev. Lett.*, 104:096803, Mar 2010.

[78] K.-K. Ni, S. Ospelkaus, M. H. G. de Miranda, A. Pe'er, B. Neyenhuis, J. J. Zirbel, S. Kotochigova, P. S. Julienne, D. S. Jin, and J. Ye. A high phase-space-density gas of polar molecules. *Science*, 322(5899):231–235, October 2008.

[79] K.-K. Ni, S. Ospelkaus, D. Wang, G. Quemener, B. Neyenhuis, M. H. G. de Miranda, J. L. Bohn, J. Ye, and D. S. Jin. Dipolar collisions of polar molecules in the quantum regime. *Nature*, 464(7293):1324–1328, April 2010.

[80] T. Koch, T. Lahaye, J. Metz, B. Frohlich, A. Griesmaier, and T. Pfau. Stabilization of a purely dipolar quantum gas against collapse. *Nat Phys*, 4(3):218–222, March 2008.

[81] Mingwu Lu, Seo Ho Youn, and Benjamin L. Lev. Trapping ultracold dysprosium: A highly magnetic gas for dipolar physics. *Phys. Rev. Lett.*, 104:063001, Feb 2010.

[82] E. Kim and M. H. W. Chan. Probable observation of a supersolid helium phase. *Nature*, 427(6971):225–227, January 2004.

[83] Pinaki Sengupta, Leonid P. Pryadko, Fabien Alet, Matthias Troyer, and Guido Schmid. Supersolids versus phase separation in two-dimensional lattice bosons. *Phys. Rev. Lett.*, 94:207202, May 2005.

[84] G. G. Batrouni and R. T. Scalettar. Phase separation in supersolids. *Phys. Rev. Lett.*, 84:1599–1602, Feb 2000.

[85] F. Hébert, G. G. Batrouni, R. T. Scalettar, G. Schmid, M. Troyer, and A. Dorneich. Quantum phase transitions in the two-dimensional hardcore boson model. *Phys. Rev. B*, 65:014513, Dec 2001.

[86] B. Capogrosso-Sansone, C. Trefzger, M. Lewenstein, P. Zoller, and G. Pupillo. Quantum phases of cold polar molecules in 2d optical lattices. *Phys. Rev. Lett.*, 104:125301, Mar 2010.

[87] Ippei Danshita and Carlos A. R. Sá de Melo. Stability of superfluid and supersolid phases of dipolar bosons in optical lattices. *Phys. Rev. Lett.*, 103:225301, Nov 2009.

[88] S. Yi, T. Li, and C. P. Sun. Novel quantum phases of dipolar bose gases in optical lattices. *Phys. Rev. Lett.*, 98:260405, Jun 2007.

[89] Jacob Jordan, Román Orús, and Guifré Vidal. Numerical study of the hardcore bose-hubbard model on an infinite square lattice. *Phys. Rev. B*, 79:174515, May 2009.

[90] B Bauer, G Vidal, and M Troyer. Assessing the accuracy of projected entangled-pair states on infinite lattices. *Journal of Statistical Mechanics: Theory and Experiment*, 2009(09):P09006–, 2009.

[91] P. Sindzingre, J.-B. Fouet, and C. Lhuillier. One-dimensional behavior and sliding luttinger liquid phase in a frustrated spin-$\frac{1}{2}$ crossed chain model: Contribution of exact diagonalizations. *Phys. Rev. B*, 66:174424, Nov 2002.

[92] Oleg A. Starykh, Rajiv R. P. Singh, and Gregory C. Levine. Spinons in a crossed-chains model of a 2d spin liquid. *Phys. Rev. Lett.*, 88:167203, Apr 2002.

[93] Oleg A. Starykh, Akira Furusaki, and Leon Balents. Anisotropic pyrochlores and the global phase diagram of the checkerboard antiferromagnet. *Phys. Rev. B*, 72:094416, Sep 2005.

[94] S. Moukouri. Néel and valence-bond crystal phases of frustrated two-dimensional heisenberg models. *Phys. Rev. B*, 77:052408, Feb 2008.

[95] Wolfram Brenig and Matthias Grzeschik. Valence-bond crystal phase of the crossed-chain quantum spin model. *Phys. Rev. B*, 69:064420, Feb 2004.

[96] O. Tchernyshyov, O. A. Starykh, R. Moessner, and A. G. Abanov. Bond order from disorder in the planar pyrochlore magnet. *Phys. Rev. B*, 68:144422, Oct 2003.

[97] Jean-Sébastien Bernier, Chung-Hou Chung, Yong Baek Kim, and Subir Sachdev. Planar pyrochlore antiferromagnet: A large-n analysis. *Phys. Rev. B*, 69:214427, Jun 2004.

[98] V. Murg, F. Verstraete, and J. I. Cirac. Exploring frustrated spin systems using projected entangled pair states. *Phys. Rev. B*, 79:195119, May 2009.

[99] G. Evenbly and G. Vidal. Frustrated antiferromagnets with entanglement renormalization: Ground state of the spin-$\frac{1}{2}$ heisenberg model on a kagome lattice. *Phys. Rev. Lett.*, 104:187203, May 2010.

[100] J.-B. Fouet, M. Mambrini, P. Sindzingre, and C. Lhuillier. Planar pyrochlore: A valence-bond crystal. *Phys. Rev. B*, 67:054411, Feb 2003.

[101] Subir Sachdev and Kwon Park. Ground states of quantum antiferromagnets in two dimensions. *Annals of Physics*, 298(1):58–122, May 2002.

[102] Z. Y. Meng, T. C. Lang, S. Wessel, F. F. Assaad, and A. Muramatsu. Quantum spin liquid emerging in two-dimensional correlated dirac fermions. *Nature*, 464(7290):847–851, April 2010.

[103] Simeng Yan, David A. Huse, and Steven R. White. Spin-liquid ground state of the s = 1/2 kagome heisenberg antiferromagnet. *Science*, 332(6034):1173–1176, June 2011.

[104] Hong-Chen Jiang, Hong Yao, and Leon Balents. Spin liquid ground state of the spin-$\frac{1}{2}$ square J_1-J_2 heisenberg model. *Phys. Rev. B*, 86:024424, Jul 2012.

[105] X-G. Wen L. Wang, Z.-C. Gu and F. Verstraete. Spin-liquid phase in spin-1/2 square j_1-j_2 heisenberg model: A tensor product state approach. 2011.

[106] Fabio Mezzacapo. Ground-state phase diagram of the quantum $J_1 - J_2$ model on the square lattice. *Phys. Rev. B*, 86:045115, Jul 2012.

[107] Christopher N. Varney, Kai Sun, Victor Galitski, and Marcos Rigol. Kaleidoscope of exotic quantum phases in a frustrated xy model. *Phys. Rev. Lett.*, 107:077201, Aug 2011.

[108] D. Jaksch and P. Zoller. The cold atom hubbard toolbox. *Annals of Physics*, 315(1):52–79, January 2005.

[109] L.-M. Duan, E. Demler, and M. D. Lukin. Controlling spin exchange interactions of ultracold atoms in optical lattices. *Phys. Rev. Lett.*, 91:090402, Aug 2003.

[110] J. Struck, C. Ã-lschlÃď ger, R. Le Targat, P. Soltan-Panahi, A. Eckardt, M. Lewenstein, P. Windpassinger, and K. Sengstock. Quantum simulation of frustrated classical magnetism in triangular optical lattices. *Science*, 333(6045):996–999, August 2011.

[111] S. Folling, S. Trotzky, P. Cheinet, M. Feld, R. Saers, A. Widera, T. Muller, and I. Bloch. Direct observation of second-order atom tunnelling. *Nature*, 448(7157):1029–1032, August 2007.

[112] F. Verstraete, V. Murg, and J.I. Cirac. Matrix product states, projected entangled pair states, and variational renormalization group methods for quantum spin systems. *Advances in Physics*, 57(2):143–224, March 2008.

[113] H. C. Jiang, Z. Y. Weng, and T. Xiang. Accurate determination of tensor network state of quantum lattice models in two dimensions. *Phys. Rev. Lett.*, 101:090603, Aug 2008.

[114] H.J. Schulz, T.A.L. Ziman, and D. Poilblanc. Magnetic order and disorder in the frustrated quantum heisenberg antiferromagnet in two dimensions. *J. Phys. I France*, 6(5):675–703, May 1996.

[115] Luca Capriotti, Federico Becca, Alberto Parola, and Sandro Sorella. Suppression of dimer correlations in the two-dimensional $J_1 - J_2$ heisenberg model: An exact diagonalization study. *Phys. Rev. B*, 67:212402, Jun 2003.

[116] E. Alba, X. Fernandez-Gonzalvo, J. Mur-Petit, J. K. Pachos, and J. J. Garcia-Ripoll. Seeing topological order in time-of-flight measurements. *Phys. Rev. Lett.*, 107:235301, Nov 2011.

[117] Olaf Mandel, Markus Greiner, Artur Widera, Tim Rom, Theodor W. Hansch, and Immanuel Bloch. Controlled collisions for multi-particle entanglement of optically trapped atoms. *Nature*, 425(6961):937–940, October 2003.

[118] K. Xu, Y. Liu, J. R. Abo-Shaeer, T. Mukaiyama, J. K. Chin, D. E. Miller, W. Ketterle, Kevin M. Jones, and Eite Tiesinga. Sodium bose-einstein condensates in an optical lattice. *Phys. Rev. A*, 72:043604, Oct 2005.

[119] N. Read and S. Sachdev. Spin-peierls, valence-bond solid, and nÃĺel ground states of low-dimensional quantum antiferromagnets. *Phys. Rev. B*, 42:4568, 1990.

[120] N. Read and Subir Sachdev. Large- N expansion for frustrated quantum antiferromagnets. *Phys. Rev. Lett.*, 66:1773–1776, Apr 1991.

[121] D. P. Arovas and A. Auerbach. Functional integral theories of low-dimensional quantum heisenberg models. *Phys. Rev. B*, 38(1):316–332, Jul 1988.

[122] I Affleck and J. B. Marston. Large-n limit of the heisenberg-hubbard model: Implications for high-t_c superconductors. *Phys. Rev. B*, 37(7):3774–3777, Mar 1988.

[123] K. Harada, N. Kawashima, and M. Troyer. NÃĺel and spin-peierls ground states of two-dimensional su(n) quantum antiferromagnets. *Phys. Rev. Lett.*, 90:117203, 2003.

[124] Michael Hermele, T. Senthil, Matthew P. A. Fisher, Patrick A. Lee, Naoto Nagaosa, and Xiao-Gang Wen. Stability of $u(1)$ spin liquids in two dimensions. *Phys. Rev. B*, 70:214437, Dec 2004.

[125] Naoki Kawashima and Yuta Tanabe. Ground states of the SU(n) heisenberg model. *Phys. Rev. Lett.*, 98:057202, Jan 2007.

[126] Martin Greiter and Stephan Rachel. Valence bond solids for SU(n) spin chains: Exact models, spinon confinement, and the haldane gap. *Phys. Rev. B*, 75:184441, May 2007.

[127] Jie Lou, Anders W. Sandvik, and Naoki Kawashima. Antiferromagnetic to valence-bond-solid transitions in two-dimensional SU(n) heisenberg models with multispin interactions. *Phys. Rev. B*, 80:180414, Nov 2009.

[128] Zi Cai, Hsiang-Hsuan Hung, Lei Wang, Dong Zheng, and Congjun Wu. arXiv:1202.6323.

[129] Zi Cai, Hsiang-Hsuan Hung, Lei Wang, Yi Li, and Congjun Wu. arXiv:1207.6843.

[130] Lars Bonnes, Kaden R. A. Hazzard, Salvatore R. Manmana, Ana Maria Rey, and Stefan Wessel. arXiv:1207.3900.

[131] Salvatore R. Manmana, Kaden R. A. Hazzard, Gang Chen, Adrian E. Feiguin, and Ana Maria Rey. Su(n) magnetism in chains of ultracold alkaline-earth-metal atoms: Mott transitions and quantum correlations. *Phys. Rev. A*, 84:043601, Oct 2011.

[132] K. I. Kugel' and D. I. Khomskii. *Usp. Fiz. Nauk*, 136:631, 1982.

[133] Y. Yamashita, N. Shibata, and K. Ueda. Su(4) spin-orbit critical state in one dimension. *Phys. Rev. B*, 58:9114, 1998.

[134] Y. Q. Li, Michael Ma, D. N. Shi, and F. C. Zhang. Su(4) theory for spin systems with orbital degeneracy. *Phys. Rev. Lett.*, 81:3527, 1998.

[135] L. Guidoni, G. Santoro, S. Sorella, A. Parola, and E. Tosatti. Spin gap in low-dimensional mott insulators with orbital degeneracy. *J. Appl. Phys.*, 85:5327, 1999.

[136] P. Azaria, A. O. Gogolin, P. Lecheminant, and A. A. Nersesyan. One-dimensional su(4) spin-orbital model: A low-energy effective theory. *Phys. Rev. Lett.*, 83:624, 1999.

[137] Mathias van den Bossche, Patrick Azaria, Philippe Lecheminant, and FrÍędÍęric Mila. Spontaneous plaquette formation in the su(4) spin-orbital ladder. *Phys. Rev. Lett.*, 86:4124, 2001.

[138] M. V. D. Bossche, F. C. Zhang, and F. Mila. Plaquette ground state in the two-dimensional su(4) spin-orbital model. *Eur. Phys. J. B*, 17:367, 2000.

[139] G. M. Zhang and S. Q. Shen. Ordered valence-bond states in symmetric two-dimensional spin-orbital systems. *Phys. Rev. Lett.*, 87:157201, 2001.

[140] C. Wu. Exotic many-body physics with large-spin fermi gases. *Physics*, 3:92, 2010.

[141] A. V. Gorshkov, M. Hermele, V. Gurarie, C. Xu, P. S. Julienne, J. Ye, P. Zoller, E. Demler, M. D. Lukin, and A. M. Rey. Two-orbital su(n) magnetism with ultracold alkaline-earth atoms. *Nature Phys.*, 6:289, 2010.

[142] M. A. Cazalilla, A. F. Ho, and M. Ueda. Ultracold gases of ytterbium: ferromagnetism and mott states in an su(6) fermi system. *New J. Phys.*, 11:103033, 2009.

[143] Shintaro Taie, Rekishu Yamazaki, Seiji Sugawa, and Yoshiro Takahashi. *ArXiv e-prints*, 2012.

[144] B. J. DeSalvo, M. Yan, P. G. Mickelson, Y. N. Martinez de Escobar, and T. C. Killian. Degenerate fermi gas of ^{87}Sr. *Phys. Rev. Lett.*, 105:030402, Jul 2010.

[145] Simon Stellmer, Rudolf Grimm, and Florian Schreck. Detection and manipulation of nuclear spin states in fermionic strontium. *Phys. Rev. A*, 84:043611, Oct 2011.

[146] Takeshi Fukuhara, Seiji Sugawa, Masahito Sugimoto, Shintaro Taie, and Yoshiro Takahashi. Mott insulator of ultracold alkaline-earth-metal-like atoms. *Phys. Rev. A*, 79:041604, Apr 2009.

[147] Shintaro Taie, Yosuke Takasu, Seiji Sugawa, Rekishu Yamazaki, Takuya Tsujimoto, Ryo Murakami, and Yoshiro Takahashi. Realization of a SU(2) $\times$ SU(6) system of fermions in a cold atomic gas. *Phys. Rev. Lett.*, 105:190401, Nov 2010.

[148] Cenke Xu and Congjun Wu. Resonating plaquette phases in large spin cold atom systems. *Phys. Rev. B*, 77:134449, 2008.

[149] Hsiang-Hsuan Hung, Yupeng Wang, and Congjun Wu. Quantum magnetism in ultracold alkali and alkaline-earth fermion systems with symplectic symmetry. *Phys. Rev. B*, 84:054406, Aug 2011.

[150] G. Santoro, S. Sorella, L. Guidoni, A. Parola, and E. Tosatti. *Phys. Rev. Lett.*, 83:3065, 1999.

[151] Michael Hermele, Victor Gurarie, and Ana Maria Rey. Mott insulators of ultracold fermionic alkaline earth atoms: Underconstrained magnetism and chiral spin liquid. *Phys. Rev. Lett.*, 103:135301, 2009.

[152] Michael Hermele and Victor Gurarie. Topological liquids and valence cluster states in two-dimensional su(n) magnets. *Phys. Rev. B*, 84:174441, Nov 2011.

[153] Cenke Xu. Liquids in multiorbital su(n) magnets made up of ultracold alkaline-earth atoms. *Phys. Rev. B*, 81:144431, 2010.

[154] C. Wu, J. P. Hu, and S. C. Zhang. Exact so(5) symmetry in the spin-3/2 fermionic system. *Phys. Rev. Lett.*, 91(18):186402, 2003.

[155] C. Wu. Competing orders in one dimensional spin 3/2 fermionic systems. *Phys. Rev. Lett.*, 95:266404, 2005.

[156] C. Wu. Hidden symmetry and quantum phases in spin-3/2 cold atomic systems. *Mod. Phys. Lett. B*, 20:1707, 2006.

[157] K. S. D. Beach, Fabien Alet, Matthieu Mambrini, and Sylvain Capponi. SU(n) heisenberg model on the square lattice: A continuous-n quantum monte carlo study. *Phys. Rev. B*, 80:184401, Nov 2009.

[158] Fa Wang and Ashvin Vishwanath. z_2 spin-orbital liquid state in the square lattice kugel-khomskii model. *Phys. Rev. B*, 80(6):064413, Aug 2009.

[159] Hsiang-Hsuan Hung. Exotic quantum magnetism and superfluidity in optical lattices. PhD thesis, University of California at San Diego, 2011.

[160] Shu Chen, Congjun Wu, Shou-Cheng Zhang, and Yupeng Wang. Exact spontaneous plaquette ground states for high-spin ladder models. *Phys. Rev. B*, 72(10):214428, 2005.

[161] F. Verstraete and J. I. Cirac. Renormalization algorithms for Quantum-Many Body Systems in two and higher dimensions. 2004.

[162] Michael Levin and Cody P. Nave. Tensor renormalization group approach to two-dimensional classical lattice models. *Phys. Rev. Lett.*, 99:120601, Sep 2007.

[163] Zheng-Cheng Gu, Michael Levin, and Xiao-Gang Wen. Tensor-entanglement renormalization group approach as a unified method for symmetry breaking and topological phase transitions. *Phys. Rev. B*, 78:205116, Nov 2008.

[164] B. Bauer, P. Corboz, R. Orús, and M. Troyer. Implementing global abelian symmetries in projected entangled-pair state algorithms. *Phys. Rev. B*, 83:125106, Mar 2011.

[165] H. H. Zhao, Z. Y. Xie, Q. N. Chen, Z. C. Wei, J. W. Cai, and T. Xiang. Renormalization of tensor-network states. *Phys. Rev. B*, 81:174411, May 2010.

[166] P. Corboz, M. Lajkĺőand A. M. L?0Ł1uchli, K. Penc, and F. Mila. Spin-orbital quantum liquid on the honeycomb lattice. *e-prints*, March 2012.

[167] M. Lewenstein, A. Sanpera, V. Ahufinger, B. Damski, A. Sen De, and U. Sen. Ultracold atomic gases in optical lattices: mimicking condensed matter physics and beyond. *Advances in Physics*, 56:243, 2007.

[168] M. Z. Hasan and C. L. Kane. *Colloquium* : Topological insulators. *Rev. Mod. Phys.*, 82:3045–3067, Nov 2010.

[169] Shi-Liang Zhu, Hao Fu, C.-J. Wu, S.-C. Zhang, and L.-M. Duan. Spin hall effects for cold atoms in a light-induced gauge potential. *Phys. Rev. Lett.*, 97:240401, Dec 2006.

[170] L. B. Shao, Shi-Liang Zhu, L. Sheng, D. Y. Xing, and Z. D. Wang. Realizing and detecting the quantum hall effect without landau levels by using ultracold atoms. *Phys. Rev. Lett.*, 101:246810, Dec 2008.

[171] R. O. Umucal ılar, Hui Zhai, and M. Ö. Oktel. Trapped fermi gases in rotating optical lattices: Realization and detection of the topological hofstadter insulator. *Phys. Rev. Lett.*, 100:070402, Feb 2008.

[172] N. Goldman, I. Satija, P. Nikolic, A. Bermudez, M. A. Martin-Delgado, M. Lewenstein, and I. B. Spielman. Realistic time-reversal invariant topological insulators with neutral atoms. *Phys. Rev. Lett.*, 105:255302, Dec 2010.

[173] Li-Jun Lang, Xiaoming Cai, and Shu Chen. Edge states and topological phases in one-dimensional optical superlattices. *Phys. Rev. Lett.*, 108:220401, May 2012.

[174] Feng Mei, Shi-Liang Zhu, Zhi-Ming Zhang, C. H. Oh, and N. Goldman. Simulating Z_2 topological insulators with cold atoms in a one-dimensional optical lattice. *Phys. Rev. A*, 85:013638, Jan 2012.

[175] D. J. Thouless, M. Kohmoto, M. P. Nightingale, and M. den Nijs. Quantized hall conductance in a two-dimensional periodic potential. *Phys. Rev. Lett.*, 49:405–408, Aug 1982.

[176] A. Bohm, A. Mostafazadeh, H. Koizumi, Q. Niu, and J. Zwanziger. *The Geometric Phase in Quantum Systems*. Springer-Verlag, Berlin, 2003.

[177] Giacomo Roati, Chiara D/'Errico, Leonardo Fallani, Marco Fattori, Chiara Fort, Matteo Zaccanti, Giovanni Modugno, Michele Modugno, and Massimo Inguscio. Anderson localization of a non-interacting bose-einstein condensate. *Nature*, 453(7197):895–898, June 2008.

[178] V. G. Rousseau, D. P. Arovas, M. Rigol, F. Hébert, G. G. Batrouni, and R. T. Scalettar. Exact study of the one-dimensional boson hubbard model with a superlattice potential. *Phys. Rev. B*, 73:174516, May 2006.

[179] J M Zhang and R X Dong. Exact diagonalization: the boseâĂŞhubbard model as an example. *European Journal of Physics*, 31(3):591, 2010.

[180] Qian Niu, D. J. Thouless, and Yong-Shi Wu. Quantized hall conductance as a topological invariant. *Phys. Rev. B*, 31:3372–3377, Mar 1985.

[181] Takahiro Fukui, Yasuhiro Hatsugai, and Hiroshi Suzuki. Chern numbers in discretized brillouin zone: Efficient method of computing (spin) hall conductances. *Journal of the Physical Society of Japan*, 74(6):1674–1677, 2005.

[182] Huaiming Guo and Shun-Qing Shen. Topological phase in a one-dimensional interacting fermion system. *Phys. Rev. B*, 84:195107, Nov 2011.

[183] D. N. Sheng, Z. Y. Weng, L. Sheng, and F. D. M. Haldane. Quantum spin-hall effect and topologically invariant chern numbers. *Phys. Rev. Lett.*, 97:036808, Jul 2006.

[184] Belen Paredes, Artur Widera, Valentin Murg, Olaf Mandel, Simon Folling, Ignacio Cirac, Gora V. Shlyapnikov, Theodor W. Hansch, and Immanuel Bloch. Tonks-girardeau gas of ultracold atoms in an optical lattice. *Nature*, 429(6989):277–281, May 2004.

[185] Andreas M. Lauchli. *Numerical simulations of frustrated systems*, chapter 10. 2011.

[186] Hsiang hsuan Hung. *Exotic quantum magnetism and superfluidity in optical lattices*. PhD thesis, UNIVERSITY OF CALIFORNIA, SAN DIEGO, 2011.